研究成果の刊行に関する一覧表

雑誌

発表者氏名	論文タイトル名	発表誌名	巻号	ページ	出版年
Yamada S., Kubo Y., Yamazaki D., Sekino Y., Nomura Y., Yoshida S., Kanda Y.	Tributyltin Inhibits Neural Induction of Human Induced Pluripotent Stem Cells.	論文投稿中			
Yamada S., Yamazaki D., Kanda Y.	5-Fluorouracil inhibits neural induction via Mfn1/2 reduction in human induced pluripotent stem cells.	論文投稿中			
Yamada S., Kubo Y., Yamazaki D., Sekino Y., Kanda Y.	Chlorpyrifos inhibits neural induction via Mfn1-mediated mitochondrial dysfunction in human induced pluripotent stem cells.	Sci Rep.	7	40925	2017
Yamazaki D., Kanda Y., Sekino Y.	Field potential recording method using multi-electrode array system-Cellular responses in human iPSC-derived cardiomyocytes and rodent brain-derived neurons-.	BUNSEKI	7	290-295	2017
Mabuchi H., Ong HY., Watanabe K., Yoshida S., Hozumi N.	Visualization of Spatially Distributed Bioactive Molecules Using Enzyme-Linked Photo Assay.	IEEJ Trans FM.	136	99-104	2016
Takanashi K., Washiya M., Ota K., Yoshida S., Hozumi N., Kobayashi K.	Quantitative evaluation method for differentiation of C2C12 myoblasts by ultrasonic microscopy.	Jpn J Appl Phys.	56	07JF11	2017
Tiong TKS., Chean TW., Yamada H., Takahashi K., Hozumi N., Kobayashi K., Yoshida S.	Effects of anticancer drugs on glia–glioma brain tumor model characterized by acoustic impedance microscopy.	Jpn J Appl Phys.	56	07JF15	2017
Fueta Y., Sekino Y., Yoshida S., Kanda Y., Ueno S.	Prenatal exposure to valproic acid alters the development of excitability in the postnatal rat hippocampus.	Neurotoxicology	65	1-8	2018
Zhang W., Qian L., Lambertini L., Finik J., Huang Y., Tsuchiya KJ., Pehme P., Buthmann J., Yoshida S., Chen J., Nomura Y.	Timing of Prenatal Exposure to Trauma and Altered Placental Expressions of HPA-Axis Genes and Genes Driving Neurodevelopment.	J Neuroendocrinol.		in press	2018
Fueta Y., Ishidao T., Ueno S., Yoshida Y., Kanda Y., Hori H.	Prenatal exposure to 1-bromopropane causes delayed adverse effects on hippocampal neuronal excitability in the CA1 subfield of rat offspring.	J Occup Health.	60	74-79	2018

Urushiyama D., Suda W., Ohnishi E., Araki R., Kiyoshima C., Kurakazu M., Sanui A., Yotsumoto F., Murata M., Nabeshima K., Yasunaga S., Saito S., Nomiyama M., Hattori M., Miyamoto S., Hata K.	Microbiome profile of the amniotic fluid as a predictive biomarker of perinatal outcome.	Sci Rep.	7	12171	2017
Kawai T., Hata K.	Reproductive/Developmental Abnormalities Induced by Epigenetic Aberrations and Possible Environmental Causes.	Nihon Eiseigaku Zasshi.	71	195-199	2016
Ito Y., Maehara K., Kaneki E., Matsuoka K., Sugahara N., Miyata T., Kamura H., Yamaguchi Y., Kono A., Nakabayashi K., Migita O., Higashimoto K., Soejima H., Okamoto A., Nakamura H., Kimura T., Wake N., Taniguchi T., Hata K.	Novel Nonsense Mutation in the NLRP7 Gene Associated with Recurrent Hydatidiform Mole.	Gynecol Obstet Invest.	81	353-358	2016
Nohara K., Okamura K., Suzuki T., Murai H., Ito T., Shinjo K., Takumi S., Michikawa T., Kondo Y., Hata K.	Augmenting effects of gestational arsenite exposure of C3H mice on the hepatic tumors of the F2 male offspring via the F1 male offspring.	J Appl Toxicol.	36	105-112	2016
Kawai T., Yamada T., Abe K., Okamura K., Kamura H., Akaishi R., Minakami H., Nakabayashi K., Hata K.	Increased epigenetic alterations at the promoters of transcriptional regulators following inadequate maternal gestational weight gain.	Sci Rep.	5	14224	2015

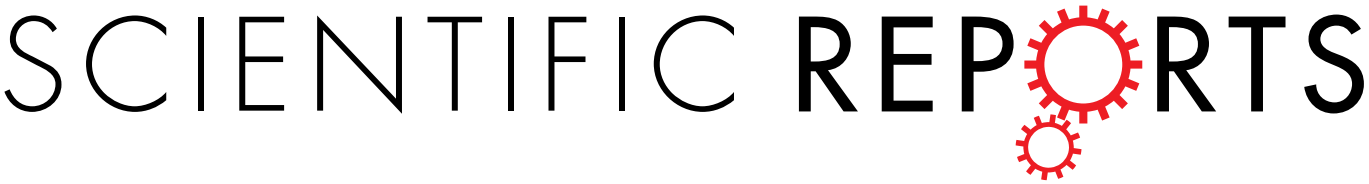

OPEN

Received: 21 October 2016
Accepted: 13 December 2016
Published: 23 January 2017

Chlorpyrifos inhibits neural induction via Mfn1-mediated mitochondrial dysfunction in human induced pluripotent stem cells

Shigeru Yamada[1,2], Yusuke Kubo[1], Daiju Yamazaki[1], Yuko Sekino[1] & Yasunari Kanda[1]

Organophosphates, such as chlorpyrifos (CPF), are widely used as insecticides in agriculture. CPF is known to induce cytotoxicity, including neurodevelopmental toxicity. However, the molecular mechanisms of CPF toxicity at early fetal stage have not been fully elucidated. In this study, we examined the mechanisms of CPF-induced cytotoxicity using human induced pluripotent stem cells (iPSCs). We found that exposure to CPF at micromolar levels decreased intracellular ATP levels. As CPF suppressed energy production that is a critical function of the mitochondria, we focused on the effects of CPF on mitochondrial dynamics. CPF induced mitochondrial fragmentation via reduction of mitochondrial fusion protein mitofusin 1 (Mfn1) in iPSCs. In addition, CPF reduced the expression of several neural differentiation marker genes in iPSCs. Moreover, knockdown of *Mfn1* gene in iPSCs downregulated the expression of *PAX6*, a key transcription factor that regulates neurogenesis, suggesting that Mfn1 mediates neural induction in iPSCs. Taken together, these results suggest that CPF induces neurotoxicity via Mfn1-mediated mitochondrial fragmentation in iPSCs. Thus, mitochondrial dysfunction in iPSCs could be used as a possible marker for cytotoxic effects by chemicals.

Growing evidence suggests the involvement of environmental chemicals in neurodevelopmental toxicity, leading to neurobehavioral outcomes such as learning disabilities, attention deficit hyperactivity disorder, cognitive impairment, and autism[1,2]. As the fetal brain is inherently more susceptible to chemical-induced toxicity compared to the adult brain, exposure to neurotoxic chemicals during early prenatal period can cause delayed neural disorders at lower doses than in adults[3,4].

Organophosphates, such as chlorpyrifos (CPF), are well known to affect brain structure and neurodevelopmental outcome, resulting in delayed neural disorders[5,6]. In regard to this, previous studies using magnetic resonance imaging have shown that prenatal exposure to CPF caused abnormalities in the structure, size, and thickness of cerebral cortex, where was responsible for several higher-order brain functions such as attention, cognition, and emotion[7]. Several reports indicate that CPF causes neurotoxicity in the developing brain of animals. In the developing brain of neonatal rats, CPF exposure impairs neurite outgrowth by inhibiting choline acetyltransferase activity[8]. Maternal exposure to CPF suppresses neurogenesis in the hippocampal dentate gyrus of rat offspring[9]. In addition to *in vivo* effects, there has been reported the cytotoxic effects of micromolar CPF levels *in vitro*. For example, CPF inhibited mitochondrial oxidative phosphorylation[10] and induced apoptosis in human neuroblastoma SH-SY5Y cells[11] or human neural precursor cells[12]. As micromolar CPF levels were detected in the blood of human newborns living in an agricultural community[13], the observations made using micromolar levels of CPF *in vitro* could potentially reflect the biological reactions in a living body. However, the effect of CPF on neurodevelopment has not been precisely elucidated.

[1]Division of Pharmacology, National Institute of Health Sciences, Tokyo, Japan. [2]Pharmacological Evaluation Institute of Japan (PEIJ), Kanagawa, Japan. Correspondence and requests for materials should be addressed to Y.K. (email: kanda@nihs.go.jp)

Morphological changes of mitochondria are known to contribute to homeostasis[14,15]. Under normal circumstances, mitochondria fuses together and forms excessive tubular networks (mitochondrial fusion). These fusion is regulated by fusion factors mitofusin 1 and 2 (Mfn1, Mfn2) and optic atrophy 1 (Opa1)[16,17]. In contrast, under stress conditions, mitochondrial networks convert into large numbers of small fragments with spherical and punctate morphology (mitochondrial fission), and are regulated by fission factors, such as fission protein 1 (Fis1) and dynamin-related protein 1 (Drp1)[18,19]. This morphological dynamics contributes to the maintenance of mitochondrial functions, including energy generation[14]. Moreover, several studies have shown the relationship between mitochondrial fragmentation and cellular and neurodevelopmental defects. For example, Mfn1 or Mfn2 knockout mice die in midgestation embryo, accompanying with developmental delay. In addition, embryonic fibroblasts from these knockout mice display distinct types of fragmented mitochondria, a phenotype due to a severe reduction in mitochondrial fusion[20]. Thus, Mfn1 is considered to be functionally different from Mfn2. In support to this, Mfn1, not Mfn2, is reported to contribute to Opa1-mediated fusion of mitochondrial inner membrane[16].

In the present study, we investigated the effect of CPF on neural differentiation using human induced pluripotent stem cells (iPSCs) as a model of human organ development. We focused on the effects of micromolar levels of CPF on mitochondrial dynamics, examining the molecular mechanisms of the process. Our results show that micromolar CPF levels inhibited ATP production through Mfn1 reduction, followed by mitochondrial fragmentation. Moreover, Mfn1-mediated mitochondrial dysfunction suppressed early neural induction by decreasing levels of *PAX6*, a key transcription factor that regulates neurogenesis. These data suggest that CPF-induced neurodevelopmental toxicity is based on impairment of mitochondrial functions in human iPSCs.

Results

Effect of CPF on neural differentiation of iPSCs. To investigate whether CPF affects early neurodevelopment, we examined neural differentiation capability of iPSCs, which was induced by dual SMAD inhibition protocol[21] (Fig. 1A). First, we determined the critical CPF concentration, affecting neural differentiation. At day 4 after neural induction with different concentrations of CPF, the expression of *PAX6*, an early neuroectodermal marker that regulates neurogenesis[22], was analyzed using real-time PCR. We found that exposure to 30 μM CPF significantly decreased *PAX6* gene expression (Fig. 1B). Next, we performed time course experiments for expression of several neural differentiation markers at days 2, 4, 6, and 8 after exposure to 30 μM CPF. At day 9, almost all cells exposed by CPF (30 μM) were detached from the culture dish. Real-time PCR analysis revealed upregulated expression of *PAX6* by day 4, and *FOXG1*, a neuroectodermal marker that also regulates neurogenesis[23], thereafter (Fig. 1C and D). Representative neural maturation marker *NCAM1*[24] continuously increased, confirming that further neural differentiation occurred (Fig. 1E). In addition, CPF exposure reduced the expression of these neural induction markers by day 6 (Fig. 1C–E). These data suggest that CPF has an inhibitory effect on early neural differentiation of iPSCs.

Mitochondrial function of iPSCs exposed to CPF. As neural differentiation process requires ATP as a source of energy[25], we examined intracellular ATP content in iPSCs. Treatment with 30 μM CPF significantly reduced the ATP content of the cells (Fig. 2A). We have previously shown that 0.1 μM carbonyl cyanide m-chlorophenyl hydrazone (CCCP), which functions as a mitochondrial uncoupler[26], decreased ATP levels in iPSCs. Because CPF inhibited ATP production, we focused on several mitochondrial functions. Mitochondrial membrane potential (MMP) was decreased by exposure to 30 μM CPF for 24 h (Fig. 2B and C). As a positive control, exposure to 0.1 μM CCCP reduced MMP (Figure S1). In addition, CPF exposure increased the number of cells with fragmented mitochondria displaying punctate morphology (Fig. 2D) and decreased the number of cells exhibiting mitochondrial fusion (Fig. 2E). We have already confirmed that 0.1 μM CCCP also increased the occurrence of fragmented mitochondria. These results suggest that CPF induces mitochondrial dysfunction, including MMP depolarization and mitochondrial fragmentation, in iPSCs.

Expression of mitochondrial fission and fusion factors in iPSCs exposed to CPF. To examine the molecular mechanisms by which CPF induces mitochondrial fragmentation in iPSCs, we assessed the expression levels of mitochondrial fission (*Fis1* and *Drp1*) and fusion genes (*Mfn1*, *Mfn2*, and *OPA1*). Real-time PCR analysis showed that the gene expression of the factors was not altered after CPF exposure (Fig. 3A). Interestingly, western blot analysis revealed that CPF significantly decreased Mfn1 protein levels. In contrast, protein expression levels of other factors, including Mfn2, were not changed (Fig. 3B and C). These data suggest that CPF-induced mitochondrial fragmentation is caused by reduction of Mfn1 protein levels.

Effects of CPF in iPSC-derived neural progenitor cells. To investigate whether the effects of CPF selectively occur in the early stage of neural differentiation in iPSCs, we used iPSC-derived neural progenitor cells (NPCs), which were induced by dual SMAD inhibition protocol[21] (Figure S1A). Treatment with 30 μM CPF had little effect on ATP content (Figure S1B). Similarly, exposure to 30 μM CPF had little effect on mitochondrial morphology (Figure S1C and D), which was confirmed by the fact that CPF did not alter the protein levels of mitochondrial fission and fusion factors containing Mfn1 (Figure S1E). These data suggest that iPSCs, not NPCs, are sensitive to CPF exposure.

Effect of Mfn1 knockdown on neural induction of iPSCs. To further investigate the involvement of Mfn1 in the effects of CPF on neural induction, we performed knockdown (KD) of Mfn1, using lentivirus-delivered shRNAs. Real-time PCR analysis showed that KD was selective for *Mfn1*, not *Mfn2*, and that the efficiency was approximately 70% (Fig. 4A). The KD effects were also confirmed by protein levels (Fig. 4B and C). The Mfn1 KD cells were used to perform neural induction. Real-time PCR analysis revealed that Mfn1 KD

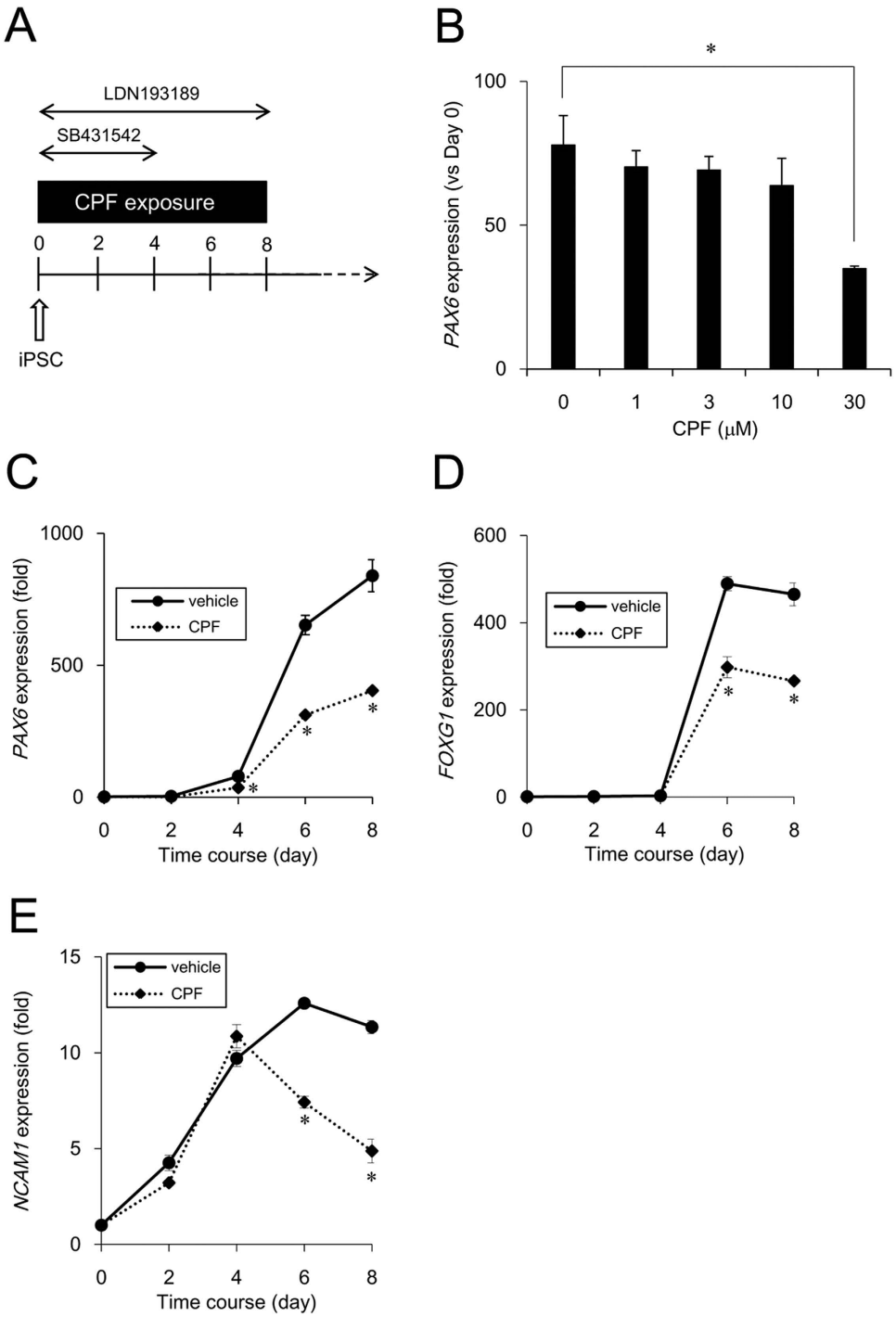

Figure 1. Time course studies of neural induction in iPSCs exposed to CPF. (**A**) Schematic time course of induction from iPSCs to NPCs by dual SMAD inhibition. Neural induction was initiated after exposure to CPF for 24 h. The cells were continuously exposed to CPF throughout neural differentiation. (**B**) At day 4 after neural induction with CPF (0–30 μM), expression of the neural differentiation marker *PAX6* was examined using real-time PCR analysis. (**C–E**) At days 2, 4, 6, and 8 after neural induction with CPF (30 μM), expression of neural differentiation markers, *PAX6*, *FOXG1*, and *NCAM1* was examined using real-time PCR analysis. Data are represented as means ± SD (n = 3). $^{*}P < 0.05$.

decreased the expression of *PAX6* (day 4), *FOXG1* (day 6) and *NCAM1* (day 6) (Fig. 4D). These data suggest that Mfn1 is involved in CPF-mediated negative effects on neural induction of iPSCs.

Negative regulation of neural induction by CPF exposure. A previous report indicates that ERK signaling inhibits neural induction via *PAX6* silencing in human embryonic stem cells[27]. ERK has been reported to be activated after depletion of Mfn1[28]. We focused on ERK signaling in the effect of CPF on neural induction.

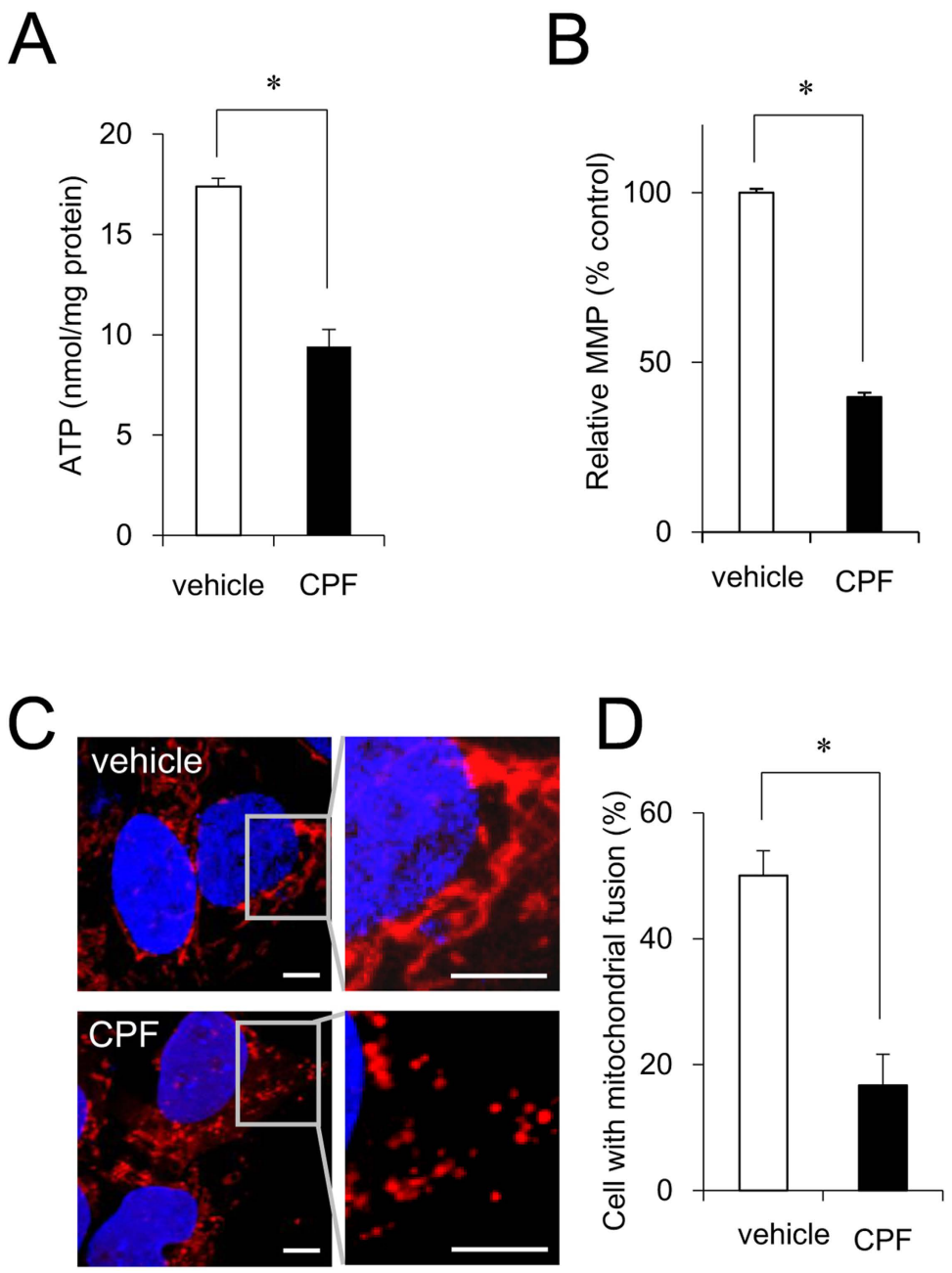

Figure 2. Mitochondrial function of iPSCs exposed to CPF. (**A**) Cells were exposed to CPF (30 μM) for 24 h. Intracellular ATP content was determined in the lysed cells (n = 3). (**B**) Cells were exposed to CPF for 24 h and stained with JC-10 for 20 min. MMP of JC-10 labeled cells was analyzed by flow cytometry. The histogram represents the ratio of JC-aggregate (F-590) to JC-monomer (F-535) fluorescence (n = 3). (**C**) Cells were exposed to CPF for 72 h and stained with MitoTracker Red CMXRos and Hoechst33342. Mitochondrial morphology was observed by confocal laser microscopy. Bar = 5 μm. (**D**) The number of cells with mitochondrial fusion (<10% punctiform) was determined in each image (n = 5). Data are represented as means ± SD. *$P < 0.05$.

We found that CPF exposure significantly increased basal ERK phosphorylation levels, which were abolished by treatment with the ERK inhibitor U0126 (Fig. 5A and B). To further study whether *PAX6* downregulation in CPF-exposed cells occurred through ERK signaling, we examined the effect of U0126 on *PAX6* expression. Incubation with U0126 recovered the expression levels of *PAX6* (Fig. 5C). These data suggest that CPF activates ERK and prevents neural induction via *PAX6* downregulation.

Effect of Mfn1 knockdown on neural induction. To confirm the involvement of Mfn1 in the inhibition of neural induction by CPF, we used Mfn1 KD cells. Mfn1 KD significantly increased basal ERK phosphorylation levels that were abolished by treatment with the ERK inhibitor U0126 (Fig. 6A and B). To further study

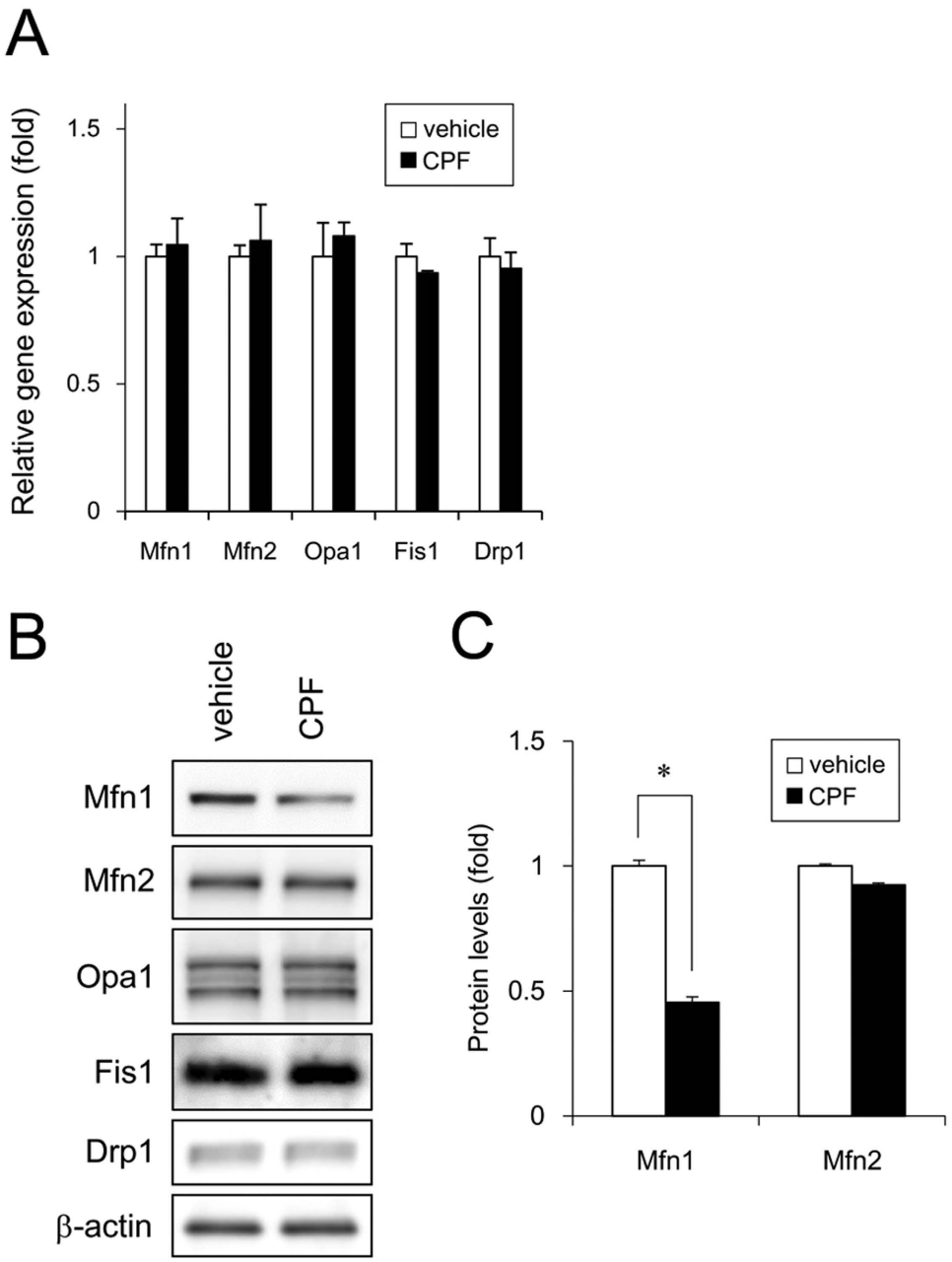

Figure 3. Expression of mitochondrial fission and fusion factors of iPSCs exposed to CPF. (**A**) After exposure to CPF (30 μM) for 24 h, expression of mitochondrial genes was analyzed by real-time PCR. (**B**) After exposure to CPF for 24 h, expression of mitochondrial proteins was analyzed by western blotting using anti-Drp1, anti-Fis1, anti-Mfn1, anti-Mfn2, anti-Opa1, or anti-β-actin antibodies. (**C**) Relative densities of bands were quantified with ImageJ software. Relative changes in expression were determined by normalization to β-actin. Data are represented as means ± SD (n = 3). $^{*}P < 0.05$.

whether *PAX6* downregulation in Mfn1 KD cells occurred through ERK signaling, we examined the effect of U0126 on *PAX6* expression. Mfn1 KD decreased *PAX6* by 64% by in the vehicle-treated cells. In contrast, Mfn1 KD decreased *PAX6* by 30% in the U0126-treated cells. Thus, incubation with U0126 partially recovered the *PAX6* expression in the Mfn1 KD cells (Fig. 6C). Taken together, these data suggest that Mfn1 reduction by CPF exposure activates ERK and prevents neural induction via *PAX6* downregulation.

Discussion

In the present study, we demonstrated that exposure to micromolar CPF targeted mitochondrial quality control in human iPSCs. We showed that CPF induced Mfn1 reduction, thereby promoting mitochondrial fragmentation. These negative effects of CPF on mitochondrial quality control could suppress ATP production and neural

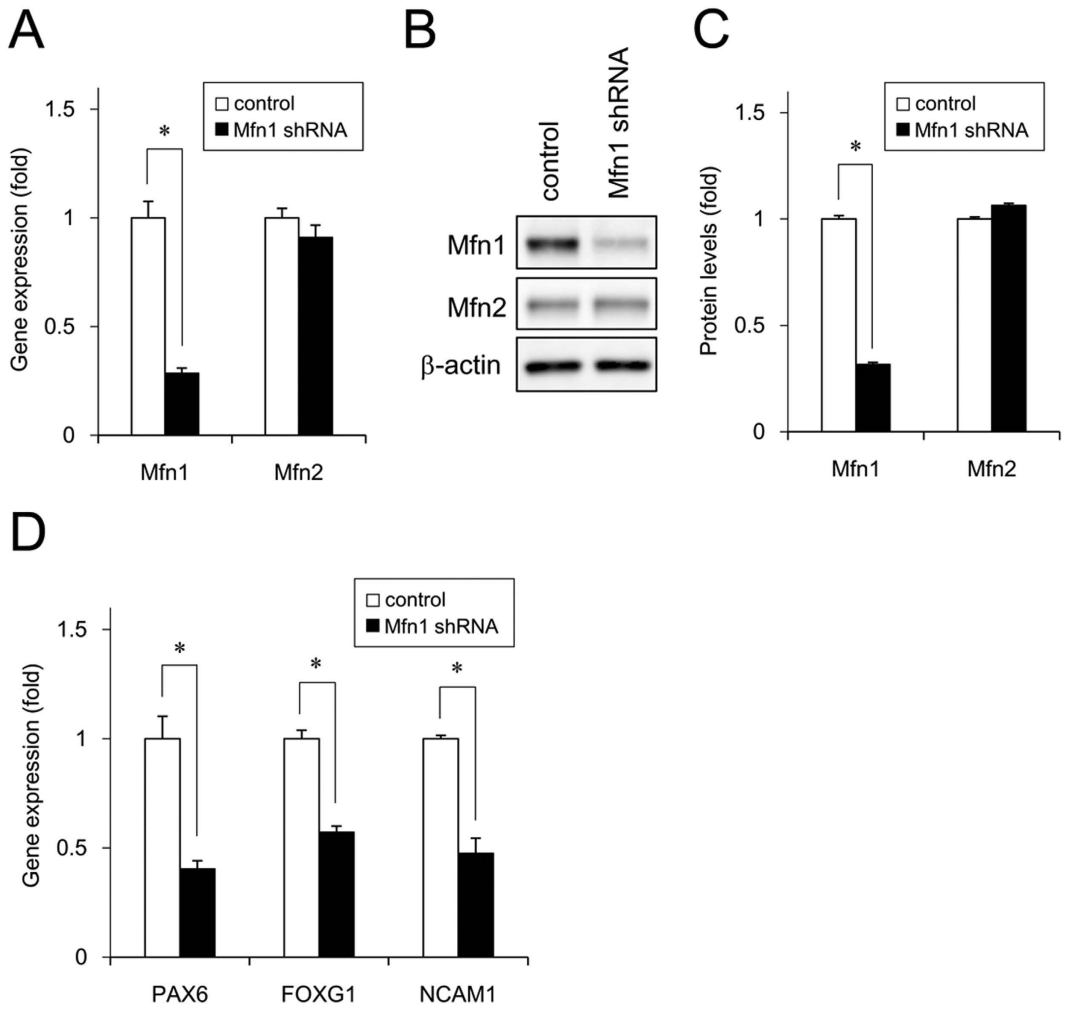

Figure 4. Effect of Mfn1 knockdown on neural induction of iPSCs. Cells were infected with lentiviruses containing a vector encoding a shRNA directed against *Mfn1* or a scrambled sequence shRNA (control) for 24 h. The infected cells were subjected to selection with puromycin (1 μg/ml) for 24 h and cultured for an additional 72 h prior to functional analyses. (**A**) The expression of *Mfn1* and *Mfn2* genes was analyzed by real-time PCR. (**B**) The expression of Mfn1 and Mfn2 proteins was analyzed by western blotting using anti-Mfn1, anti-Mfn2, or anti-β-actin antibodies. (**C**) Relative densities of bands were quantified with ImageJ software. Relative changes in expression were determined by normalization to β-actin. (**D**) Expression of neural differentiation markers *PAX6* (day 4), *FOXG1* (day 6), and *NCAM1* (day 6) was examined with real-time PCR. Data are represented as means ± SD (n = 3). $^*P < 0.05$.

differentiation. Based on the data observed in our study, Fig. 7 shows a proposed mechanism of CPF cytotoxicity via mitochondrial dysfunction.

Our studies showed that treatment with micromolar CPF levels caused mitochondrial dysfunction of human iPSCs (Fig. 2). We observed that iPSCs were sensitive to CPF exposure, unlike iPSC-derived NPCs (Figure S1). Previous reports support this difference in CPF sensitivity. The inhibitory effect of CPF on DNA synthesis in undifferentiated C6 glioma cells is found to be much higher than in differentiated cells[29]. *In vivo* studies indicate that immature organisms are more susceptible to CPF-induced toxicity compared to adults due to lower levels of CPF metabolizing enzymes[30]. Thus, the difference in CPF sensitivity between iPSCs and NPCs may be dependent on the maturation of CPF detoxification pathways. We are currently conducting experiments to determine the mechanism causing the differences in sensitivity to CPF.

We showed that CPF induced mitochondrial fragmentation via Mfn1 reduction (Figs 2 and 3). Consistent with this, our previous knockdown studies indicated that Mfn1 reduction was sufficient to promote mitochondrial dysfunction[31]. CPF-induced Mfn1 reduction might mediate mitochondrial fragmentation, decrease ATP levels, and inhibit iPSC growth. Although Mfn2 is also involved in mitochondrial fission and energy supply processes[32,33], our results indicated that CPF specifically targeted Mfn1, not Mfn2. Regarding this apparent CPF specificity, E3 ubiquitin ligase membrane-associated RING-CH 5 (MARCH5) has been reported to selectively bind to Mfn1 dependent on its acetylation, and degrade among all mitochondrial proteins, including Mfn2[34]. In addition, we have reported that organotin compounds induced Mfn1 degradation through MARCH5,

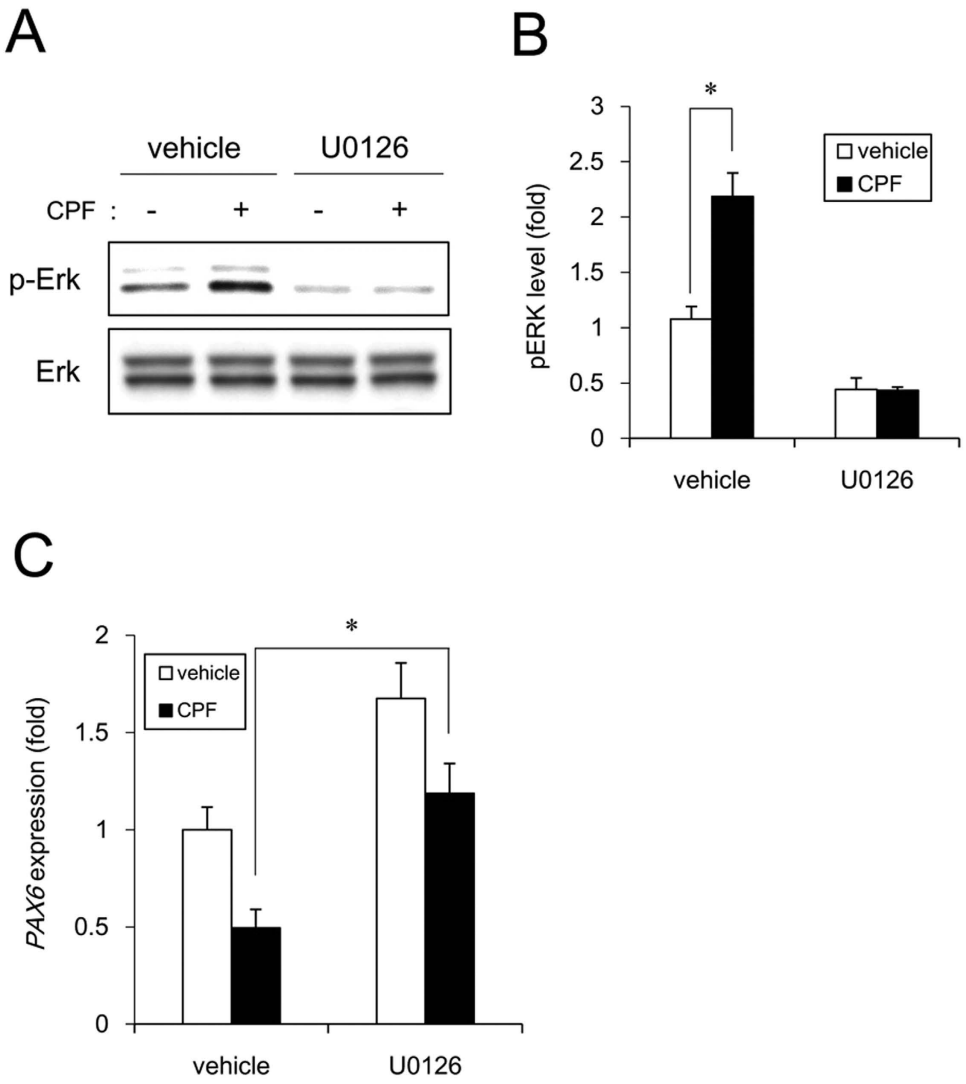

Figure 5. Negative regulation of neural induction by CPF exposure. (**A**) Cells were exposed to CPF (30 μM) or CPF + U0126 (5 μM) for 24 h. ERK phosphorylation was analyzed by western blotting using anti-phospho-ERK antibodies. (**B**) Relative densities of bands were quantified with ImageJ software. Relative changes in expression were determined by normalization to total ERK protein level. (**C**) At day 4 after neural induction with CPF or CPF + U0126, the expression of *PAX6* gene was analyzed by real-time PCR. Data are represented as means ± SD (n = 3). **P* < 0.05.

thereby promoting mitochondrial fragmentation in iPSCs[31]. Thus, CPF may specifically target Mfn1 protein via MARCH5 in iPSCs without affecting mRNA levels. Furthermore, the difference in CPF sensitivity between iPSCs and NPCs may be dependent on Mfn1 and MARCH5 expression levels or MARCH5 activity. Further studies should determine whether CPF reduces Mfn1 via MARCH5-mediated degradation in iPSCs.

We demonstrated that ERK phosphorylation mediated the negative effects of CPF on early neural differentiation (Figs 1, 4 and 5). A previous report indicates that Mfn1 directly binds Ras and Raf, resulting in the inhibition of Ras-Raf-ERK signaling by the biochemical analysis[35,36]. Mfn1 reduction by CPF or shRNA may reverse this ERK signaling inhibition. Mobilization of Ca^{2+} from intracellular stores, including mitochondria was reported to result in phosphorylation of MAPKs, as the process was suppressed by chelation of intracellular Ca^{2+} in human T lymphoblastoid cells[37]. As mitochondria are known to uptake into the matrix of any Ca^{2+} that has accumulated in the cytosol, dependent on MMP[38], mitochondrial dysfunction by CPF exposure may cause an overload of Ca^{2+}, resulting in ERK activation. Moreover, ERK signaling was reported to inhibit neural induction by *PAX6* silencing via upregulation of stemness factors *NANOG/OCT4* and downregulation of homeobox transcription factor *OTX2*[27]. NANOG and OCT4 act as repressors of *PAX6* induction, whereas OTX2 is a positive inducer of *PAX6*[27]. Therefore, ERK signaling evoked by CPF could affect the expression of these transcriptional network, including *NANOG*, *OCT4* and *OTX2*, *by* regulating *PAX6*. In future studies, we should further investigate the mechanisms of CPF-induced negative regulation of neural induction via ERK.

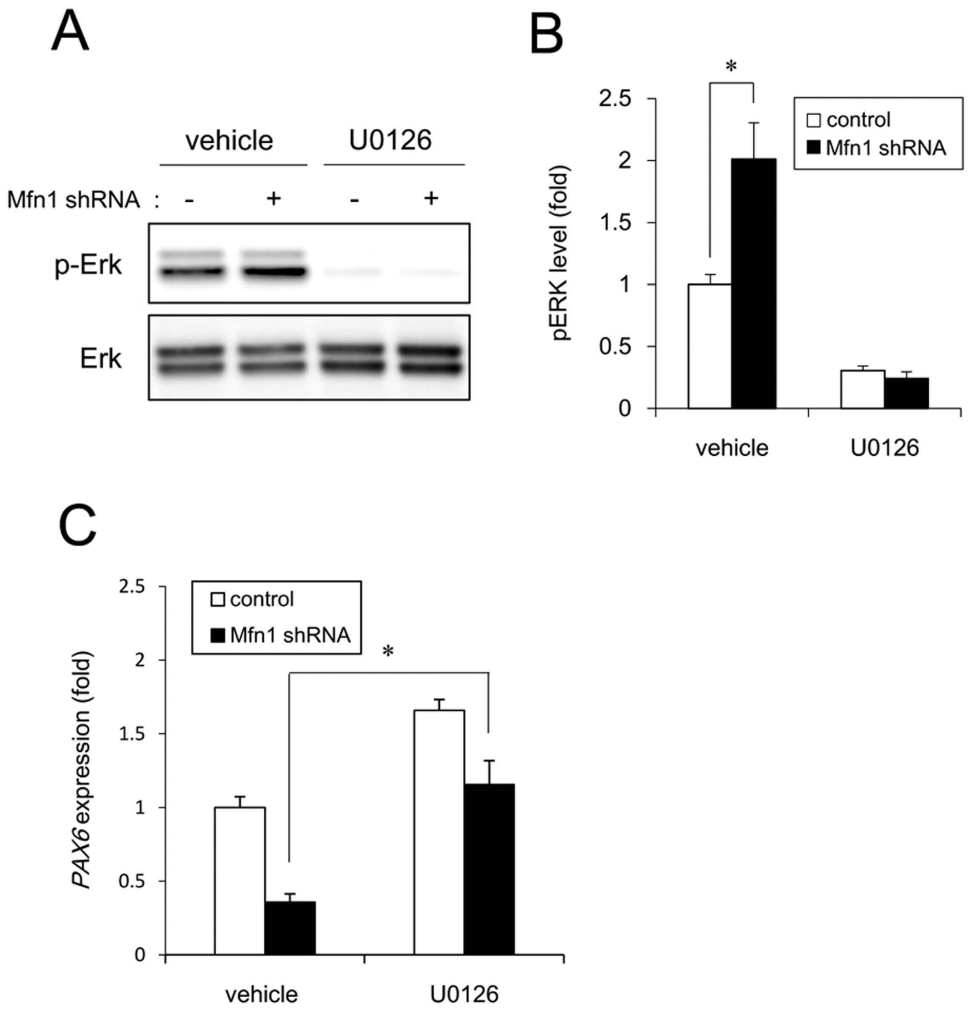

Figure 6. Negative regulation of neural induction by Mfn1 knockdown. The cells were infected with lentiviruses containing a vector encoding a shRNA directed against Mfn1 or a scrambled sequence shRNA (control) for 24 h. The infected cells were subjected to selection with 1 μg/ml puromycin for 24 h and cultured for an additional 72 h prior to functional analyses. (**A**) After incubation with U0126 for 24 h, ERK phosphorylation was analyzed by western blotting using anti-phospho-ERK antibodies. (**B**) Relative densities of bands were quantified with ImageJ software. Relative changes in expression were determined by normalization to total ERK protein level. (**C**) At day 4 after neural induction with U0126, the expression of *PAX6* gene was analyzed by real-time PCR. Data are represented as means ± SD (n = 3). $^{*}P < 0.05$.

We further demonstrated that Mfn1 reduction mediated cytotoxic effects of CPF on iPSCs via *PAX6* downregulation (Figs 5 and 6). *FOXG1* was downregulated, along with *PAX6*, during neural differentiation of iPSCs exposed to CPF. *PAX6* and *FOXG1* act as transcriptional regulators during forebrain development in vertebrates[39,40]. Targeted disruption of *PAX6* and *FOXG1* in rodents led to the loss of anterior neural tissues, suggesting the central role of these genes in forebrain development[41,42]. CPF causes various defects in the development of hippocampus and cortex of rodents[43]. Thus, CPF-induced defects of forebrain architecture may be caused by transcriptional silencing of anterior neural markers during early neurogenesis. As *NCAM1* was downregulated during neural differentiation of iPSCs exposed to CPF, further studies using NPCs are required to reveal how CPF affects neural maturation processes.

In summary, our results demonstrate a novel mechanism underlying cytotoxicity, including neurodevelopmental toxicity of CPF in iPSCs. Recently, significant progress has been made in the induction of differentiation of pluripotent stem cells into a variety of cell types[44]. Further studies are needed to evaluate the developmental effects of CPF on various types of iPSC-derived cells. Moreover, we show that CPF toxicity is caused by Mfn1-mediated mitochondrial dysfunction, which is involved in the cytotoxicity of organotin compounds[31]. Thus, mitochondrial functions influenced by Mfn1 might be a good starting point for investigating toxic mechanisms induced by exposure to other chemicals.

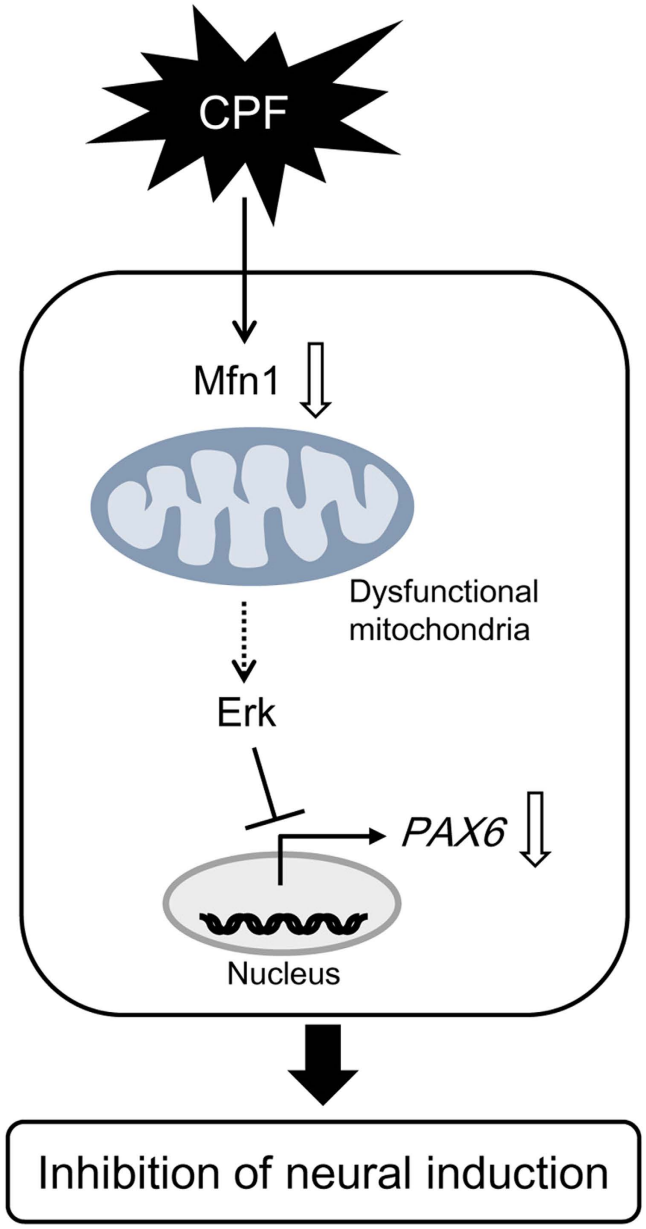

Figure 7. Proposed mechanism of CPF cytotoxicity in human iPSCs. CPF exposure causes Mfn1 reduction, which induces mitochondrial dysfunction, including mitochondrial fragmentation and decreased ATP levels. Mitochondrial dysfunction in turn evokes ERK phosphorylation, leading to the suppression of *PAX6*, which is an early marker of neurogenesis.

Methods

Chemicals. Chlorpyrifos (CPF), Y-27632, SB431542, and LDN193189 were obtained from Wako (Tokyo, Japan). Penicillin-streptomycin mixture (PS) was obtained from Thermo Fisher Scientific (Waltham, MA, USA). U0126 was obtained from Enzo Life Sciences (Farmingdale, NY, USA). Poly-L-ornithine, 2-mercaptoethanol (2-ME), and carbonylcyanide *m*-chlorophenylhydrazone (CCCP) were obtained from Sigma-Aldrich (St. Louis, MO, USA). All other reagents were of analytical grade and obtained from commercial sources.

Cell culture. Human iPSC line 253G1 (Riken BRC Cell Bank, Tsukuba, Ibaraki, Japan) was established through retroviral transduction of *OCT4*, *SOX2*, and *KLF4* into adult human dermal fibroblasts[45]. The cells were cultured under feeder-free conditions using human embryonic stem cell (ESC)-qualified Matrigel (BD Biosciences, San Jose, CA, USA) and TeSR-E8 medium (Stemcell Technologies, Vancouver, BC, Canada) at 37 °C in an atmosphere containing 5% CO_2. For passage, iPSC colonies were dissociated into single cells using Accumax (Innovative Cell Technologies, San Diego, CA, USA) and cultured in TeSR-E8 medium supplemented with Y-27632 (ROCK inhibitor, 10 μM). The NPCs derived from iPSCs were cultured on poly-L-ornithine and Laminin (Thermo Fisher Scientific) coated dishes at 37 °C in an atmosphere containing 5% CO_2. The culture

medium was Neural maintenance medium [NMM; a 1 : 1 mixture of DMEM/F12 (Thermo Fisher Scientific) and Neurobasal (Thermo Fisher Scientific) containing N2 (Thermo Fisher Scientific), B27 (Thermo Fisher Scientific), GlutaMAX (Thermo Fisher Scientific), non-essential amino acids (NEAA; Thermo Fisher Scientific), 2-ME, PS]. For passage, NPCs were dissociated into single cells using Accumax and cultured in NMM supplemented with EGF (20 ng/ml), FGF2 (20 ng/ml) and Y-27632.

Neural differentiation procedure. For the induction of neuronal lineages, dual SMAD inhibition protocol was used as previously described[21] with modifications. Briefly, iPSC colonies were dissociated into single cells with Accumax. The cells were seeded at a density of 7×10^4 cells/cm^2 in TeSR-E8 medium on Matrigel-coated plates in order to reach nearly confluent within two days after seeding. The initial differentiation medium was knockout serum replacement (KSR) medium [Knockout DMEM (Thermo Fisher Scientific) containing KSR (Thermo Fisher Scientific), L-glutamine, NEAA, 2-ME, PS] with SB431542 (TGFβ inhibitor, 10 μM) and LDN193189 (BMP inhibitor, 1 μg/ml). After 4 days, N2 medium [Neurobasal containing N2, B27, GlutaMAX, PS] was added to the KSR medium with LDN193189 every two days.

Measurement of intracellular ATP levels. Intracellular ATP content was measured using an ATP Determination Kit (Thermo Fisher Scientific), according to the manufacturer's protocol. Briefly, the cells were washed and lysed with 0.1% Triton X-100/PBS. The resulting cell lysates were added to a reaction mixture containing 0.5 mM D-luciferin, 1 mM DTT, and 1.25 μg/mL luciferase and incubated for 30 min at room temperature. Luminescence was measured using a Fluoroskan Ascent FL microplate reader (Thermo Fisher Scientific). The luminescence intensities were normalized to the total protein content.

Measurement of MMP. A Cell Meter JC-10 Mitochondrial Membrane Potential Assay Kit (AAT Bioquest, Sunnyvale, CA, USA) was used to detect MMP. Briefly, the cells were suspended in staining buffer containing JC-10 and incubated for 20 min at room temperature. After the cells were treated with CPF, a FACS Aria II cell sorter (BD Biosciences) was used to measure the fluorescence intensity ratio, JC-aggregate (F-590)/JC-monomer (F-535).

Assessment of mitochondrial fusion. After treatment with CPF (30 μM, 72 h), the cells were fixed with 4% paraformaldehyde and stained with 50 nM MitoTracker Red CMXRos (Cell Signaling Technology, Danvers, MA, USA) and 5 μg/mL Hoechst 33342 (Sigma-Aldrich). Changes in mitochondrial morphology were observed using a confocal laser microscope (Nikon A1). Images ($n = 5$) of random fields were taken, and the number of cells displaying mitochondrial fusion (<10% punctiform) was determined in each image, as previously reported[46].

Real-time polymerase chain reaction (PCR). Total RNA was isolated from iPSCs using TRIzol reagent (Thermo Fisher Scientific), and quantitative real-time reverse transcription (RT)-PCR was performed using a QuantiTect SYBR Green RT-PCR Kit (Qiagen, Valencia, CA, USA) on an ABI PRISM 7900HT sequence detection system (Applied Biosystems, Foster City, CA, USA) as previously reported[47]. Relative changes in transcript levels were normalized to the mRNA levels of glyceraldehyde-3-phosphate dehydrogenase (*GAPDH*). The following primer sequences were used for real-time PCR analysis: *Fis1*, forward, 5′-TACGTCCGCGGGTTGCT-3′ and reverse, 5′-CCAGTTCCTTGGCCTGGTT-3′; *Drp1*, forward, 5′-TGGGCGCCGACATCA-3′ and reverse, 5′-GCTCTGCGTTCCCACTACGA-3′; *Mfn1*, forward, 5′-GGCATCTGTGGCCGAGTT-3′ and reverse, 5′-ATTATGCTAAGTCTCCGCTCCAA-3′; *Mfn2*, forward, 5′-GCTCGGAGGCACATGAAAGT-3′ and reverse, 5′-ATCACGGTGCTCTTCCCATT-3′; *Opa1*, forward, 5′-GTGCTGCCCGCCTAGAAA-3′ and reverse, 5′-TGACAGGCACCCGTACTCAGT-3′; *PAX6*, forward, 5′-ATGTGTGAGTAAAATTCTGGGCA-3′ and reverse, 5′-GCTTACAACTTCTGGAGTCGCTA-3′; *FOXG1*, forward, 5′-GCCACAATCTGTCCCTCAACA-3′ and reverse, 5′-GACGGGTCCAGCATCCAGTA-3′; *NCAM1*, forward, 5′-GGCATTTACAAGTGTGTGGTTAC-3′ and reverse, 5′-TTGGCGCATTCTTGAACATGA-3′; *GAPDH*, forward, 5′-GTCTCCTCTGACTTCAACAGCG-3′ and reverse, 5′-ACCACCCTGTTGCTGTAGCCAA-3′.

Western blot analysis. Western blot analysis was performed as previously reported[48]. Briefly, the cells were lysed with Cell Lysis Buffer (Cell Signaling Technology). The proteins were then separated by sodium dodecyl sulfate-polyacrylamide gel electrophoresis (SDS-PAGE) and electrophoretically transferred to Immobilon-P membranes (Millipore, Billerica, MA, USA). The membranes were probed with anti-Drp1 monoclonal antibodies (1:1000; Cell Signaling Technology), anti-Fis1 polyclonal antibodies (1:200; Santa Cruz Biotechnology, Santa Cruz, CA, USA), anti-Mfn1 polyclonal antibodies (1:1000; Cell Signaling Technology), anti-Mfn2 monoclonal antibodies (1:1000; Cell Signaling Technology), anti-Opa1 monoclonal antibodies (1:1000; BD Biosciences), anti-ERK1/2 polyclonal antibodies (1:1000; Cell Signaling Technology), anti-phospho ERK1/2 (Thr202/Tyr204) monoclonal antibodies (1:2000; BD Biosciences), and anti-β-actin monoclonal antibodies (1:5000; Sigma-Aldrich). The membranes were then incubated with secondary antibodies against rabbit or mouse IgG conjugated to horseradish peroxidase (Cell Signaling Technology). The bands were visualized using an ECL Western Blotting Analysis System (GE Healthcare, Buckinghamshire, UK). Images were acquired using an LAS-3000 Imager (FUJIFILM, Tokyo, Japan).

Gene knockdown by shRNA. Knockdown experiments were performed using *Mfn1* shRNA lentiviruses from Sigma-Aldrich (MISSION shRNA), as previously reported[49]. A scrambled hairpin sequence was used as a negative control. Briefly, the cells were infected with the viruses at a multiplicity of infection of 1 in the presence

of 8 μg/mL hexadimethrine bromide (Sigma-Aldrich) for 24 h. After medium exchange, the cells were subjected to selection with 1 μg/mL puromycin for 24 h and cultured for an additional 72 h prior to functional analyses.

Statistical analysis. All data are presented as means ± standard deviation (SD). Analysis of variance (ANOVA) followed by post-hoc Bonferroni test was used to analyze data in Figs 1, 3C, 4, 5, and 6. Student's t test was used to analyze data in Figs 2, 3A, S1, and S2. *P*-values < 0.05 were considered statistically significant.

References

1. Landrigan, P. J., Lambertini, L. & Birnbaum, L. S. A research strategy to discover the environmental causes of autism and neurodevelopmental disabilities. *Environ. Health Perspect.* **120,** a258–a260 (2012).
2. Ross, E. J., Graham, D. L., Money, K. M. & Stanwood, G. D. Developmental consequences of fetal exposure to drugs: what we know and what we still must learn. *Neuropsychopharmacology* **40,** 61–87 (2015).
3. Rodier, P. M. Developing brain as a target of toxicity. *Environ. Health Perspect.* **103,** 73–76 (1995).
4. Rice, D. & Barone, S. Jr. Critical periods of vulnerability for the developing nervous system: evidence from humans and animal models. *Environ. Health* Perspect.**108,** 511–533 (2000).
5. Brown, M. A. & Brix, K. A. Review of health consequences from high-, intermediate- and low-level exposure to organophosphorus nerve agents. *J. Appl. Toxicol.* **18,** 393–408 (1998).
6. Ray, D. E. & Richards, P. G. The potential for toxic effects of chronic, low-dose exposure to organophosphates. *Toxicol. Lett.* **120,** 343–351 (2001).
7. Rauh, V. A. *et al.* Brain anomalies in children exposed prenatally to a common organophosphate pesticide. *Proc. Natl. Acad. Sci. USA* **109,** 7871–7876 (2012).
8. Slotkin, T. A., Levin, E. D. & Seidler, F. J. Comparative developmental neurotoxicity of organophosphate insecticides: effects on brain development are separable from systemic toxicity. *Environ. Health Perspect.* **114,** 746–751 (2006).
9. Ohishi, T. *et al.* Reversible effect of maternal exposure to chlorpyrifos on the intermediate granule cell progenitors in the hippocampal dentate gyrus of rat offspring. *Reprod. Toxicol.* **35,** 125–136 (2013).
10. Salama, M., El-Morsy, D., El-Gamal, M., Shabka, O. & Mohamed, W. M. Mitochondrial complex I inhibition as a possible mechanism of chlorpyrifos induced neurotoxicity. *Ann. Neurosci.* **21,** 85–89 (2014).
11. Lee, J. E., Park, J. H., Jang, S. J. & Koh, H. C. Rosiglitazone inhibits chlorpyrifos-induced apoptosis via modulation of the oxidative stress and inflammatory response in SH-SY5Y cells. *Toxicol. Appl. Pharmacol.* **278,** 159–171 (2014).
12. Lee, J. E., Lim, M. S., Park, J. H., Park, C. H. & Koh, H. C. Nuclear NF-κB contributes to chlorpyrifos-induced apoptosis through p53 signaling in human neural precursor cells. *Neurotoxicology* **42,** 58–70 (2014).
13. Huen, K. *et al.* Organophosphate pesticide levels in blood and urine of women and newborns living in an agricultural community. *Environ. Res.* **117,** 8–16 (2012).
14. Youle, R. J. & van der Bliek, A. M. Mitochondrial fission, fusion, and stress. *Science* **337,** 1062–1065 (2012).
15. van der Bliek, A. M., Shen, Q. & Kawajiri, S. Mechanisms of mitochondrial fission and fusion. *Cold Spring Harb. Perspect. Biol.* **5,** pii: a011072 (2013).
16. Cipolat, S., De Brito, O. M., B. Dal Zilio, B. & Scorrano, L. OPA1 requires mitofusin 1 to promote mitochondrial fusion. *Proc. Natl. Acad. Sci. USA* **101,** 15927–15932 (2004).
17. Koshiba, T. *et al.* Structural basis of mitochondrial tethering by mitofusin complexes. *Science* **305,** 858–862 (2004).
18. Smirnova, E., Griparic, L., Shurland, D.-L. & van der Bliek, A. M. Dynamin-related protein Drp1 is required for mitochondrial division in mammalian cells. *Mol. Biol. Cell* **12,** 2245–2256 (2001).
19. Yoon, Y., Krueger, E. W., Oswald, B. J. & McNiven, M. A. The mitochondrial protein hFis1 regulates mitochondrial fission in mammalian cells through an interaction with the dynamin-like protein DLP1. *Mol. Biol. Cell* **23,** 5409–5420 (2003).
20. Chen, H. *et al.* Mitofusins Mfn1 and Mfn2 coordinately regulate mitochondrial fusion and are essential for embryonic development. *J. Cell Biol.* **160,** 189–200 (2003).
21. Chambers, S. M. *et al.* Highly efficient neural conversion of human ES and iPS cells by dual inhibition of SMAD signaling. *Nat. Biotechnol.* **27,** 275–280 (2009).
22. Manuel, M. N., Mi, D., Mason, J. O. & Price, D. J. Regulation of cerebral cortical neurogenesis by the Pax6 transcription factor. *Front. Cell Neurosci.* **9,** 70 (2015).
23. Shen, L., Nam, H. S., Song, P., Moore, H. & Anderson, S. A. FoxG1 haploinsufficiency results in impaired neurogenesis in the postnatal hippocampus and contextual memory deficits. *Hippocampus* **16,** 875–890 (2006).
24. Polo-Parada, L., Bose, C. M., Plattner, F. & Landmesser, L. T. Distinct roles of different neural cell adhesion molecule (NCAM) isoforms in synaptic maturation revealed by analysis of NCAM 180 kDa isoform-deficient mice. *J. Neurosci.* **24,** 1852–1864 (2004).
25. Cheng, A., Hou, Y. & Mattson, M. P. Mitochondria and neuroplasticity. *ASN. Neuro.* **2,** e00045 (2010).
26. Tanaka, A. *et al.* Proteasome and p97 mediate mitophagy and degradation of mitofusins induced by Parkin. *J. Cell Biol.* **191,** 1367–1380 (2010).
27. Greber, B. *et al.* FGF signalling inhibits neural induction in human embryonic stem cells. *EMBO J.* **30,** 4874–4884 (2011).
28. Son, M. J. *et al.* Mitofusins deficiency elicits mitochondrial metabolic reprogramming to pluripotency. *Cell Death Differ.* **22,** 1957–1969 (2015).
29. Garcia, S. J., Seidler, F. J., Crumpton, T. L. & Slotkin, T. A. Does the developmental neurotoxicity of chlorpyrifos involve glial targets? Macromolecule synthesis, adenylyl cyclase signaling, nuclear transcription factors, and formation of reactive oxygen in C6 glioma cells. *Brain Res.* **891,** 54–68 (2001).
30. Basha, M. & Poojary, A. Cold stress offered modulation on chlorpyrifos toxicity in aging rat central nervous system. *Toxicol. Int.* **19,** 173–181 (2012).
31. Yamada, S. *et al.* Tributyltin induces mitochondrial fission through Mfn1 degradation in human induced pluripotent stem cells. *Toxicol. In Vitro.* **34,** 257–263 (2016).
32. Leboucher, G. P. *et al.* Stress-induced phosphorylation and proteasomal degradation of mitofusin 2 facilitates mitochondrial fragmentation and apoptosis. *Mol. Cell* **47,** 547–557 (2012).
33. Yue, W. *et al.* A small natural molecule promotes mitochondrial fusion through inhibition of the deubiquitinase USP30. *Cell Res.* **24,** 482–496 (2014).
34. Park, Y. Y., Nguyen, O. T., Kang, H. & Cho, H. MARCH5-mediated quality control on acetylated Mfn1 facilitates mitochondrial homeostasis and cell survival. *Cell Death Dis.* **5,** e1172 (2014).
35. Chen, K. H. *et al.* Dysregulation of HSG triggers vascular proliferative disorders. *Nat. Cell Biol.* **6,** 872–883 (2004).
36. Chen, K. H. *et al.* Role of mitofusin 2 (Mfn2) in controlling cellular proliferation. *FASEB J.* **28,** 382–394 (2014).
37. Yu, Z. P., Matsuoka, M., Wispriyono, B., Iryo, Y. & Igisu, H. Activation of mitogen-activated protein kinases by tributyltin in CCRF-CEM cells: role of intracellular Ca(2+). *Toxicol. Appl. Pharmacol.* **168,** 200–207 (2000).
38. Pizzo, P., Drago, I., Filadi, R. & Pozzan, T. Mitochondrial Ca^{2+} homeostasis: mechanism, role, and tissue specificities. *Pflugers Arch.* **464,** 3–17 (2012).

39. Danesin, C. & Houart, C. A. Fox stops the Wnt: implications for forebrain development and diseases. *Curr. Opin. Genet. Dev*. **22,** 323–330 (2012).
40. Georgala, P. A., Carr, C. B. & Price, D. J. The role of Pax6 in forebrain development. *Dev. Neurobiol.* **71,** 690–709 (2011).
41. Tuoc, T. C. *et al.* Selective cortical layering abnormalities and behavioral deficits in cortex-specific Pax6 knock-out mice. *J. Neurosci.* **29,** 8335–8349 (2009).
42. Tian, C. *et al.* Foxg1 has an essential role in postnatal development of the dentate gyrus. *J. Neurosci.* **32,** 2931–2949 (2012).
43. Chen, X. P., Chen, W. Z., Wang, F. S. & Liu, J. X. Selective cognitive impairments are related to selective hippocampus and prefrontal cortex deficits after prenatal chlorpyrifos exposure. *Brain Res.* **1474,** 19–28 (2012).
44. Li, K. *et al.* Differentiation of pluripotent stem cells for regenerative medicine. *Biochem. Biophys. Res. Commun.* **471,** 1–4 (2016).
45. Nakagawa, M. *et al.* Generation of induced pluripotent stem cells without Myc from mouse and human fibroblasts. *Nat. Biotechnol.* **26,** 101–106 (2008).
46. Fan, X., Hussien, R. & Brooks, G. A. H_2O_2-induced mitochondrial fragmentation in C2C12 myocytes. *Free Radic. Biol. Med.* **49,** 1646–1654 (2010).
47. Hirata, N. *et al.* Sphingosine-1-phosphate promotes expansion of cancer stem cells via S1PR3 by a ligand-independent Notch activation. *Nat. Commun.* **5,** 4806 (2014).
48. Kanda, Y. *et al.* Reactive oxygen species mediate adipocyte differentiation in mesenchymal stem cells. *Life Sci.* **89,** 250–258 (2011).
49. Yamada, S. *et al.* NAD-dependent isocitrate dehydrogenase as a novel target of tributyltin in human embryonic carcinoma cells. *Sci. Rep*. **4,** 5952 (2014).

Acknowledgements

This work was supported by a Health and Labour Sciences Research Grant from the Ministry of Health, Labour, and Welfare, Japan (#H25-Kagaku-Ippan-002 and #H28-Kagaku-Ippan-003 to Y.Ka.), a Grant-in-Aid for Scientific Research from the Ministry of Education, Culture, Sports, Science, and Technology, Japan (#26293056 and #26670041 to Y.Ka.), the Japan Agency for Medical Research and Development, AMED (#15mk0104053h0101 and #16mk0104027j0002 to Y.S.), and a grant from the Smoking Research Foundation (Y.Ka.).

Author Contributions

Y.S. and Y.Ka. planned the project. S.Y. performed most of the experiments. S.Y. and Y.Ka. wrote the manuscript. Y.Ku. and D.Y. provided technical advices. All authors reviewed the manuscript.

Additional Information

Supplementary information accompanies this paper at http://www.nature.com/srep

Competing financial interests: The authors declare no competing financial interests.

How to cite this article: Yamada, S. *et al.* Chlorpyrifos inhibits neural induction via Mfn1-mediated mitochondrial dysfunction in human induced pluripotent stem cells. *Sci. Rep.* **7**, 40925; doi: 10.1038/srep40925 (2017).

Publisher's note: Springer Nature remains neutral with regard to jurisdictional claims in published maps and institutional affiliations.

展　望

多点電極システムを用いた細胞外電位記録法

――ヒト iPS 心筋細胞および齧歯類神経細胞における医薬品・化学物質の作用解析――

多点電極システムは心筋細胞や神経細胞の電気的活動を簡便に細胞外電位記録するために開発され，これまで様々な研究分野において応用されてきている。近年，本システムを使って医薬品の心臓安全性評価法や化学物質リスク評価法の開発が進められ，これら評価法の標準化について国際的な議論が開始されている。本稿では，多点電極システムの概要，実験への応用例や今後の展開などについて概説する。

山崎　大樹，諫田　泰成，関野　祐子

1　多点電極システムとは

心筋細胞や神経細胞の詳細な電気生理学的特性を調べるには，Neher と Sakmann がノーベル生理学・医学賞を受賞したことでも有名なパッチクランプ法[1]によりイオン電流を測定する方法が最適である。この方法で各種のイオン電流を詳細に記録するためには，外部環境（蛍光灯や各種電源等）からの電気的ノイズの影響を取り除くことを目的として金網のシールドによって顕微鏡・サンプルを囲み，外部からの振動を除去するための除振台を必要とするなど非常に大掛かりなセットが必要である。さらに，先端の径が 1 μm ほどのガラス電極を精密マニピュレーターによって単一細胞へ接触させ僅かな陰圧を保つことによりギガオームシール（細胞膜とパッチ電極間で，ピペット内外の抵抗が 1 ギガオーム以上となる強固な抵抗）を形成させて，漏洩電流を最小限に抑える必要がある。このようにパッチクランプ法によって電気生理学的特性を調べるには，大掛かりなセットに加えて相当に熟練された正確なテクニックが必要である。ところが，医薬品の安全性評価や化学物質のリスク評価では数多くの化合物が対象となるためハイスループット性が強く要求される。したがって，パッチクランプ法での詳細な解析を行うことは，副作用などのメカニズム解明には必要であっても，これらリスク評価で利用することは非現実的である。

近年，多点電極（micro-electrode array：MEA）システムを使って医薬品の心臓安全性評価法や化学物質リスク評価法が開発され，これら評価法の標準化について国際的な議論が開始されている。1997 年に世界で初めて商業製品化された MEA システムが原型であるが，大量のデータ処理が可能になったことから近年になって急速に利用が進んでいる。MEA システムに用いられるプローブには平面に複数の微小電極がパターニングされており，その上に試料を載せて，細胞外電位（field potential：FP）を計測する。特徴を列挙すると次のようになる。①平面微小電極のインピーダンスは非常に小さく，外来ノイズの影響を受けにくいため，シールドや除振台等の特別な実験設備を必要としない。②低ノイズ故に高い SN 比が得られ，急性組織片や未成熟な幹細胞由来分化細胞の微弱応答も簡単・確実に計測できる。さらに，③平面微小電極上に試料を載せた状態で培養でき，細胞に電極を刺入しないことから，安定した状態を保ったまま数週間から数ヶ月にわたって計測が可能である。

現在，MEA システムとして MED64（アルファメッドサイエンティフィック社，日本），Maestro（Axion BioSystems 社，米国），MEA2100－Systems・Mul-

表 1　代表的な MEA システムメーカーとデバイス名や測定プローブ・プレートの詳細

メーカー	本社所在地	デバイス名	ウェル数	電極数
アルファメッドサイエンティフィック社	日本	MED64	1	64
			4	16
			8	8
Axion BioSystems 社	アメリカ	Muse	1	64
		Maestro	12	64
			48	16
			96	8
Multi Channel Systems 社	ドイツ	MEA2100-Systems	1	60
			6	9
		Multiwell-MEA-Systems	24	12
			72	4
			96	3

Field Potential Recording Method Using Micro-Electrode Array System: Cellular Responses in Human iPSC-Derived Cardiomyocytes and Rodent Brain-Derived Neurons.

本稿にある「医薬品」および「化学物質」は，それぞれ日本薬局方および化審法（化学物質の審査および製造等の規制に関する法律）記載の定義に従うものとする。

tiwell-MEA-Systems（Multi Channel Systems 社，ドイツ）などが日米欧から販売されており，様々なアプリケーションで使用されるようになってきた。表1にメーカー・デバイス名・プレートあるいはプローブのウェル数・1ウェルあたりの電極数をまとめたので参照いただきたい。

現在，MEA を用いたアプリケーションとして最も開発が進んでいるのが，ヒト iPS 細胞由来心筋細胞（ヒト iPS 心筋細胞）を用いた医薬品の心臓安全性評価系，ならびにげっ歯類の胎児培養神経細胞を用いた化学物質のリスク評価系である。筆者らは，これらの方法の標準化を目指して様々な化合物を用いて試験法の再現性の検証に取り組んでおり，これら二つについての最新情報と方法論・課題等を以下にご紹介したい。

2　MEA システムによるヒト iPS 心筋細胞を用いた医薬品の安全性評価法

新薬の承認申請にはヒトへの医薬品の安全性を評価する安全性薬理試験の実施が求められている。その試験では現在，致死性の多形性心室頻拍（torsade de pointes：dP）の主な原因である hERG チャネル（心臓において心電図の QT 間隔を主に規定している細胞膜上のタンパク質）の阻害作用を調べる *in vitro* 非臨床試験とヒトの心電図の QT 延長作用を調べる臨床試験が行われている。しかし hERG チャネル阻害や QT 延長は必ずしも TdP 誘発にはつながらないことや，他のタイプの催不整脈性を予測できないことなどの課題があり，非臨床試験の段階でヒトへの安全性をこれまでよりも正確に評価する方法が求められている。ヒト iPS 細胞技術の登場によりヒト心筋細胞を使った試験が可能となり，ヒト iPS 心筋細胞を用いた試験系の開発と安全性薬理試験への利用に大きな期待が寄せられている。

筆者ら，国立医薬品食品衛生研究所薬理部では，ヒト iPS 心筋細胞を利用した医薬品の心臓安全性評価系の構築に世界に先駆けて取り掛かった[2]。新規試験法においては，ハイスループット性に優れ簡便で高い再現性が期待できる MEA システムを採用した（図 1A, B）。細胞外電位の 1 st ピークから次の 1st ピークまでの間隔は inter-spike interval（ISI）と呼ばれ，拍動間隔を表す（図 1C）。心筋細胞は電気刺激により心筋細胞に発現している Na^+ チャネル，Ca^{2+} チャネル，K^+ チャネルを適切なタイミングで活性化あるいは不活性化させて活動電位（action potential: AP）を生じる。心室筋細胞における活動電位の持続時間（AP duration: APD）は細胞外電位波形の 1st ピークと 2nd ピークの間隔を示す FP の持続時間（FP duration: FPD，図 1C）とある程度相関しており[3]，さらにこれらは心電図における QT 間隔に相当する（図 2A）。TdP の発生に主に関与している hERG チャネル阻害は，FPD の延長により評価でき，

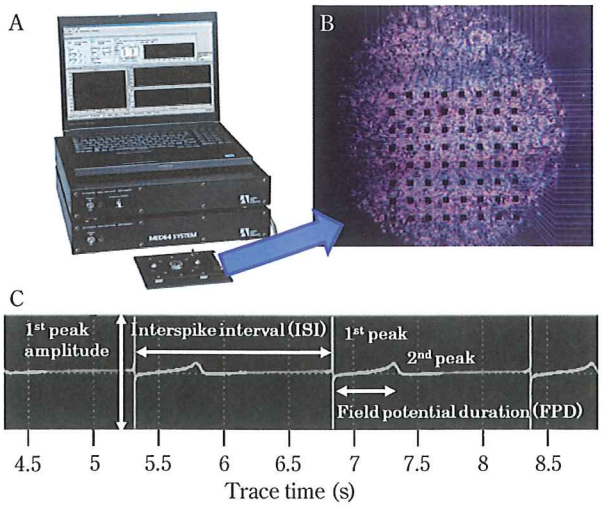

アルファメッドサイエンティフィック社製の多点電極システムである MED64（A）にヒト iPS 心筋細胞のシート（B）をプローブ上に播種し，細胞外電位波形（C）を取得した。1st ピークから次の 1st ピークまでを Inter spike interval（ISI），1st ピークから 2nd ピークまでを Field potential duration（FPD）という。文献 3 および 8 の一部を改変。

図 1　ヒト iPS 心筋細胞における多点電極システムの活用

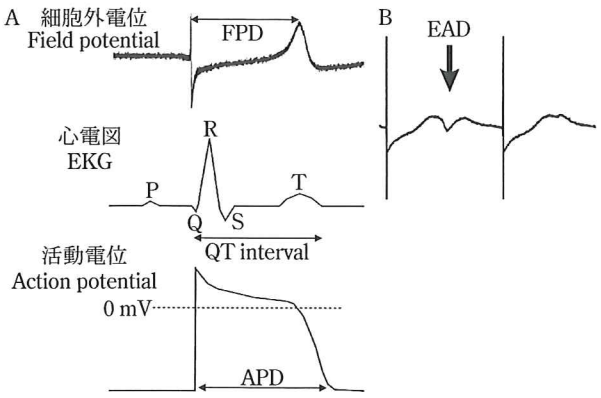

(A) 細胞外電位波形（上段）の FPD に対して心電図波形（中段）の QT 間隔および活動電位波形（下段）の APD80（活動電位がピークから 80%減衰したときの間隔）が時間的に相当する。(B) 細胞外電位波形における異常波形の一つである EAD を示した。

図 2　細胞外電位波形，心電図波形，活動電位波形の比較と細胞外電位波形における異常波形

また TdP の前触れとして考えられている Early after-depolarization（EAD）も観測できる（図 2B）。この試験法の予測性の高さは，hERG チャネルおよび Ca チャネルを同時に阻害するベラパミルの評価で見ることができる。現行の試験法においてベラパミルは，hERG チャネル阻害のみが評価され TdP リスクを有する物質に分類されるが，Ca チャネル阻害作用がこれを相殺するため，実際には TdP を誘発しない。一方，ヒト iPS 心筋細胞と MEA システムを用いた評価系では，Ca チャネル阻害作用も同時に確認できるため，TdP リスクを含めたベラパミルの安全性を正確に評価することができる

ことがわかった。

ヒトiPS心筋細胞には，心臓を構成する複数の細胞が含まれている。実際，ヒトiPS心筋細胞を培養して，単一細胞での活動電位波形を記録すると，心房筋タイプ，心室筋タイプや洞房結節タイプなど複数の活動電位波形が得られる[4]。二次元で細胞を高密度に培養すると，細胞同士は融合し心筋細胞シートが形成され自発的な活動電位および自律拍動がシート全体で同期し，心電図と類似した波形を記録することができる。筆者らは高密度培養を使った方法を標準化して，多施設で再現性を確認することとした。エーザイ（産），東邦大学（学），国立衛研（官）の3者において同一機器（MED64，アルファメッドサイエンティフィック社）・同一細胞（iCell cardiomyocytes, Cellular Dynamics International社）・同一化合物（選択的hERGチャネル阻害薬，E-4031）を用いて実験方法の再現性を検証するバリデーション試験を行った（プレバリデーション試験）。1プローブあたり13000～26000細胞を播種（はしゅ）し，E-4031によるFPD延長率やEADが検出された濃度を比較したところ，3施設間の差は3倍以内に収まっていた[5]。MEAシステムにおいて，FPDは医薬品の薬理反応を評価する上で重要なパラメーターの一つである。筆者らは，計測時の高周波域通過フィルターの違いによって，FPDの値が異なることを明らかにした[6]。さらに播種する細胞密度を厳密に規定することで，標本ごとのばらつきや施設間の差を最小限にできると考えられたことから，播種細胞数の検討を行った。その結果，細胞数依存的に拍動数が減少する一方で，設定したクライテリア（1stピーク振幅≥±200 μV, 2ndピーク振幅≥15 μV, inter-spike interval<1715 msec，FPDcF≥340 msec）を満たす電極数は増加した。1stピーク振幅や2ndピーク振幅の大きさも十分なことから，iCell cardiomyocytesについては1プローブあたり25000細胞以上で播種することが望ましいと結論づけた[6]。

筆者らは最近，厳密な実験条件のもと4施設での大規模検証試験を行い，二つの論文を報告した。一つは，ヒトiPS心筋細胞から得られた拍動数に相当するISIとQT間隔に相当するFPDの関係性が，5000人規模の心拍数とQT間隔との関係を調べた大規模住民研究（フラミンガム心臓研究[7]）の成績に類似していること，およびTdPを誘発する薬剤が，徐脈になるほどFPDを延長することを明らかにしたものである[8]。また，TdPリスクの異なる60化合物を選択し，ヒトiPS心筋細胞における薬剤応答性を様々な薬剤濃度で評価した。得られた結果を実際の臨床データであるCredibleMedsと比較したところ，薬剤誘発性の致死性不整脈の発生リスクの予測度が83％と非常に高かった[9]。

以上のデータは，1種類のヒトiPS心筋細胞と1種類の機器により得られた結果である。筆者らが，ヒトiPS心筋細胞とMEAシステムを組み合わせた医薬品の心臓安全性評価系の構築を始めた頃は，性質が安定しており恒常的に供給可能なヒトiPS心筋細胞は1種類のみであった。近年ではMEAシステムの開発が進むにつれてヒトiPS心筋細胞にもバリエーションが増え，今では日本企業を含む複数のベンダーからヒトiPS心筋細胞が販売され，また筆者らの研究班の成果としてアカデミアからのヒトiPS心筋細胞も検証実験に用いることが可能かどうかの検討を行っている段階である。今後，性質の異なる複数のヒトiPS心筋細胞をMEAシステムで評価することで，ヒトiPS心筋細胞を用いた医薬品のTdPリスク予測に対してなんらかのクライテリアが見いだせるものと期待している。

3　MEAシステムを用いた化学物質リスク評価法

これまで医薬品安全性評価へのMEAシステムの応用を述べてきたが，ここでは神経細胞を用いたMEAシステムの応用を述べたい。当初MEAシステムは，海馬スライス標本での長期増強を記録するために開発されたデバイスである[10]。開発以降，海馬だけでなく大脳皮質[11]や脊髄[12]，網膜[13]などの急性スライス標本や初代培養神経細胞[14]，幹細胞由来神経細胞[15]へも応用されてきており，神経細胞の活動電位の細胞外記録に優れている。近年，化学物質の発達神経毒性評価系にもMEAシステムを応用しようとする動きが世界中で広がってきている。米国環境保護庁（Environmental Protection Agency：EPA）ではMEAシステムによる初代培養ラット大脳皮質神経細胞を用いた化学物質リスク評価法の検討を行った[16)~18)]。この報告では，評価すべき陽性・陰性対照物質（陽性対照物質：発達神経毒性を発現することが知られている化学物質，陰性対照物質：発達神経毒性を発現しないことが知られている化学物質）がいくつか挙げられている（表2）。筆者らも，厚生労働省科学研究費補助金（化学物質リスク研究事業）の支援を受けて，平成28年度よりMEAシステムによる凍結ラット胎児海馬神経細胞を用いた神経ネットワーク評価系の構築を開始した（図3A）。現在筆者らは，群馬大学・白尾研究室から提供された細胞を用いて再現性の高いデータの取得を目指してプロトコル整備を行い，EPAと情報交換しながら評価系の構築を行っている。また，その他にも国際的な動向として発達神経毒性以外にもMEAシステムを化学物質リスク評価に応用しようとする動きがある。その動きの中心になっているのは米国の保健環境科学研究所（HESI）である。HESIは，産官学等の戦略的パートナーから科学者の参画を通じて地球の健康と環境に関する課題を解決するために支援を行っている非営利機関である。HESIでの課題の一つとしてNeuTox（イメージングや形態および神経病理学的な指標等

表2　評価すべき陽性・陰性対照物質一覧

陽性対照物質	分　類	CAS#
ビククリン	$GABA_A$ アンタゴニスト	40709-69-1
ビフェントリン	電位依存性ナトリウムチャネル・殺虫剤	82657-04-3
カルバリル	アセチルコリンエステラーゼ阻害剤	63-25-2
クロルピリホス	アセチルコリンエステラーゼ阻害剤	5598-15-2
シフルトリン	電位依存性ナトリウムチャネル・殺虫剤	68359-37-5
デルタメトリン	電位依存性ナトリウムチャネル・殺虫剤	52918-63-5
ジアゼパム	$GABA_A$ アンタゴニスト	439-14-5
ドウモイ酸	グルタミン酸受容体アンタゴニスト	14277-97-5
フィプロニル	$GABA_A$ アンタゴニスト	120068-37-3
フルオキセチン	セロトニン選択的再取り込み阻害剤	114247-09-5
イミダクロピリド	ニコチン性アセチルコリン受容体・殺虫剤	138261-41-3
ケタミン	NMDA 受容体アンタゴニスト	33795-24-3
鉛	重金属	6080-56-4
L-グルタミン酸	グルタミン酸受容体アゴニスト	19285-83-7
リンデン	$GABA_A$ アンタゴニスト	58-89-9
メチル水銀	重金属	115-09-3
ムッシモール	$GABA_A$ アゴニスト	18174-72-6
ニコチン	ニコチン性アセチルコリン受容体アゴニスト	54-11-5
ペルメトリン	電位依存性ナトリウムチャネル・殺虫剤	52645-53-1
RDX	$GABA_A$ アンタゴニスト	121-82-4
トリメチルスズ	重金属	56-24-6
バルプロ酸	抗けいれん薬	1069-66-5
ベラパミル	電位依存性ナトリウムチャネル阻害剤	152-11-4
陰性対照物質	**分　類**	**CAS#**
アセトアミノフェン	Cox-2 阻害剤	103-90-2
アモキシシリン	抗生物質	26787-78-0
グリホサート	除草剤	1071-83-6
パラコート	除草剤	1910-42-5
サッカリン	甘味料	82385-42-0
サリチル酸	植物ホルモン	69-72-7
D-ソルビトール	甘味料	50-70-4

（文献 16 の一部を改変）

の連携により，既知の神経毒性・発達神経物質の曝露（ばくろ）によって生じる毒性の予測が可能なバイオマーカーの同定を目的とした活動）がある。神経細胞ネットワークの活動を指標として既知の神経毒性の曝露による毒性予測が可能かを検証する MEA サブチームでは，MEA プラットフォームにおけるラット神経細胞や脳スライス，ヒト iPS 神経細胞の違いを比較するとともに，てんかんを引き起こすことが知られている医薬品を用いたプレバリデーションの実施内容について現在議論されている。

MEA システムを用いて神経ネットワークの形成を評価する場合の指標について，現状では有効的かつ効果的な指標は決まっていない。そのため，10 を超えるパラメーターについて解析し，評価するのに最適なパラメーターを検討する必要がある。すでに解析パラメーターに関する論文が報告されている[19]ので，それを例にとって説明する。

未成熟な胎児神経細胞は，頻度は低いが神経細胞の活性化を示すスパイクと呼ばれる電位変化を生じる。この電位変化は非常に短い（数 msec）間に起こるが，これを MEA システムによって検出する。MEA システムではスパイクの検出閾値をノイズレベルの 6〜8 倍に設定することでノイズの検出を防いでおり，検出閾値を超えたスパイクはラスタープロットとして表される（図 3B）。神経細胞の成熟とともにスパイクの発生頻度は増加し，やがて神経細胞の突起同士がシナプスを形成することで神経ネットワークを構築する。神経ネットワークの構築により各神経細胞で独立に発生しているスパイクが同期し，最終的にはバーストやネットワークスパイクと呼ばれる連続的でウェル中の複数の電極で同期した電位変化が起こるようになる（図 3C）。スパイクやバーストの発生を電極ごとの発生頻度として算出するためには，それらの現象が起こっている電極の数についても算出する必要がある。1 ウェルで 1 分間に発生したスパイクを活性化電極数（Active electrodes，1 分間に 5 回以上のスパイクを生じた電極数）で除算した値を MFR（Mean firing rate）という（図 4）。さらにそれぞれの現象が発生するまでの間隔，同期して生じるスパイクやバーストの発生頻度，持続時間，発生までの間隔等の合計 12 のパラメーターについて算出し（表 3），主成分分析などによって評価指標としてより相関性の高いパラメーターを提案することになる。今後は，現在構築中の評価系において上述の陽性対照物質や陰性対照物質を急性投与や慢性投与によりリスク評価を行う予定である。

神経ネットワーク形成の機能評価について，現在はげっ歯類の神経細胞を用いて評価が行われている。動物実験代替の観点からヒト iPS 神経細胞を利用できることが理想であるが，ヒト iPS 神経細胞はそれのみの培養では成熟しにくいことが知られている。ヒト iPS 神経細胞においてスパイクが検出されるためには長期間（数か月程度）の培養期間を設けるか，グリア細胞との共培養系あるいはグリア細胞の条件培地を用いる系にするかである。しかし培養の長期化は評価の複雑化につながり，グリア細胞との共培養や条件培地の使用は再現性

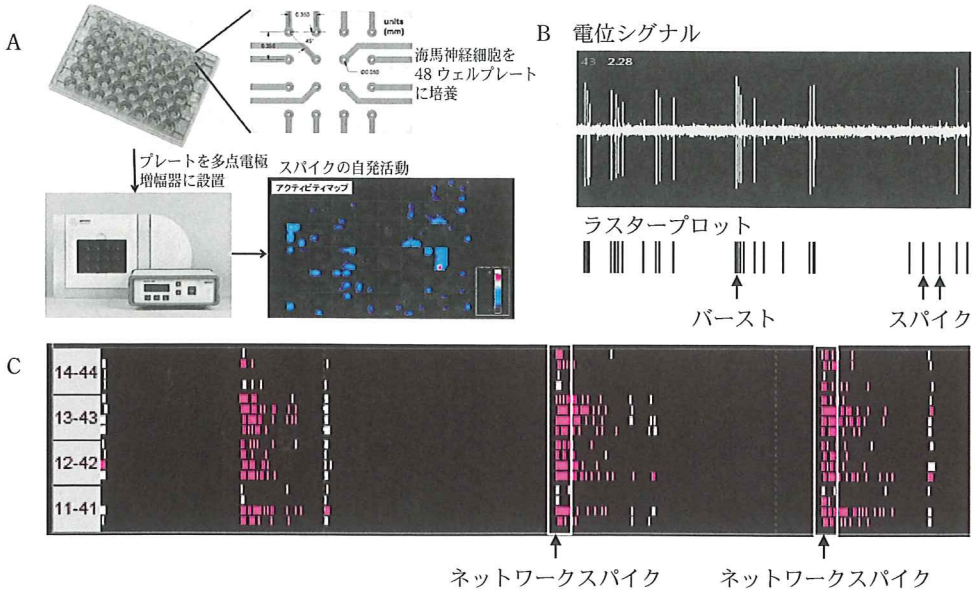

A. 各ウェルに 16 個の電極が埋め込まれている 48 ウェルプレートにラット海馬神経細胞を 1 ウェルあたり 50000 細胞を播種・培養し，Axion 社製多点電極システムに設置し，神経活動を記録する。神経活動（スパイク）がアクティビティマップとして疑似カラー表示される。B. 1 電極ごとに電位シグナルが検出され，検出閾値よりも大きなシグナルはラスタープロットとして表示される。ラスタープロット 1 本 1 本はスパイクを表しており，スパイクがまとまって発生した場合にはバーストと呼ばれる。C. 1 ウェル（16 電極）のラスタープロット。同期したスパイクをネットワークスパイクと呼ぶ。白のラスタープロットは単一のスパイク，赤のラスタープロットはバーストを表している。

図 3　神経細胞を用いた多点電極システム

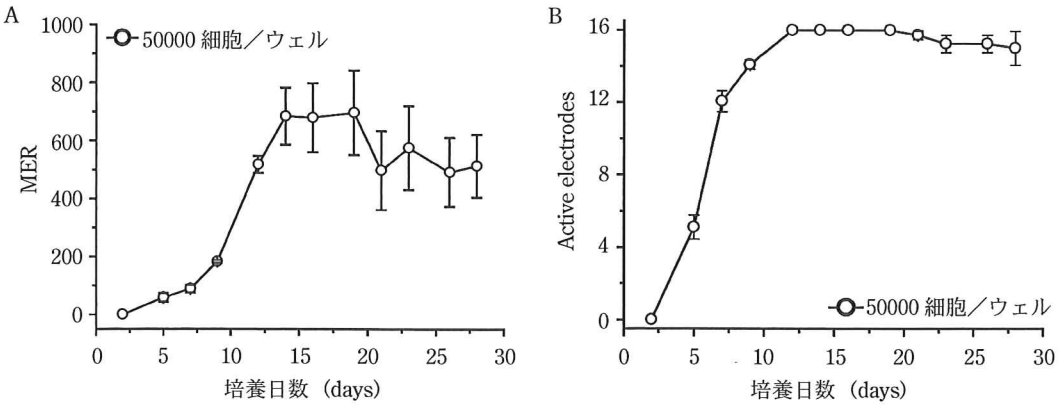

(A) 28 日目までの神経活動を経時的に表した。4 ウェル分の平均値を示す。縦軸は 1 分間に観察された 1 電極あたりのスパイク数を示した。培養 14 日目から 19 日目では 1 電極あたりのスパイク数が維持された。(B) A と同じウェルでの 1 分間に 5 回以上スパイクが記録された電極数（Active electrodes）の経時変化を示した。培養日数 7 日目にはすでに半数以上の電極が活性化状態となり，12 日目以降はほぼすべての電極が活性化していた。その状態は培養 28 日目まで持続した。

図 4　経時的な神経活動計測

を担保するのが難しいと考えられることから，ヒト iPS 神経細胞を用いた MEA システムでの評価系を構築するには更なる検討が求められている。

4　おわりに

本稿では，心筋細胞や神経細胞の電気的活動を簡便に測定可能な MEA システムの開発の背景と，現在応用されている二つのアプリケーション例について紹介した。ヒト iPS 心筋細胞を用いた医薬品の心臓安全性評価では，日本国内のみならず世界規模でその評価に係（かかわ）るガイドライン改訂の動きがあり，ヒト iPS 心筋細胞と MEA システムを組合せた評価系の導入が検討されている。

また，神経毒性における化学物質リスク評価における MEA システムの利用は今まさに開発段階であり，*in vivo* 試験を主とする医薬品の薬理試験や化学物質の発達神経毒性評価系への導入の提案に向けて世界規模で動いている。今後，ますます MEA システムの応用は増えて

表3　多点電極システムにおける神経ネットワーク形成の解析パラメーター

解析パラメーター	説　明
スパイク頻度	1電極あたり1分間のスパイク数
バースト頻度	1電極あたり1分間のバースト数
バースト間隔	1電極におけるバーストの間隔
起バースト電極	バーストが観察された電極数
バースト内のスパイク頻度	バースト中に生じたスパイクの頻度
バースト内のスパイクの割合	バースト中に生じたスパークの割合
バースト間隔の変動係数	バーストの間隔の標準偏差
バースト内のスパイク間隔の変動係数	バースト中に観察されたスパイクの間隔の標準偏差
ネットワークスパイク頻度	1分間に生じた同期したスパイク数
ネットワークスパイク間隔	1分間に生じた同期したスパイクの間隔
ネットワークスパイクピーク	1分間に生じた同期したスパイクが観察された電極数
平均相関係数	1対の電極ごとの組合せを係数を用いて算出

（文献19の一部を改変）

いくものと思われる。

謝辞　本研究は，厚生労働省科学研究費補助金（H24-Iyaku-Shitei-030 to YS）ならびに国立研究開発法人日本医療研究開発機構（AMED）の医薬品等規制調和・評価研究事業委託研究「ヒトiPS分化細胞技術を活用した医薬品の次世代毒性・安全性評価試験系の開発と国際標準化に関する研究」（#15mk0104053h0101 for 2015, #16mk0104027j0002 for 2016 to YS），厚労省化学研究費補助金（化学物質リスク研究事業）「発達期における統合的な遅発性神経毒性試験法の開発」（H28-化学-一般-003 to YK）のサポートにより実施されました。

文　献

1) E. Neher, B. Sakmann : *Nature*, **260**, 799 (1976).
2) Y. Kanda, D. Yamazaki, J. Kurokawa, T. Inutsuka, Y. Sekino : *J. Pharmacol. Toxicol. Methods.*, **81**, 196 (2016).
3) Y. Ide, D. Yamazaki, Y Kanda, Y. Sekino : *Kokuritsu Iyakuhin Shokuhin Eisei Kenkyusho Hokoku*, in press.
4) J. Zhang, G. F. Wilson, A. G. Soerens, C. H. Koonce, J. Yu, S. P. Palecek, J. A. Thomson, T. J. Kamp : *Circ. Res.*, **104**, e30 (2009).
5) Y. Nakamura, J. Matsuo, N. Miyamoto, A. Ojima, K. Ando, Y. Kanda, K. Sawada, A. Sugiyama, Y. Sekino : *J. Phamacol. Sci.*, **124**, 494 (2014).
6) K. Asakura, S. Hayashi, A. Ojima, T. Taniguchi, N. Miyamoto, C. Nakamori, C. Nagasawa, T. Kitamura, T. Osada, Y. Honda, C. Kasai, H. Ando, Y. Kanda, Y. Sekino, K. Sawada : *J. Pharmacol. Toxicol. Methods.*, **75**, 17 (2015).
7) A. Sagie, M. G. Larson, R. J. Goldberg, J. R. Bengtson, D. Levy : *Am. J. Cardiol.*, **70**, 797 (1992).
8) W. Yamamoto, K. Asakura, H. Ando, T. Taniguchi, A. Ojima, T. Uda, T. Osada, S. Hayashi, C. Kasai, N. Miyamoto, H. Tashibu, T. Yoshinaga, D. Yamazaki, A. Sugiyama, Y. Kanda, K. Sawada, Y. Sekino : *PLoS One*, **11**, e0167348 (2016).
9) H. Ando, T. Yoshinaga, W. Yamamoto, K. Asakura, T. Uda, T. Taniguchi, A. Ojima, R. Shinkyo, K. Kikuchi, T. Osada, S. Hayashi, C. Kasai, N. Miyamoto, H. Tashibu, D. Yamazaki, A. Sugiyama, Y. Kanda, K. Sawada, Y. Sekino : *J. Pharmacol. Toxicol. Methods.*, in press.
10) H. Oka, K. Shimono, R. Ogawa, H. Sugihara, M. Taketani : *J. Neurosci. Methods.*, **93**, 61 (1999).
11) M. Kobayashi, K. Imamura, T. Sugai, N. Onoda, M. Yamamoto, S. Komai, Y. Watanabe : *Eur. J. Neurosci.*, **12**, 264 (2000).
12) H. Zhang, N. Robinson, C. Wu, W. Wang, M. A. Harrington : *PLoS One*, **5**, e11696 (2010).
13) L. Li, Y. Hayashida, T. Yagi : *Vision Res.*, **45**, 263 (2005).
14) S. Honma, T. Shirakawa, Y. Katsuno, M. Namihira, K. Honma : *Neurosci. Lett.*, **250**, 157 (1998).
15) Y. Fujimoto, M. Abematsu, A. Falk, K. Tsujimura, T. Sanosaka, B. Juliandi, K. Semi, M. Namihira, S. Komiya, A. Smith, K. Nakashima : *Stem Cells.* **30**, 1163 (2012).
16) E. R. McConnell, M. A. McClain, J. Ross, W. R. Lefew, T. J. Shafer : *Neurotoxicology.* **33**, 1048 (2012).
17) P. Valdivia, M. Martin, W. R. LeFew, J. Ross, K. A. Houck, T. J. Shafer : *Neurotoxicology.* **44**, 204 (2014).
18) J. P. Brown, D. Hall, C. L. Frank, K. Wallace, W. R. Mundy, T. J. Shafer : *Toxicol. Sci.*, **154**, 126 (2016).
19) E. Cotterill, D. Hall, K. Wallace, W. R. Mundy, S. J. Eglen, T. J. Shafer : *J. Biomol.. Screen.* **21**, 510 (2016).

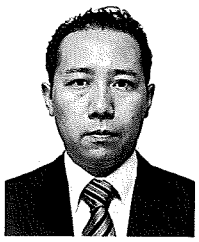

山崎大樹（Daiju Yamazaki）
国立医薬品食品衛生研究所薬理部（〒158-8501 東京都世田谷区上用賀1-18-1）。名古屋市立大学大学院薬学研究科博士後期課程修了。薬学博士。≪現在の研究テーマ≫医薬品・化学物質のMEAシステムによる評価系の構築と国際標準化。≪趣味≫テニス，スポーツ観戦，ドライブ。
E-mail: daiju-y@nihs.go.jp

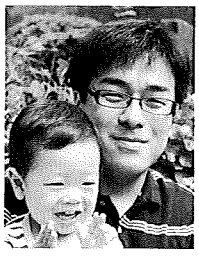

諫田泰成（Yasunari Kanda）
国立医薬品食品衛生研究所薬理部（〒158-8501 東京都世田谷区上用賀1-18-1）。東京大学大学院薬学系研究科修士課程修了。博士（薬学）。≪現在の研究テーマ≫幹細胞を用いた医薬品および化学物質の安全性評価と国際標準化。≪趣味≫旅行，食べ歩き，子育て。
E-mail: kanda@nihs.go.jp

関野祐子（Yuko Sekino）
国立医薬品食品衛生研究所薬理部（〒158-8501 東京都世田谷区上用賀1-18-1。東京大学薬学部卒。医学博士。≪現在の研究テーマ≫ヒトiPS分化細胞技術を活用した医薬品の次世代安全性評価試験系の開発と国際標準化。
E-mail: yukos@mol.f.u-tokyo.ac.jp

電気学会論文誌 A（基礎・材料・共通部門誌）
IEEJ Transactions on Fundamentals and Materials
Vol.136 No.2 pp.99-104 DOI: 10.1541/ieejfms.136.99

Paper

Visualization of Spatially Distributed Bioactive Molecules using Enzyme-Linked Photo Assay

Hikaru Mabuchi* Student Member, HongYao Ong* Associate
Kazunori Watanabe* Non-member, Sachiko Yoshida* Non-member
Naohiro Hozumi*a) Senior Member

(Manuscript received March 18, 2015, revised Oct. 4, 2015)

In this paper, we propose a new simple device for visualizing bioactive molecules with a fine spatial resolution by using a membrane in which a specific enzyme is immobilized. The layer produces fluorescence after association with a specific substance. The layer, on which a biological tissue is to be mounted, is deposited on a quartz substrate that is used as a light guide to introduce UV light to the layer. Substance release is observed by a CCD camera from the opposite side of the substrate. In order to shorten the experiment time, we had automated the optical device. The paper also describes the reduction of background fluorescence by means of image processing technique. Images were acquired by employing two UV-LEDs with slightly different angle. Image processing was performed to separate background and target fluorescence by means of independent component analysis. Finally the release of GABA(γ-aminobutyric acid) and glutamate from specific layers in rat cerebellum was successfully observed. It is expected that, using this method, both real-time transmitter release and its response to medicine can be observed.

Keywords : bioactive molecules, enzyme-linked photo assay, independent component analysis

1. Introduction

Light guide is composed of a dielectric material that can enclose the light propagation. In addition to being applied to communication, it is useful for sensing as well. In chemical sensing the surface of the light guide has to be coated with some specific chemical that may change its optical property depending on chemical reactions. Such a function can be applied to chemical imaging, if the light guide has a flat surface. This study proposes an application of two-dimensional light guide, of which surface is chemically modified, to biochemical imaging.

Neurotransmitter molecules released from neurons are not only regulators of neuronal transduction but also indicators of neuronal conditions. Glutamate and γ-aminobutyric acid (GABA) are known as typical transmitters in brain cortex that play important roles as stimulator and suppresser, respectively. Lack of balance in the release of glutamate and GABA may lead to autism, epilepsy or Parkinson's disease[(1)(2)].

In order to observe the spatio-temporal release in cerebellar cortex, we have newly proposed the enzyme-linked photo assay system, which is realized even using normal CCD camera, and observed GABA release in developing cerebellar slice using either new or authorized methods[(3)].

In this paper, we propose a new simple device for this purpose by using a reactive layer in which a specific enzyme is immobilized, and produces fluorescence after association with a specific substance released from mounted slice. This layer is bound a quartz substrate that is used as a light guide for UV light excitation. Fluorescence derived from a substance is observed by a CCD camera from the opposite side of the substrate.

The paper describes the reduction of background fluorescence by means of image processing technique. Finally it will be shown that the release of transmitters from specific layers in rat cerebellum was successfully observed.

2. Specimen Preparation and Photo Excitation System

Imaging of neurotransmitter release was monitored the reaction of oxidoreductases generating reduced nicotinamide adenine dinucleotide (NAD^+) or diphosphonucleotide ($NADP^+$). For glutamate and GABA, we used glutamate dehydrogenase and GABA disassembly enzyme (GABase), respectively.

Enzymes were covalently immobilized on the quartz glass substrate using a silane coupling agent and a crosslink agent. The substrate was as thick as 1 mm. Stoichiometrically generated NADH or NADPH emits 480 nm fluorescence after excitation at 340-365 nm.

Existence of glutamate and GABA lead to fluorescence when co-existing with specific enzyme and co-enzyme. A glass substrate on which specific enzyme is coated is in contact with the biological specimen. A chamber space is created around the specimen. The space is filled with buffer liquid and co-enzyme. On the glass substrate therefore, the specimen is in contact with both enzyme and co-enzyme.

Consequently glutamate or GABA, that is released from the tissue spontaneously by stimulation, makes an oxidation-reduction reaction on the substrate. Although both glutamate and GABA do not produce fluorescence by themselves, NAD(P)H that is created as the result of the above chemical reaction makes fluorescence. As the ratio of glutamate or GABA and NAD(P)H is 1:1, the

a) Correspondence to: Naohiro Hozumi. E-mail: hozumi@icceed.tut.ac.jp
* Toyohashi University of Technology
1-1, Hibarigaoka, Tenpaku, Toyohashi 441-8580, Japan

fluorescence can be correlated to the amount of released glutamate or GABA.

In the experiment, rat cerebellum was sliced sagittally at 400 μm thick and incubated in oxygen-aerated HEPES-Na^+ buffer for 40 min. The slice was placed on the quartz glass substrate with both $NADP^+$ and α-ketoglutarate. Figure 1 shows the schematic diagram of the observation system including the device. The enzyme was immobilized covalently on the glass as shown in Fig. 2. Figure 3 shows chemical reactions taking place on the substrate. $NADP^+$ (nicotinamide adenine dinucleotide phosphate) changes into NADPH (reduced nicotinamide adenine dinucleotide phosphate) just as glutamate and GABA degeneration. Synthesized NADPH was illuminated by 360 nm surface UV-LED, and emitted the 480 nm fluorescent light observed by cooled CCD (ORCA ER, Hamamatsu Photonics). The quartz substrate can be recognized as a light guide to illuminate the surface of the substrate.

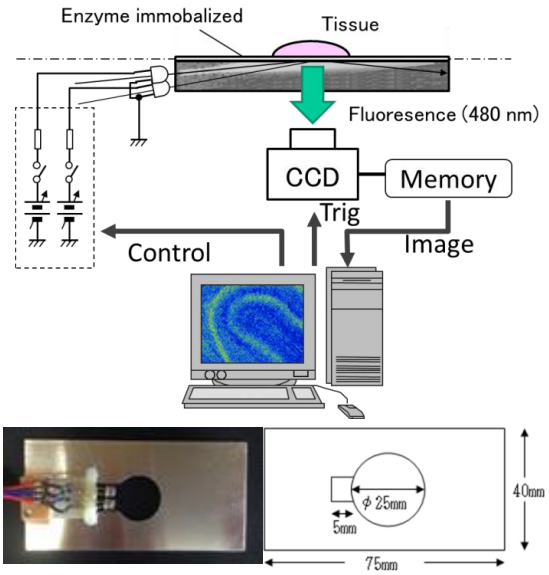

Fig. 1. Schematic diagram of the observation system including the device and its outlook

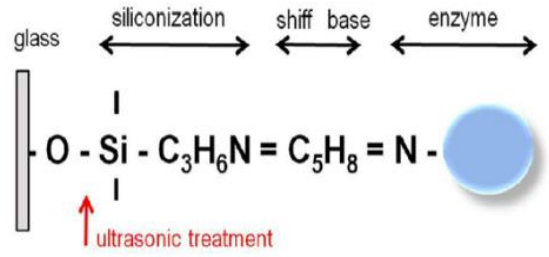

Fig. 2. Immobilized enzyme

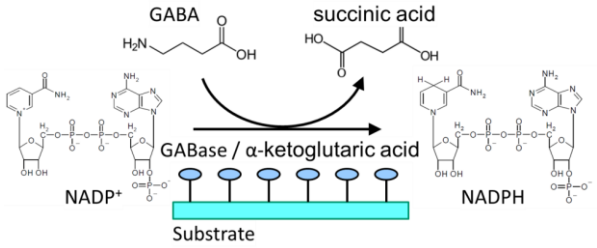

Fig. 3. Chemical reaction on the substrate

3. Image Processing

The fluorescent light detected by the CCD camera is divided into target light and background light. As significant intensity of background light is detected, it is assumed that fluorescence is excited by the light that is refracted on the interface between the substrate and tissue system including the layer. The light, being generated by LEDs and propagates though the substrate, can be decomposed into plane waves with different angles of propagation. Each plane wave transfers across the enzyme layer and comes into the tissue. We assume that both target and background light were predominantly excited by normal light. As the background light significantly damage the quality of the image, it should be reduced as much as possible. Making use of the evanescent light may be a solution, however, it may make the system complicated, and the target light may be not as significant as this case. Therefore we tried to reduce the background by means of a simple image processing.

Assuming that the light is a plane wave and scatter can be neglected, wave propagation and detected fluorescence can be illustrated as Fig. 4. In the figure, fluorescence, attributed to the layer where the enzyme is fixed, is represented as I_0. This is

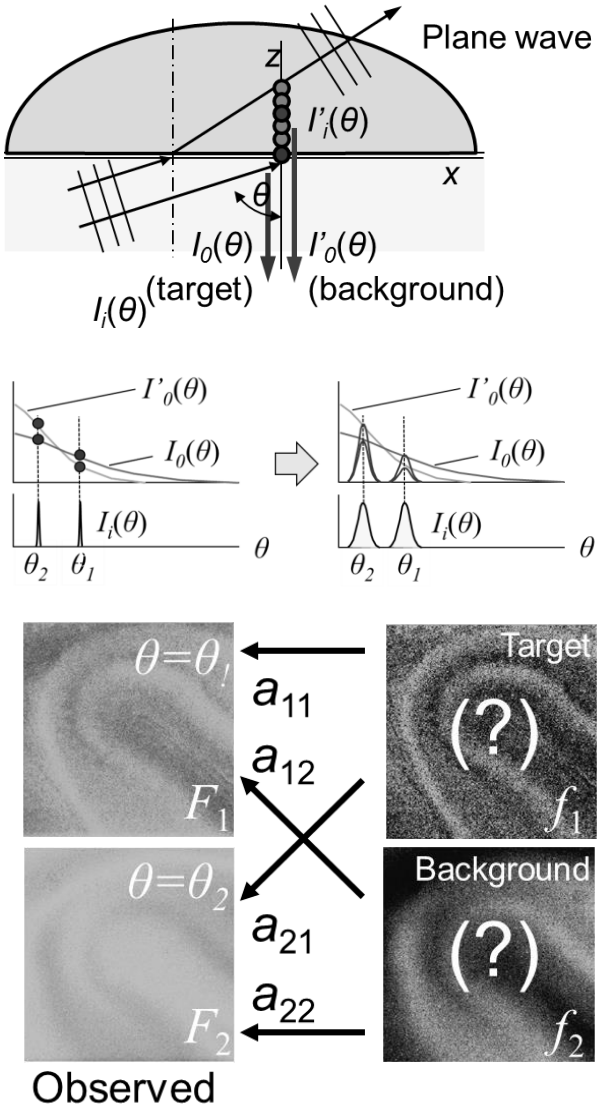

Fig. 4. Fluorescence detected by CCD camera

defined as to be the target. The fluorescence attributed to the tissue is represented as I'_0 . This is defined as to be the background. Both I_0 and I'_0 depends on the incident angle θ. The thickness of the quartz plate, which is used as a light guide, is as thick as 1 mm. As it is much thicker than the diameter of normal optical fiber it is relatively easy to introduce two kinds of lights of which angles of center axes are significantly different. In addition, in practice, they depend differently on the incident angle. As the result, the proportion (I_0/I'_0) is not the same along θ. This is true even if the incident angle has distributed.

As the result, the captured fluorescence with different angle of optical axis is composed of target and background fluorescence with different mixture ratios. This can be represented as:

$$\begin{pmatrix} F_1 \\ F_2 \end{pmatrix} = \begin{pmatrix} a_{11} & a_{12} \\ a_{21} & a_{22} \end{pmatrix} \begin{pmatrix} f_1 \\ f_2 \end{pmatrix} \quad \cdots\cdots (1)$$

where $F_1(x,y)$ and $F_2(x,y)$ are captured fluorescence image, $f_1(x,y)$ and $f_2(x,y)$ are spatial distributions of fluorescence as the target and background, a_{11}, a_{12}, a_{21}, a_{22} are constants. Although the image acquisition is sequential, ICA is performed by assuming that two images, $F_1(x,y)$ and $F_2(x,y)$ are acquired with a negligible time lag. Reproduced images $f'_1(x,y)$ and $f'_2(x,y)$ are calculated from F_1 and F_2. As the result of periodical acquisitions of F_1 and F_2, time dependent images of f'_1 and f'_2 are calculated. Eq. (1) can also be described using a matrix expression as:

$$\mathbf{F} = \mathbf{A} \cdot \mathbf{f} \quad \cdots\cdots (2)$$

The target and background fluorescence distribution can be calculated by applying $\mathbf{A}^{-1}$ to $\mathbf{F}$. In practice, only contrast of the image would be enough to recognize the distribution. In such a case $\mathbf{A}^{-1}$ can be represented as:

$$\begin{pmatrix} 1 & \alpha \\ \beta & 1 \end{pmatrix} \quad \cdots\cdots (3)$$

After capturing two images $\mathbf{F}_1$ and $\mathbf{F}_2$ by changing the angle of optical axis, the target and background images can be separated by finding appropriate numbers for α and β. α and β can be tuned manually by monitoring the quality of reproduced image, however, the theory of independent component analysis (ICA) may be powerful for solving such a problem[4].

Stochastic distribution of pixel intensity in images f'_1 and f'_2 are represented as $p(y_{1i})$ and $p(y_{2j})$, where y_{1i} and y_{2j} represent the intensity.

$$\left.\begin{aligned} p(y_1) &\equiv \{p(y_{11}), \cdots, p(y_{1i}), \cdots p(y_{1n})\} \\ p(y_2) &\equiv \{p(y_{21}), \cdots, p(y_{2j}), \cdots p(y_{2n})\} \end{aligned}\right\} \quad \cdots\cdots (4)$$

$p(y_{1i}, y_{2j})$ represents the probability that the intensity of a pixel in image f'_1 is y_{1i} and that of the corresponding point in image f'_2 is y_{2j}. In other words $p(y_1)$ and $p(y_2)$ are probabilities that cases y_1 and y_2 take place, respectively, and $p(y_1, y_2)$ is the probability that cases y_1 and y_2 takes place simultaneously. Variables y_1 and y_2 are considered to be independent when

$$p(y_1, y_2) = p(y_1)p(y_2) \quad \cdots\cdots (5)$$

is established. Kullback-Leibler (K-L) parameter is often employed to indicate the independency of variables:

$$KL \equiv \sum_{i,j} p(y_{1i}, y_{2j}) \log \frac{p(y_{1i}, y_{2j})}{p(y_{1i})p(y_{2j})} \quad \cdots\cdots (6)$$

The K-L parameter is zero when two sets of variables y_1 and y_2 are completely independent together. In practice, α and β in Eq. (3), which determine the probabilities $p(y_1)$, $p(y_2)$ and $p(y_1, y_2)$, can be tuned so that the K-L parameter indicates the minimum.

The process of ICA is illustrated in Fig. 5. The equation described in the form of matrix indicates that two images, F_1 and F_2, derive from linear combination of unknown original images f_1 and f_2. If an appropriate inverse matrix can be found then the original images can be reproduced. However as the matrix to describe the linear combination is unknown as well, ICA algorithm is applied to find the most appropriate matrix (as the inverse matrix). In the

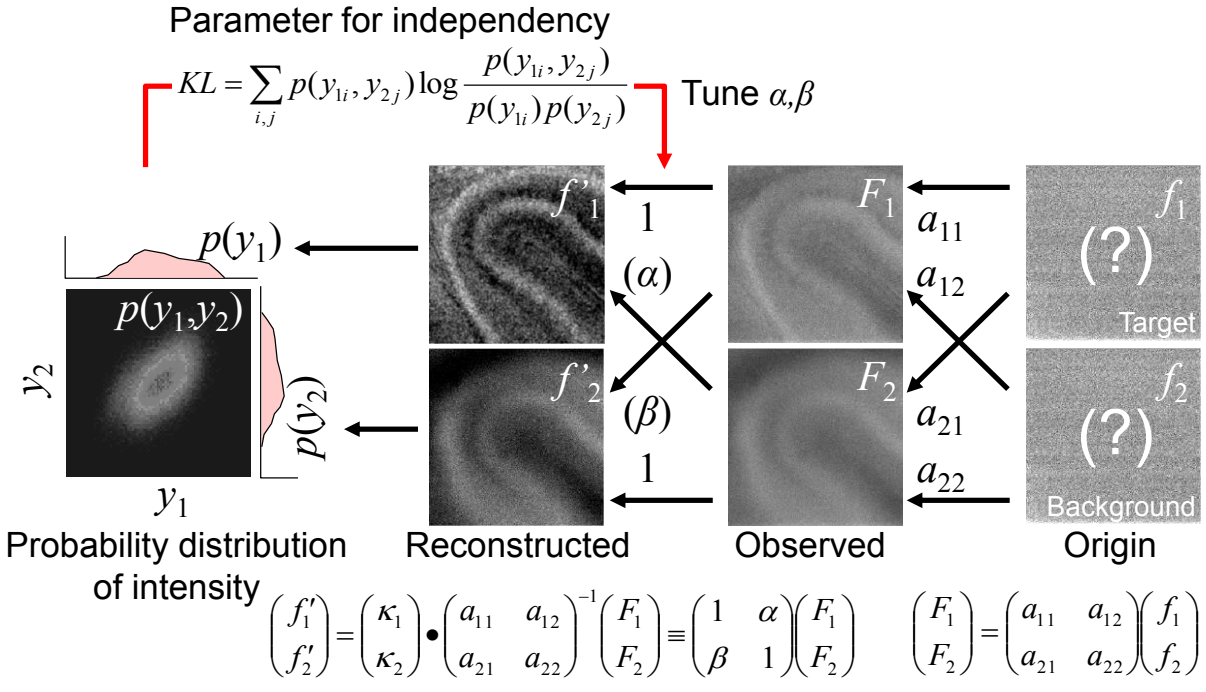

Fig. 5. Illustration for image processing based on independent component analysis

ICA process K-L parameter is calculated in order to evaluate the probabilistic independency of images f'_1 and f'_2. It can be considered that in the reproduction algorithm the core process is the calculation of the K-L parameter. In this preliminary study K-L parameter is successively calculated by manually changing the inverse matrix, and images are assumed to be reproduced when the K-L parameter indicates the minimum.

4. Results and Discussion

4.1 Image Processing using the ICA Figure 6 (a) shows visible light image of the cerebellum with postnatal 21 days. In developing cerebellum, granule cells, small input neurons, proliferate and migrate down from the external granular layer (EGL) to the internal granular layer (IGL). As the development proceeds, EGL turns into molecular layer (ML) whereas IGL remains. Purkinje cells, big output neurons, develop their dendrites and associate neuronal connections between granule cells and other interneurons. Neuronal circuit layer forms the ML. As the cerebellum shown in Fig. 6 (a) is mature, ML, PL, IGL are clearly visible. Note that ML is on the outer side of the cerebellum, and a wrinkle surrounded by the ML is seen in Fig. 6 (a).

As for fluorescence observation, three different images were acquired. Two were with different inclination of the excitation light source, and one was with no excitation light. Each of the two images with excitation light was subtracted with the image with no excitation light, in order to reduce the background light from the outside. These two images after the subtraction were defined as images A and B.

Figure 6 (b) shows these images for a rat cerebellum. Both images are very unclear, because of the background fluorescence. Figure 6 (c) shows the result of image processing. It is clearly shown in the image entitled as "target" that the fluorescence intensity is high in two layers, whereas that entitled as "background" is not clear. By morphological inspection these layers are recognized as ML and IGL. These layers are known that GABAergic neurons distribute in mature cerebellum. Studies using HPLC and electrophysiological method have shown that GABA is released from the postnatal cerebellar cortex even before synaptogenesis, and that GABA receptors act on the developing cerebellar Purkinje cells[4][5]. However, dynamic GABA release could not be observed unless the enzyme-linked photo assay is used. In addition, because cytoplasmic autofluorescence becomes noisy background light, it is useful that the image processing system extracted the image of GABA release from the autofluorescence-contained image. Using this method, both real-time transmitter release and its response to medicine can be observed.

4.2 Transition after Chemical Stimulation In relatively developed cerebellum, cells distributed in the ML and IGL are only the neurons of glutamate release, so that both layers showed fluorescent activities. Figure 7 indicates release distribution of glutamate in comparison with normal optical image illuminated with visible light. The fluorescent image, indicating glutamate release, is after the ICA processing. Figure 7 (c) indicates the regions of interest for analysis. Regions highlighted as ML and IGL have relatively strong intensity in fluorescence. They have a contrast to the region highlighted as PL. Release from white matter (WM), which is mostly composed of fatty materials, is much less significant.

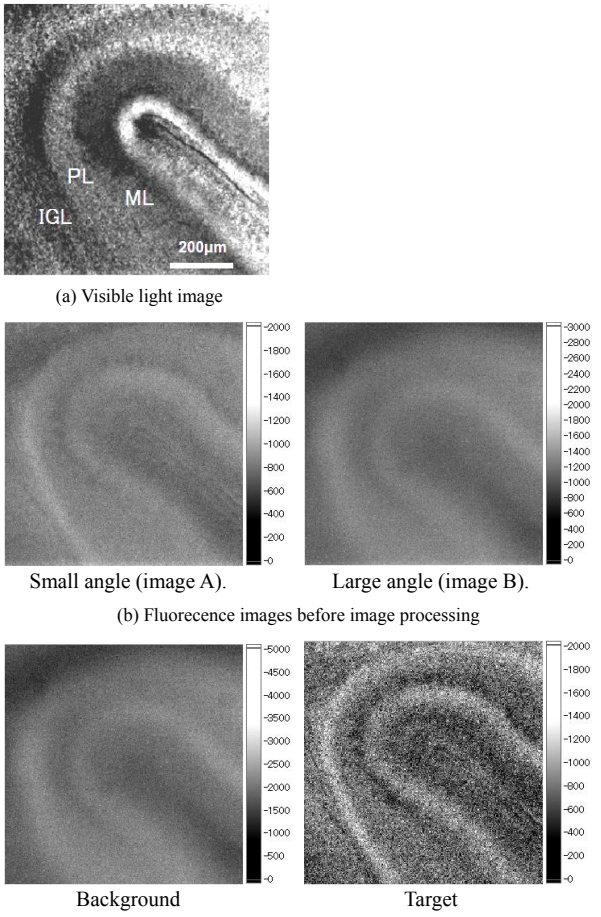

(a) Visible light image

(b) Fluorecence images before image processing

(c) Fluorecence images after image processing

Fig. 6. Cross sectional mages of cerebellar cortex: (a) Visible light image, (b) original fluorescent images with different angle of optical axes, and (c) fluorescent images after the image processing. Scales are indicated in arbitrary unit. Specimen: rat cerebellum (postnatal 21 days), target: GABA

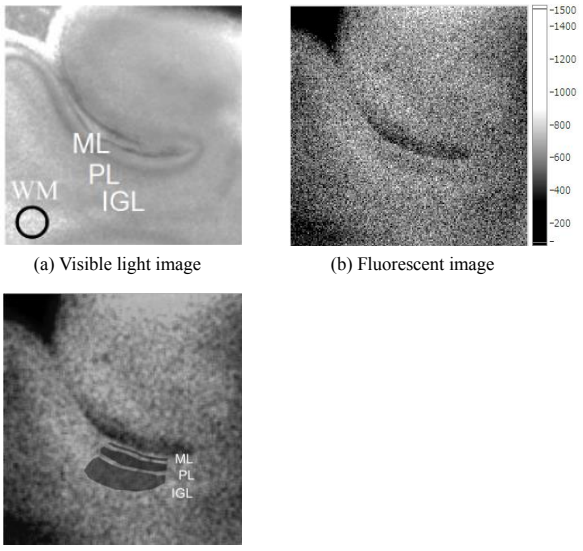

(a) Visible light image

(b) Fluorescent image

(c) Regions of interest for analysis

Fig. 7. Cerebellum with postnatal 7 days observed with visible light and fluorescent light indicating glutamate release. 0.9 mm × 0.9 mm. Gray scale is arbitrary. ML: molecular layer, PL: Purkinje layer, IGL: internal granular layer, WM: white matter. Specimen: rat cerebellum (postnatal 7 days)

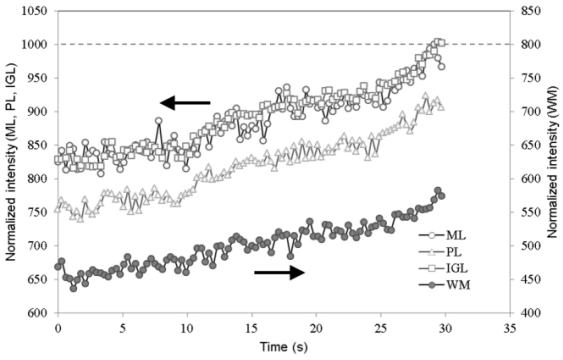

Fig. 8. Transition in fluorescence intensity in each layer (normalized by the intensity of ML 30 s after stimulation that is indicated as 1000). Specimen: rat cerebellum (postnatal 7 days), target: glutaminate

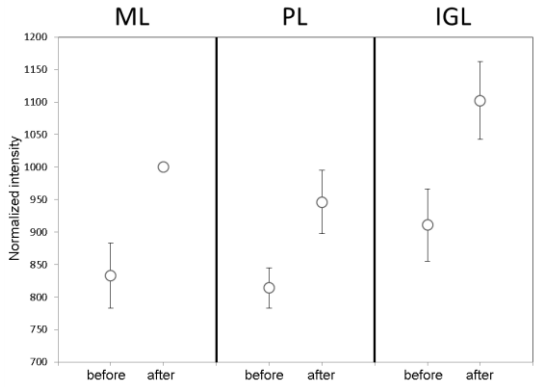

Fig. 9. Change in fluorescence intensity before and after AMPA stimulation (normalized by the intensity of ML 30 s after stimulation that is indicated as 1000). Specimen: rat cerebellum (postnatal 7 days), target: glutaminate

Our system can visualize both spontaneous and responsive transmitter release with about 0.2 s time resolution. Figure 8 shows the transition of glutamate release in response to 100 μmol/ℓ (S)-alpha-Amino-3-hydroxy- 5 methylisoxazole-4-propionic acid (AMPA) application in cerebellar slices. All values are normalized by the intensity of ML 30 s after stimulation that is indicated as 1000. Fluorescence, as indication glutamate release, was intense in both the IGL and ML, whereas the PL was indicated with lower intensity. As shown in Fig. 8, a clear increase in fluorescence was observed after stimulation. Transition in fluorescence was similar for ML and IGL, suggesting that these layers are activated. However PL, which was not expected to release glutamate, showed fluorescence as well although it was less intense than ML and IGL. As this specimen was taken from relatively young rat (postnatal 7 days), the cerebellar development was not totally completed, and the layers were not separated enough. It is hence considered that diffusion from ML and IGL to PL would take place, leading to an increase in fluorescence in this layer. The increase in fluorescence in WM suggests that glutamate might have been diffused into WM as well, although the absolute value was much lower than ML and IGL.

Figure 9 compares the fluorescence in each layer before and after stimulation. Four different specimens were used for the observation, in order to confirm reproducibility. It is clear that the AMPA stimulation brought a significant glutamate release from ML and IGL, although the increase is also seen with PL.

5. Conclusions

A new method for visualization of spatially distributed bioactive molecules using enzyme-linked photo assay has been proposed. It is based on fluorescent reaction assisted by an enzyme immobilized on the substrate, however, background fluorescence disturbs the observation. In order to reduce the background fluorescence, two images were acquired by changing the optical axis of UV illumination. Image processing based on independent component analysis made the target image clear. Observation of rat cerebellum was successfully performed and GABA and glutamate release from two specific layers was clearly indicated.

Acknowledgement

The study was partially supported by grants from Scientific Research (C) 23500516, 26350498 and Health Labor Sciences Research.

References

(1) N. C. Danbolt : "Glutamate Uptake", *Neurobiology*, Vol.65, pp.1-105 (2001)
(2) N. Kasai, Y. Jimbo, O. Niwa, T. Matsue, and K. Torimitsu : "Rea-time Multisite Observation of Glutamate Release in Rat Hippocampal Slices", *Neurosdence Lett.*, Vol.304, pp.112-116 (2001)
(3) T. Morishima, M. Uematsu, T. Furukawa, Y. Yanagawa, A. Fukuda, and S. Yoshida : "GABA Imaging in Brain Slices Using Enzyme-linked Photo Analysis", *Neurosci. Res.*, Vol.67, pp.347-353 (2001)
(4) V. Calhoun, G. Pearlson, and T. Adali : "Independent Component Analysis to fMRI Data, A Generative Model for Validating Results", VLSI Signal Processing, Vol.37, pp.281-291 (2004)
(5) F. F. Trigo, M. Chat, and A. Marty : "Enhancement of GABA Release through Endogenous Activation of Axonal GABA(A) Receptors in Juvenile Cerebellum", *J. Neurosci*., Vol.27, No.46, pp.12452-63 (2007)
(6) K. Obata : "Excitatory and Trophic Action of GABA and Related Substances in Newborn Mice and Organotypic Cerebellar Culture", *Dev Neurosci*, Vol.19, No.1, pp.117-119 (1997)

Hikaru Mabuchi

(Student Member) was born in Hokkaido, Japan on July 25, 1992. He is 1st-year student in Graduate School of Toyohashi University of Technology. His major is electric and electronic information. He has been engaged in research on bio-sensing by means of optical measurement. He is a student member of IEEJ.

HongYao Ong

(Associate) was born in Malaysia on June 30, 1990. He received his B.S degree in 2014 from Toyohashi University of Technology, Japan. His major is electric and electronic information. He is currently engaged in GS Reality Sdn. Bhd., Malaysia. His major is electric and electronic information. He is an associate member of IEEJ.

Kazunori Watanabe

(Non-member) was born in Asahikawa, Japan on February 3, 1992. He is 2nd-year student in Graduate School of Toyohashi University of Technology. His research focuses both the optimization of surface modification for biosensor, and detection of neurotransmitters. He is a member of Japan neuroscience Society.

Sachiko Yoshida

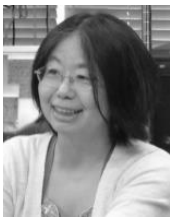

(Non-member) was born in Toyama, Japan on January 24, 1961. She received her B.S., M.S. and Ph.D. degrees in 1983, 1986 and 1990 from University of Tokyo. She was engaged in JSPS Postdoctoral Researcher from 1990 to 1992, JST PRESTO Researcher from 1992 to 1994, and Research Associate at Toyohashi University of Technology from 1995 to 1996. Since 1996, she has been a lecturer of Toyohashi University of Technology. Her research interests focus the physiological interaction and morphological transformation through brain differentiation, and these detections. She is a member of a member of IEEE, International Brain Research Organization, Society for neuroscience, Japan neuroscience Society, and the Physiological Society of Japan.

Naohiro Hozumi

(Senior Member) was born in Kyoto, Japan on April 2, 1957. He received his B.S., M.S. and Ph.D. degrees in 1981, 1983 and 1990 from Waseda University. He was engaged in Central Research Institute of Electric Power Industry (CRIEPI) from 1983 to 1999. He was an associate professor of Toyohashi University of Technology from 1999 to 2006, and a professor of Aichi Institute of Technology from 2006 to 2011. Since 2011, he has been a professor of Toyohashi University of Technology. He has been engaged in the research in insulating materials and diagnosis for high voltage equipment, acoustic measurement for biological and medical applications, etc. He was awarded in 1990 and 1999 from IEE of Japan for his outstanding research papers. He is a member of IEEE, IEE of Japan and the Acoustic Society of Japan.

Quantitative evaluation method for differentiation of C2C12 myoblasts by ultrasonic microscopy

2017 Jpn. J. Appl. Phys. 56 07JF11

(http://iopscience.iop.org/1347-4065/56/7S1/07JF11)

Japanese Journal of Applied Physics **56**, 07JF11 (2017)
https://doi.org/10.7567/JJAP.56.07JF11

REGULAR PAPER

Quantitative evaluation method for differentiation of C2C12 myoblasts by ultrasonic microscopy

Kyoichi Takanashi[1]*, Mamoru Washiya[1], Kazuki Ota[1], Sachiko Yoshida[1], Naohiro Hozumi[1]*, and Kazuto Kobayashi[2]

[1]*Department of Electrical and Electronic Information Engineering, Toyohashi University of Technology, Toyohashi, Aichi 441-8580, Japan*
[2]*Honda Electronics Co., Ltd., Toyohashi, Aichi 441-3139, Japan*

*E-mail: k143239@edu.tut.ac.jp; hozumi@iceed.tut.ac.jp

Received November 25, 2016; accepted February 6, 2017; published online June 14, 2017

Cell differentiation was evaluated by ultrasonic microscopy. However, there were some regions that showed a lower acoustic impedance than the culture liquid. It was considered that, in such regions, the cells were not perfectly in contact with the film substrate. Hence, a waveform analysis was performed, and compensated acoustic impedances in such regions were in a reasonable range of values. By the same analysis, the displacements of partially floated cells were also successfully calculated. The elapsed day transitions of the compensated acoustic impedances and displacements were successfully evaluated. In the process of differentiation, actin fibers comprising the cytoskeleton are supposed to loosen in order to induce cellular fusion. In addition, the progress in cell differentiation accompanied by a change into a three-dimensional structure can partially be assessed by the displacement between a cell and a cultured film. Hence, we believe that cell differentiation can be evaluated using an ultrasonic microscope.

1. Introduction

An optical microscope is often used for the measurement of biological tissues and an antibody staining technique is often employed to observe the biological structure. However, such a measurement process may take a long time because the staining process takes several hours or days. In addition, the biological function of matter may be lost completely after staining.

On the other hand, an ultrasonic microscope makes it possible to indicate an acoustic characteristic (e.g., elastic parameter or sound speed) of cells as a two-dimensional profile.[1–13] An acoustic characteristic is an important parameter for the quantitative characterization of living tissues. As chemical staining is not necessary, the measurement can be performed without losing the biological functions of cells.[14–17] This reduces cost and time for staining as well. In addition, ultrasound can be directly digitized as a waveform three-dimensional structure that may be estimated by various waveform analyses. In this study, we will propose the nondestructive measurement of living cells using an ultrasonic microscope that we developed. C2C12 myoblast cells will be targeted.

As a requirement for cell measurement, regenerative medicine using stem cells is being developed markedly.[18,19] When cells are being transplanted, nondifferentiated cells or tissues should be never included, which may produce teratomas in vivo.[20,21] For such reasons, monitoring cell differentiation is highly advantageous. This series of studies is conducted to determine whether a quantitative ultrasonic microscope can be used to monitor cell differentiation. The transition of the acoustic impedance of the cells during differentiation was monitored. In addition, displacement from the culture film substrate after cell differentiation was evaluated in order to assess cell growth.

2. Experimental methods

2.1 C2C12 myoblasts

The C2C12 myoblasts used in this study are clones of mouse myoblasts. These cells remain undifferentiated at the initial expression of heart and skeletal muscles. The C2C12 myoblasts (DS Pharma Biomedical) were cultured in Minimum Essential Medium Eagle with Hanks' salt (HMEM; Sigma-Aldrich M4780 Hank's MEM) supplemented with l-glutamine, 10% fetal bovine serum (FBS), some vitamins, amino acids, and 0.1 g/L kanamycin (proliferation medium, PM), and the medium was replaced every other day. To induce the differentiation of myoblasts into myotubes, C2C12 cells at an 80–90% confluency were transferred to HMEM without FBS (differentiated medium, DM). All cells were cultured and observed in OptiCell™ (Thermo Scientific Nunc), which is composed of two polystyrene films of 50 cm^2 in culture area and 75 μm in film thickness. C2C12 myoblasts were injected and cultured in the space between the two films.[22]

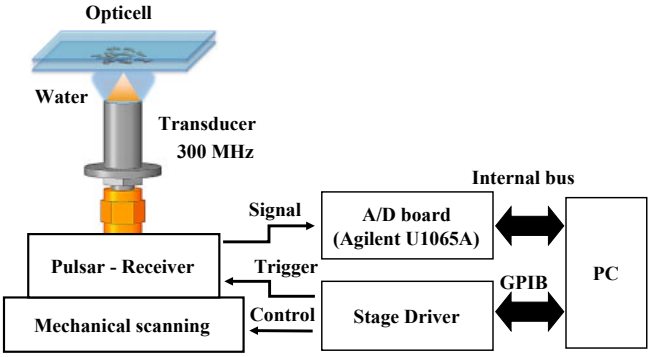

Fig. 1. (Color online) Schematic diagram of the measurement system.

2.2 Measurement system

The details of the measurement system that we developed can be found in Refs. 23–25. As shown in Fig. 1, the scanning ultrasonic microscope is composed of an ultrasonic transducer, a mechanical scanning unit, a pulsar/receiver, an A/D converter (Agilent U1065A Acqiris DC222 8 GS/s), and a stage controller.

The pulsed ultrasound was focused at the interface between a cell and the film substrate. The reflection was received and interpreted into a characteristic acoustic impedance. The two-dimensional acoustic impedance profile was obtained by mechanical scanning.

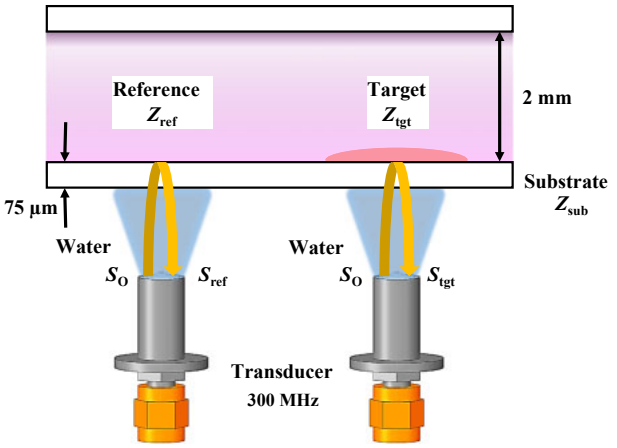

Fig. 2. (Color online) Illustration for calibration of the acoustic impedance.

An acoustic wave was transmitted and received by the same transducer. The ultrasonic transducer was composed of a ZnO thin film attached to a sapphire lens (aperture half-angle: 60°), and its frequency after being driven by an electric pulse ranged briefly from 100 to 500 MHz. The central frequency was 300 MHz. The transducer had a focal length of about 0.288 mm. The measurement was performed with eight times of averaging (sampling frequency was 4 GSamplings/s) in order to reduce random noise before being introduced into the computer. Distilled water was used as the coupling medium between the film substrate and the transducer. Two-dimensional profiles of the acoustic impedance can be obtained by mechanically scanning the transducer.

Figure 2 illustrates the basic concept of determining the acoustic impedance. The reference waveform is the reflection from the interface between the film substrate and the culture liquid, which appears in the field of view, the acoustic impedance of which is known to be 1.52 MN·s/m^3. The target waveform is the reflection from the interface between a cell and the culture liquid.

The acoustic impedance of the target substance, Z_{target}, is determined by comparing these two reflections as

$$Z_{target} = \frac{1 - \frac{S_{target}}{S_{ref}} \cdot \frac{Z_{sub} - Z_{ref}}{Z_{sub} + Z_{ref}}}{1 + \frac{S_{target}}{S_{ref}} \cdot \frac{Z_{sub} - Z_{ref}}{Z_{sub} + Z_{ref}}} Z_{sub}, \quad (1)$$

where S_{ref} and S_{target} are the reference and target signals, and Z_{sub} and Z_{ref} are the acoustic impedances of the film substrate (2.46 MN·s/m^3) and cultured liquid (1.52 MN·s/m^3), respectively. By considering the oblique incident component of the ultrasonic wave, the longitudinal wave acoustic impedance is obtained by using the result of sound field analysis in order to obtain a more accurate value.

2.3 Investigation of low-acoustic-impedance area of the measurement result

Figure 3 shows the acoustic impedance profiles of undifferentiated and differentiated C2C12 myoblasts and their corresponding histograms. In the profiles, the regions measured at around 1.52 MN·s/m^3 correspond to the culture liquid. Cells are normally higher in acoustic impedance than the culture liquid.[7,25–30] However, some regions after differentiation induction are measured at a significantly low acoustic impedance. Hence, some comparisons of waveforms from different points of the measurement result were performed as shown in Fig. 4(a). Firstly, the waveform of the culture liquid, which is defined as the reference waveform, was extracted from point 1. Then, target waveforms from a cell (point 2) and a significantly low acoustic impedance area (point 3) were extracted. Consequently, subtractions between both target waveforms with the reference waveform were performed as shown in Figs. 4(b) and 4(c). From Fig. 4(c), it is clear that the residual waveform obtained from the subtraction of the target waveform from the cell and the reference waveform was relatively larger than that in Fig. 4(b). Here, we can conclude that some interference must have happened in the target waveforms of an area with a significantly low acoustic impedance. Hence,

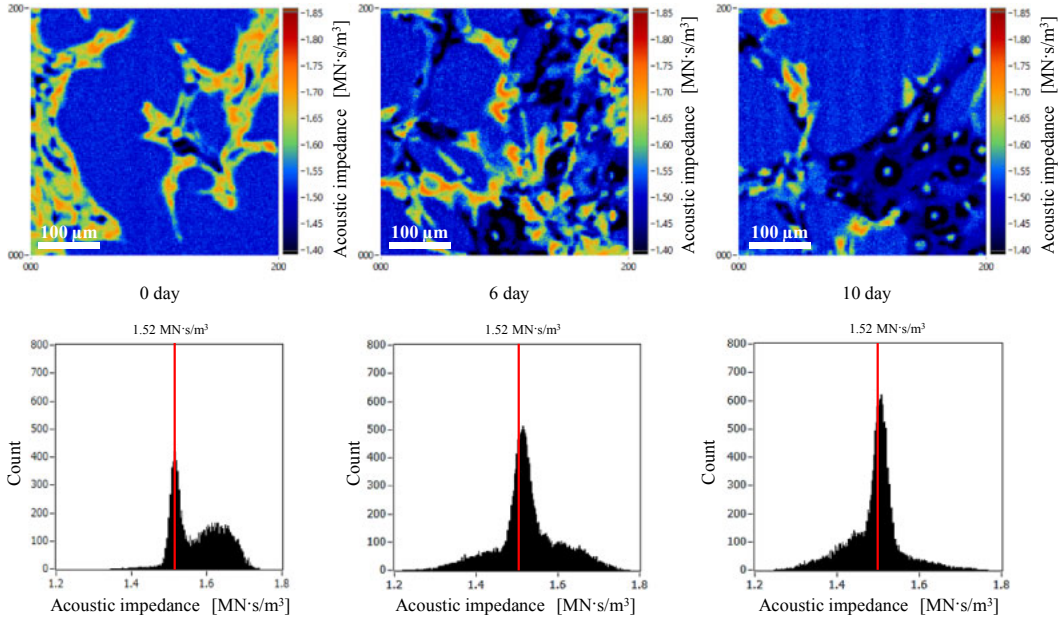

Fig. 3. (Color online) Acoustic impedance profiles of undifferentiated and differentiated C2C12 myoblasts, and their corresponding histograms.

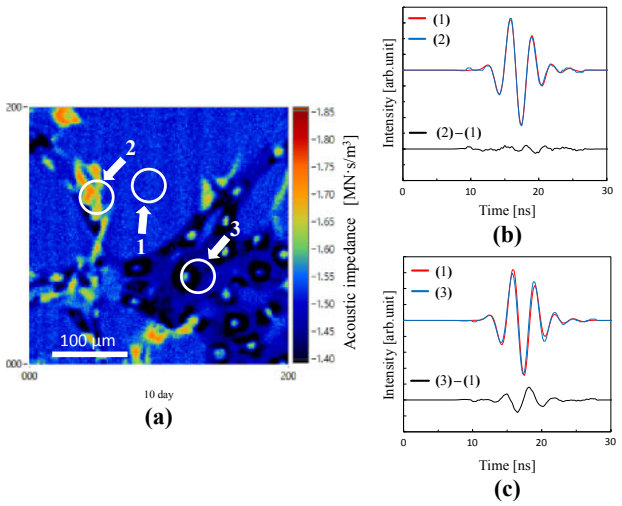

Fig. 4. (Color online) Some comparisons of waveforms from different points. (a) Acoustic impedance profile measured at the 10th day after differentiation induction. (b) Comparison of target waveforms from point 1 and high-acoustic-impedance area (point 2). (c) Comparison of target waveforms from point 1 and significantly low acoustic impedance area (point 3).

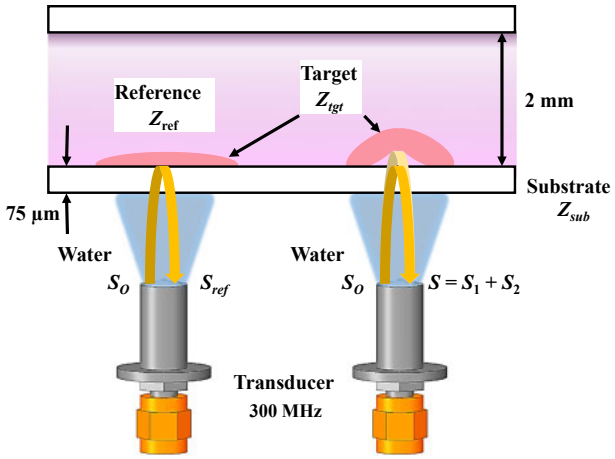

Fig. 5. (Color online) Illustration for compensation of the acoustic impedance.

in order to eliminate interference, the waveform was subjected to the waveform analysis described in the next chapter.

3. Compensation of acoustic impedance

3.1 Interference due to nonperfect contact of cells to the film

C2C12 myoblasts have such a characteristic that F-actin coagulates through differentiation and grows into a tissue with a contractile ability through the expression of various proteins.[26–31] Cell contraction will create a gap between the cell and the film substrate during differentiation. Figure 3 illustrates that, at such a stage, the cells are not perfectly in contact with the film substrate. For this reason, the interference of reflected waves may occur, leading to an error in acoustic impedance estimation. At such a point, it can be assumed that the reflection wave S is composed of two different reflection components (S_1 and S_2).

Figure 5 illustrates the compensation of the acoustic impedance. S_1 is very similar in both shape and intensity to the reference wave S_{ref}, which is the reflection from the interface between the film substrate and the culture liquid. S_2, which can be considered the reflection from the interface between the culture liquid and the cell, is relatively small in intensity, as there is only a small difference in acoustic impedance at the boundary between materials. In addition, these two wave components are opposite in polarity, because the acoustic impedance is high in the culture film, low in the culture liquid, and relatively high again in the cell.

The acquired waves can be separated into these two components by an appropriate waveform analysis. The acoustic impedance of the cell would be evaluated using the separated reflection intensities.

It is assumed that the acquired waveform can be described as a linear combination of the components as

$$S_{(t)} = S_1 + S_2, \tag{2}$$

$$S_{1(t)} = P_1 \exp\left[A_1(t-t_1) - \beta_1(t-t_1)^2\right] \times \cos[2\pi f_0(t-t_1)], \tag{3}$$

$$S_{2(t)} = P_2 \exp\left[A_1(t-t_1) - \beta(t-t_1)^2\right] \times \cos[2\pi f_0(t-t_2)], \tag{4}$$

where P_1 and P_2 are the intensities, A_1 and A_2 are the attenuation constants, f_0 is the central frequency of the pulse ($f_0 = 300\,\mathrm{MHz}$), β_1 and β_2 ($\mathrm{cm}^2/\mathrm{kg}$) are the coefficients of compressibility for the media, and t_1 and t_2 are the delay times. These parameters (P_1, P_2, A_1, A_2, β_1, β_2, t_1, and t_2) can be determined by the gradient descent method. β_1 and β_2 are set as constants with a value of $0.1\,\mathrm{cm}^2/\mathrm{kg}$ to improve the analysis speed. In performing the gradient descent method, a partial derivative is applied to a function, and it searches the local minimum (or maximum) of the function. The reproduced waveform $S_{(t)}$ is modified as

$$\begin{aligned} S_{(t)}^{(k+1)} &= S_{(t)}^{(k)} - \alpha \cdot \mathrm{grad}[f(S_{(t)}^{(k)})] \\ &= S_{(t)}^{(k)} - \alpha \left[\frac{\partial f(S_{(t)}^{(k)})}{\partial P_1^{(k)}} \frac{\partial f(S_{(t)}^{(k)})}{\partial P_2^{(k)}} \frac{\partial f(S_{(t)}^{(k)})}{\partial A_1^{(k)}} \frac{\partial f(S_{(t)}^{(k)})}{\partial A_2^{(k)}} \frac{\partial f(S_{(t)}^{(k)})}{\partial t_1^{(k)}} \frac{\partial f(S_{(t)}^{(k)})}{\partial t_2^{(k)}} \right]^{\mathrm{t}}, \end{aligned} \tag{5}$$

where k is the repetitive number and α is the learning rate. The parameters are determined so that the difference between the waveform reproduced by Eq. (2) and the practically acquired waveform is minimized.

3.2 Compensation of acoustic impedance

The compensation of acoustic impedance was performed by solving

$$S_1 = \frac{Z_{\mathrm{ref}} - Z_{\mathrm{sub}}}{Z_{\mathrm{ref}} + Z_{\mathrm{sub}}} S_0, \tag{6}$$

$$S_2 = \frac{Z_{\mathrm{target}} - Z_{\mathrm{ref}}}{Z_{\mathrm{target}} + Z_{\mathrm{ref}}} TS_0, \tag{7}$$

where S_0 is the transmitted signal, and Z_{sub} and Z_{ref} are the acoustic impedances of the film substrate ($2.46\,\mathrm{MN{\cdot}s/m^3}$)

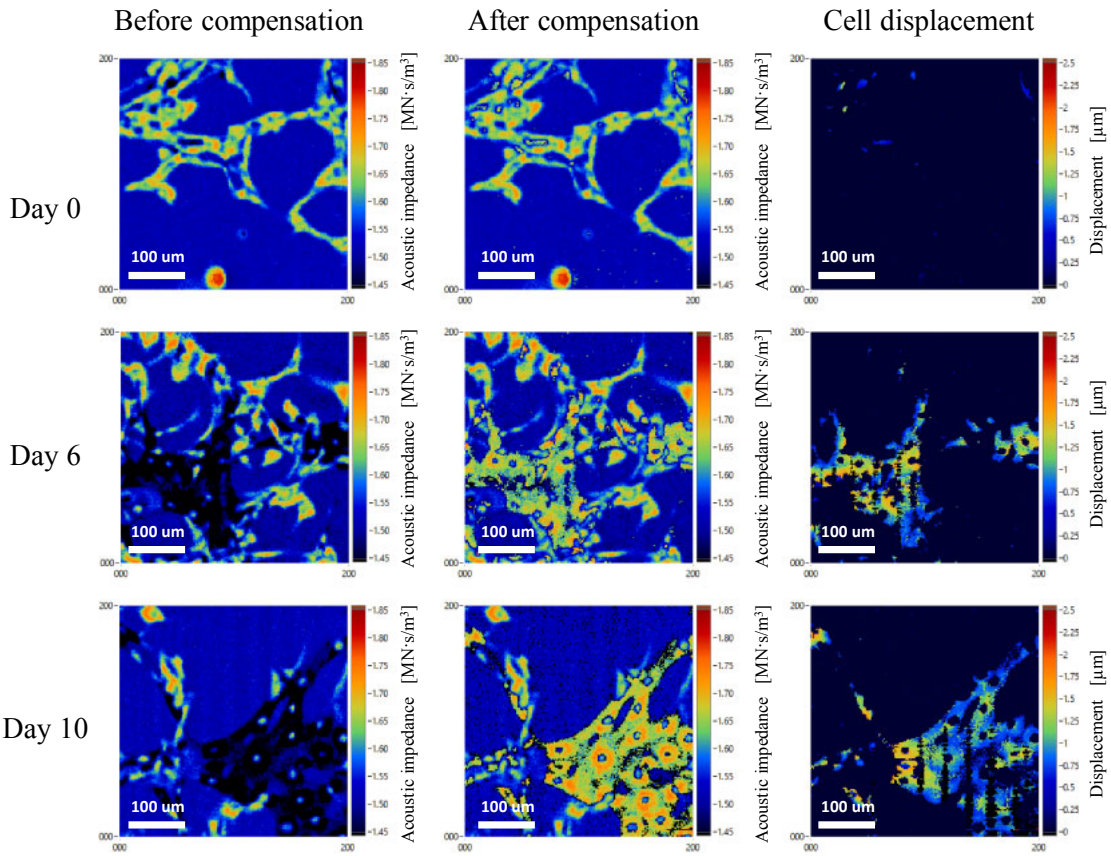

Fig. 6. (Color online) Profiles measured before and after compensation of acoustic impedance and the displacement distance.

and cultured liquid (1.52 MN·s/m^3), respectively. T is the echo transmittance represented as

$$T = \frac{4Z_{\mathrm{sub}}Z_{\mathrm{ref}}}{(Z_{\mathrm{sub}} + Z_{\mathrm{ref}})^2}. \tag{8}$$

By simultaneously solving Eqs. (6)–(8) and considering that S_1 and S_2 are in opposite phases, the cell acoustic impedance Z_{target} at the gap is shown as

$$Z_{\mathrm{target}} = \frac{1 + \frac{S_2}{S_1} \cdot \frac{Z_{\mathrm{sub}}^2 - Z_{\mathrm{ref}}^2}{4Z_{\mathrm{sub}}Z_{\mathrm{ref}}}}{1 - \frac{S_2}{S_1} \cdot \frac{Z_{\mathrm{sub}}^2 - Z_{\mathrm{ref}}^2}{4Z_{\mathrm{sub}}Z_{\mathrm{ref}}}} Z_{\mathrm{ref}}. \tag{9}$$

3.3 Displacement of cells from the culture film

As illustrated in Fig. 5, it is considered that, in the low-acoustic-impedance region in Fig. 3, cells are not perfectly in contact with the film substrate. Therefore, the time lag Δt of the two reflection components was calculated by using t_1 and t_2. The displacement distance d (μm) is shown as

$$d = \frac{1}{2} \cdot c \cdot \Delta t, \tag{10}$$

where c is the sound speed ($c = 1500$ m/s) through the culture liquid and Δt is the time lag of the two reflection components ($\Delta t = t_2 - t_1$).

4. Results and discussion

Figure 6 shows the profiles measured before and after compensation in the low-acoustic-impedance region, and the distance of displacement calculated by using the above-mentioned method. After compensation, the region where the acoustic impedance was originally low showed an acoustic impedance of around 1.65–1.75 MN·s/m^3. This would be a reasonable acoustic impedance of cells.[7,25–30] A significantly high acoustic impedance area appeared around the nucleus. This high-acoustic-impedance area was assumed to be due to F-actin, which protects and supports the nucleus. In addition, the distance of displacement was around 0.8–2.0 μm. Although the spatial resolution in the lateral direction determined by the diffraction limit is expected to be as high as 5 μm at 300 MHz, note that the gap distance of 0.8–2 μm between the cell and the film substrate was successfully assessed, as the spatial resolution in the depth direction is generally much higher than that in the lateral direction at a sufficient sampling speed.

Changes in acoustic impedance accompanied by differentiation were evaluated by the compensated profiling method. Intracellular changes with differentiation in a single cell have been reported; however, the change in differentiating cell population is unknown. Our evaluation first provides the tools to clarify this. Figure 7 shows the transition of the acoustic impedance of cells for 10 days after shifting to DM. This graph represents the ratio of the relatively high acoustic impedance area to the total cellular area in the measurement area. The threshold was changed from 1.55 to 1.70 MN·s/m^3 at an interval of 0.01. When the acoustic impedance was set at 1.68 MN·s/m^3, the transition rate of the area was measured and is as shown in Fig. 7; hence, this value was determined by the threshold value. As shown in this graph, the ratio of the high-acoustic-impedance

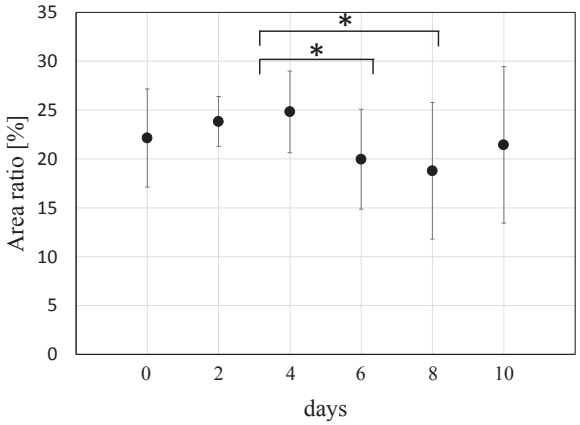

Fig. 7. Area ratio of the high-acoustic-impedance ($\geqq 1.68\,\mathrm{MN{\cdot}s/m^3}$) area to the total cellular area. Each point shows the average area ratio and standard deviation of eight samples ($^*P = 0.07$).

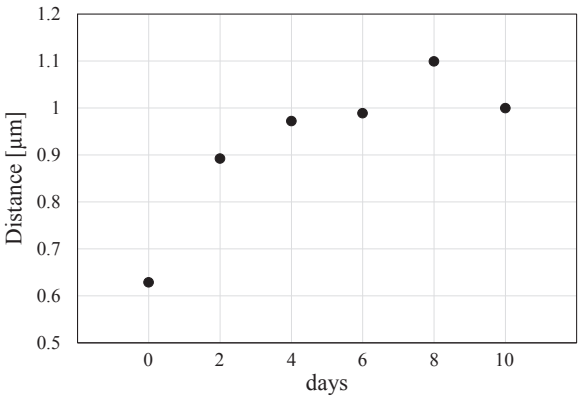

Fig. 8. Elapsed day transition of the average displacement. Each point shows the average displacement of eight samples.

area tended to decrease. The asterisk in the graph shows a tendency to decrease as determined by Student's *t*-test ($P = 0.07$).

This change would be consistent with the change in the intracellular condition of F-actin, which is one of the important factors in cell development. In undifferentiated cells, F-actin exists abundantly in the periphery of the nucleus. During differentiation, myoblast cells simultaneously fuse together to form a myotube. F-actin would defuse within the cytoplasm temporarily. The areal ratio would be reduced after the loosening of F-actin. After cell fusion, F-actin would reassemble in the vicinity of the nucleus and the parenchyma in order to support the cell membranes. Therefore, the ratio of high acoustic impedance would increase as the cells differentiate after the 10th day.

Moreover, Fig. 8 shows the transition of displacement between the cells and the basal film for 10 days after shifting to DM. It tended to increase with a constant rate during differentiation, suggesting the formation of a three-dimensional structure.

However, these measurements were disturbed by the existence of non-negligible noise. For this reason, it is necessary to suppress vibration and reduce noise in order to increase the calculation accuracy of the displacement distance.

5. Conclusions

The differentiation of C2C12 cells was assessed by means of an acoustic microscope. An ultrasonic beam was transmitted across a plastic film substrate on which cells were cultured, and the reflection was interpreted as the acoustic impedance and displacement of cells from the culture film. This quantitative measurement was considered perfectly non-invasive to cells, as well as it made it possible to continuously monitor the change in acoustic response through the differentiation process.

The acoustic impedance was often determined to be extremely low when the reflection intensities from the cell and reference material were simply compared. A waveform analysis made it possible to assess the displacement between a cell and the film substrate, which is also a factor for monitoring the degree of differentiation. In such a case, the acquired waveform was composed of two different reflections. During cell differentiation, the change in the section of impedance was measured, suggesting the loosening of F-actin in the cells. The waveform analysis made it possible to assess the displacement between a cell and the film substrate. The displacement was successfully assessed to be 0.8–2 μm, as the spatial resolution in the depth direction is generally much higher than that in the lateral direction at a sufficient sampling speed. This method would be a good tool for monitoring the degree of differentiation.

The results suggest that monitoring the transition of the acoustic impedance is useful for evaluating the differentiation of muscle fibers. Furthermore, the displacement was found to be reflected by the three-dimensional conformation of the organ.

1) S. Saito, Y. Kameyama, and K. Nakamura, Jpn. J. Appl. Phys. **40**, 3664 (2001).
2) N. Hozumi, R. Yamashita, C.-K. Lee, M. Ngao, K. Kobayashi, Y. Saijo, M. Tanaka, and S. Ohtsuki, Ultrasonics **42**, 717 (2004).
3) Y. Saijo, N. Hozumi, C. Lee, M. Nagao, K. Kobayashi, N. Oakada, N. Tanaka, E. S. Filho, H. Sasaki, M. Tanaka, and T. Yambe, Ultrasonics **44**, e51 (2006).
4) N. Hozumi, A. I. Gunawan, S. Kajima, S. Yoshida, Y. Saijo, K. Kobayashi, and S. Yamamoto, 2013 Joint UFFC/EFTF/PFM Symp., 2013, p. 1212.
5) K. Kobayashi, S. Yoshida, Y. Saijo, and N. Hozumi, Ultrasonics **54**, 1922 (2014).
6) N. Hozumi, R. Yamashita, C.-K. Lee, M. Nagao, K. Kobayashi, Y. Saijo, M. Tanaka, N. Tanaka, and S. Ohtsuki, Acoust. Sci. Technol. **24**, 386 (2003).
7) Y. Saijo, T. Miyakawa, H. Sasaki, M. Tanaka, and S. Nitta, Ultrasonics **42**, 695 (2004).
8) T. Higuchi, S. Hirata, T. Yamaguchi, and H. Hachiya, Jpn. J. Appl. Phys. **52**, 07HF19 (2013).
9) T. Higuchi, S. Hirata, T. Yamaguchi, and H. Hachiya, Jpn. J. Appl. Phys. **53**, 07KF27 (2014).
10) K. Tachi, H. Hasegawa, and H. Kanai, Jpn. J. Appl. Phys. **53**, 07KF17 (2014).
11) H. Isono, S. Hirata, and H. Hachiya, Jpn. J. Appl. Phys. **54**, 07HF15 (2015).
12) Z. Qu and Y. Ono, Jpn. J. Appl. Phys. **54**, 07HF01 (2015).
13) M. Omura, K. Yoshida, M. Kohta, T. Kudo, T. Ishiguro, K. Kobayashi, N. Hozumi, and T. Yamaguchi, Jpn. J. Appl. Phys. **55**, 07KF14 (2016).
14) Y. Saijo, E. S. Filho, H. Sasaki, T. Yambe, M. Tanaka, and N. Hozumi, IEEE Trans. Ultrason. Ferroelectr. Freq. Control **54**, 1571 (2007).
15) Y. Saijo, A. Kimura, S. Terauchi, M. Nagao, S. Yoshida, K. Kobayashi, and N. Hozumi, IEEE Ultrasonics Symp., 2006, p. 1421.
16) Y. Hagiwara, Y. Saijo, A. Ando, E. Chimoto, H. Suda, Y. Onoda, and E. Itoi, Ultrasonics **49**, 386 (2009).
17) Y. Tanaka, Y. Saijo, Y. Fujihara, H. Yamaoka, S. Nishizawa, S. Nagata, T.

Ogasawara, Y. Asawa, T. Takato, and K. Hoshi, J. Biosci. Bioeng. **113**, 252 (2012).
18) O. Ishii, M. Shin, T. Sueda, and J. P. Vacanti, J. Thorac. Cardiovasc. Surg. **130**, 1358 (2005).
19) Y. Kuroyanagi, K. Kubo, H. Matsui, H. J. Kim, S. Numari, Y. Mabuchi, and S. Kagawa, Artif. Organs **28**, 13 (2004).
20) M. Abad, L. Mosteiro, C. Pantoja, M. Cañamero, T. Rayon, I. Ors, O. Graña, D. Megias, O. Domindues, D. Martinez, M. Manzanares, S. Ortega, and M. Serrano, Nature **502**, 340 (2013).
21) W. Y. Wendy, P. E. de Almeida, and J. C. Wu, *Teratoma Formation: A Tool for Monitoring Pluripote ncy in Stem Cell Research* (Stembook, Boston, MA, 2012) p. 1.
22) S. T. Cooper, A. L. Maxwell, E. Kizana, M. Ghoddusi, E. C. Hardeman, I. E. Alexander, D. G. Allen, and K. N. North, Cell Motility Cytoskeleton **58**, 200 (2004).
23) N. Hozumi, A. Kimura, S. Terauchi, M. Nagao, S. Yoshida, K. Kobayashi, and Y. Saijo, IEEE Ultrasonics Symp., 2005, p. 170.
24) A. I. Gunawan, N. Hozumi, S. Yoshida, Y. Saijo, K. Kobayashi, and S. Yamamoto, Ultrasonics **61**, 79 (2015).
25) A. I. Gunawan, N. Hozumi, K. Takahashi, S. Yoshida, Y. Saijo, K. Kobayashi, and S. Yamamoto, Ultrasonics **63**, 102 (2015).
26) J. A. Hildebrand, D. Rugar, R. N. Johnston, and C. F. Quate, Proc. Natl. Acad. Sci. U.S.A. **78**, 1656 (1981).
27) S. Y. Chou, C. M. Cheng, and P. R. LeDuc, Biomaterials **30**, 3136 (2009).
28) H. Haga, S. Sasaki, K. Kawabata, E. Ito, T. Ushiki, and T. Sambongi, Ultramicroscopy **82**, 253 (2000).
29) S. Kidoaki, T. Matsuda, and K. Yoshikawa, Biomech. Model. Mechanobiol. **5**, 263 (2006).
30) S. Kidoaki and T. Matsuda, J. Biomed. Mater. Res., Part A **81A**, 803 (2007).
31) S. Burattini, P. Ferri, M. Battistelli, R. Curci, F. Luchetti, and E. Falcieri, Eur. J. Histochem. **48**, 223 (2004).

Effects of anticancer drugs on glia–glioma brain tumor model characterized by acoustic impedance microscopy

2017 Jpn. J. Appl. Phys. 56 07JF15

(http://iopscience.iop.org/1347-4065/56/7S1/07JF15)

Japanese Journal of Applied Physics **56**, 07JF15 (2017)
https://doi.org/10.7567/JJAP.56.07JF15

REGULAR PAPER

Effects of anticancer drugs on glia–glioma brain tumor model characterized by acoustic impedance microscopy

Thomas Tiong Kwong Soon[1], Tan Wei Chean[2], Hikari Yamada[1], Kenta Takahashi[2], Naohiro Hozumi[2], Kazuto Kobayashi[3], and Sachiko Yoshida[1*]

[1]*Department of Environmental and Life Sciences, Toyohashi University of Technology, Toyohashi, Aichi 441-8580, Japan*
[2]*Department of Electrical and Electronic Information Engineering, Toyohashi University of Technology, Toyohashi, Aichi 441-8580, Japan*
[3]*Honda Electronics Co., Ltd., Toyohashi, Aichi 441-3147, Japan*

*E-mail: syoshida@ens.tut.ac.jp

Received November 25, 2016; accepted February 6, 2017; published online June 15, 2017

An ultrasonic microscope is a useful tool for observing living tissue without chemical fixation or histochemical processing. Two-dimensional (2D) acoustic impedance microscopy developed in our previous study for living cell observation was employed to visualize intracellular changes. We proposed a brain tumor model by cocultivating rat glial cells and C6 gliomas to quantitatively analyze the effects of two types of anticancer drugs, cytochalasin B (CyB) and temozolomide (TMZ), when they were applied. We reported that CyB treatment (25 μg/ml, $T = 90$ min) significantly reduced the acoustic impedance of gliomas and has little effect on glial cells. Meanwhile, TMZ treatment (2 mg/ml, $T = 90$ min) impacted both cells equally, in which both cells' acoustic impedances were decreased. As CyB targets the actin filament polymerization of the cells, we have concluded that the decrease in acoustic impedance was in fact due to actin filament depolymerization and the data can be quantitatively assessed for future studies in novel drug development.

1. Introduction

Gliomas are the most common and serious type of brain cancer and arise from glial cells, which are the supportive cells for neurons, and their incidence is increasing over time.[1)] It is an umbrella term for various glial tumors: astrocytoma, oligodendroglioma, ependymoma, and glioblastoma.[2)] They are characterized by highly proliferative growth and malignancy, which make up approximately 30% of all brain and central nervous system tumors and 80% of all malignant brain tumors.[3)] Therefore, combined therapy is vital, for instance, treating patients with a combination of surgery, chemotherapy, radiotherapy, and immunotherapy, as this may prolong patients' survival while reducing morbidity. Despite intensive research, the prognosis for glioma patients remains poor.[1,4,5)] Although many novel anticancer drugs are constantly sought, most of them have proven to be toxic to even normal cells or organs. Thus, it is essential to determine the effect of each drug on cell viability.

Two common anticancer drugs, cytochalasin B (CyB) and temozolomide (TMZ), were used in this study to quantitatively investigate their effects on the constructed brain tumor model. CyB is a type of cell-permeable alkaloid mycotoxin, which can be extracted from the fungus *Helminthosporium dematioideum*.[6)] It targets actin filaments, a major component of the cytoskeleton that controls cell mobility and morphology, by inhibiting network formation in actin polymerization. This causes the cytoskeleton to depolymerize, and hence reduce the cell membrane integrity.[7,8)] Meanwhile, TMZ is an imidazotetrazine derivative that is also a novel oral alkylation agent commonly used in brain cancer treatment for glioblastoma multiforme and astrocytoma.[9)] It damages the DNA of cancer cells by alkylating guanine bases of cancer cell DNA because cancer cells proliferate faster than normal cells, which make them more sensitive to DNA damage. It is a modestly effective anticancer drug that also displays significant toxicity.[10,11)] Moreover, zinc (Zn) was used in this study to help us distinguish between normal cells and cancer cells. It is critical for cell growth, development, and differentiation.[12)] Moreover, it is required for DNA synthesis, RNA transcription, cell division, and tissue repair and growth.[13)] Many reports have suggested that Zn is involved in cancer development, and it has been widely recognized that the leucine zipper is upregulated in most cancers.[14)] Increased concentration of Zn in most tumors indicates that Zn accumulation occurs in cancer cells.[15–17)] Hence, we employed Zn as a cancer-cell-accumulating metal in this study to identify cancer cells.

Nonclinical studies that investigate the effects of anticancer drugs using cultured cells play an important role in new drug development. Optical microscopy is often used to determine the effects of drugs in these types of experiment by evaluating morphological changes of the cells. For that reason, it can only distinguish between living cells and dead or damaged cells. Therefore, we propose an ultrasonic microscope for cell observation that targets cell morphology based on their elasticity, as it is reported that the elasticity is different between healthy cells and cancer cells.[18)] It is a powerful tool for the live observation of intracellular conditions.[19)] We have observed nuclear and cytoskeletal distributions of rat cerebellar tissue, glia cells, glioma cells, and C2C12 cells, and their dynamical changes in cultured living cells. It has been employed in the observation of living tissue, which works quickly and nondestructively without chemical staining.[20–30)] In this study, two-dimensional (2D) acoustic impedance microscopy that was developed in our previous study was employed to aid us in the quantitative observation of the brain tumor model, before and after the anticancer drug injection. The acoustic impedance images obtained through this observation visualize the intracellular conditions of the brain tumor model under treatment with anticancer drugs. Therefore, the observation can be made quickly without damaging cells as it does not require staining. These features enable the development of a novel evaluation system for drug screening.

2. Experimental methods

2.1 Cell culture

Glial cells were extracted from a model animal VGAT-Venus rat cerebellum P0–P2 (P = postnatal), whereas C6 glioma

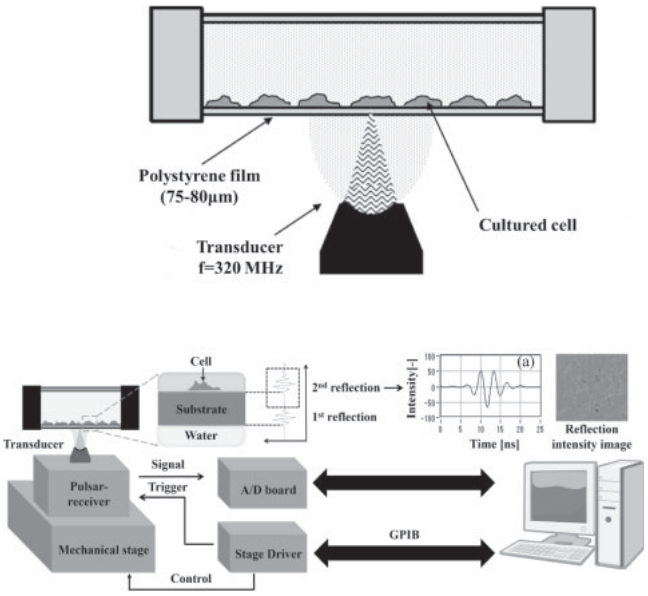

Fig. 1. Schematic diagram of measurement system. Typical acoustic waveform reflected from target (a).

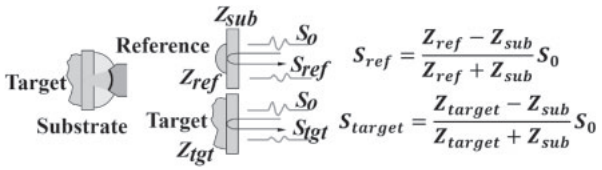

Fig. 2. Basic concept for calibration of acoustic impedance assuming perpendicular incidence.

cells[31] were obtained commercially (DS Pharma Biomedical). The extracted glial cells were genetically labeled with the endogenous fluorescent protein Venus[32] to visualize their position in a culture vessel. Cell cultivation was carried out in a commercial culture vessel, OptiCell™ (Thermo Scientific Nunc). It was composed of two polystyrene films in which each film has a thickness of 75 μm and the gap between the two films was 2 mm. All cells were proliferated in Minimum Essential Medium Eagle with Hanks' salt (HMEM) supplemented with 4 g/L D-glucose, 10% calf serum, and 0.1 g/L kanamycin, and the medium was replaced every other day.

2.2 Brain tumor model

A glia–glioma brain tumor model was constructed by cocultivating both glial cells and gliomas in the same culture vessel to quantitatively analyze the effects of anticancer drugs when they were applied to the brain tumor model.[33]

2.3 Anticancer drugs

Two types of anticancer drugs commonly used in cancer treatment, CyB (25 μg/ml) and TMZ (2 mg/ml), were used in this research to investigate their effects on the constructed glia–glioma brain tumor model. Additionally, zinc sulphate ($ZnSO_4$, 400 μM) was applied as a cancer-cell-accumulating metal that helps us to distinguish between normal cells and cancer cells.

2.4 Acoustic impedance microscopy

Figure 1 illustrates the schematic diagram of the observation system employed in this research, which was established in our previous study. The transducer consists of a flat ZnO as piezoelectric material attached with a sapphire lens of (assumed uniform) half curvature of 60°. Its aperture diameter and focal length (from the bottom of the lens) were 0.43 and 0.29 mm, respectively.[20–24] The central frequency of the transducer was designed as 320 MHz. Acoustic pulse wave spreading (200–400 MHz) was focused on the interface between the cell and the substrate, and sent through the substrate. The acoustic wave transmitted and received by the same transducer was focused on the interface between the substrate and the specimen. OptiCell™ containing cultured cells was placed above the transducer, which mechanically scanned the specimen by attaching it to a stage driver while maintaining the focal point on the rear surface of the film. The reflection from the surface was subsequently interpreted into a 2D profile of reflection intensity. All the measurements were performed at room temperature. Figure 2 shows the basic concept of calibration, in which the signal reflected from the target is compared with that reflected from the reference material. If the incident angle was approximated to be perpendicular to the substrate, the target signal compared with the reference signal can be interpreted into acoustic impedance as

$$T_{\mathrm{tgt}} = \frac{1 + \frac{S_{\mathrm{tgt}}}{S_0}}{1 - \frac{S_{\mathrm{tgt}}}{S_0}} \cdot Z_{\mathrm{sub}} = \frac{1 - \frac{S_{\mathrm{tgt}}}{S_{\mathrm{ref}}} \cdot \frac{Z_{\mathrm{sub}} - Z_{\mathrm{ref}}}{Z_{\mathrm{sub}} + Z_{\mathrm{ref}}}}{1 + \frac{S_{\mathrm{tgt}}}{S_{\mathrm{ref}}} \cdot \frac{Z_{\mathrm{sub}} - Z_{\mathrm{ref}}}{Z_{\mathrm{sub}} + Z_{\mathrm{ref}}}} \cdot Z_{\mathrm{sub}}, \qquad (1)$$

where S_0 is the transmitted signal, S_{tgt} and S_{ref} are reflections from the target and reference, and Z_{tgt}, Z_{ref}, and Z_{sub} are the acoustic impedances of the target, reference, and substrate, respectively. As for the substrate, polystyrene film ($Z_{\mathrm{sub}} = 2.46\,\mathrm{N\,s\,m^{-3}}$) was chosen, and for the reference material, culture medium ($Z_{\mathrm{ref}} = 1.52\,\mathrm{N\,s\,m^{-3}}$) was employed. This equation was practically corrected by considering the focused sound field.[20]

In this research, we measured a coculture system with glial cells and C6 glioma cells. $ZnSO_4$ and the anticancer drugs CyB and TMZ were injected into the OptiCell™ after the setup for experiment. The treatment time for glial cells and gliomas was 120 min each and 90 min for cocultured cells.

2.5 Statistical analysis

Each experiment was repeated 3 times for each drug. More than 10 pieces of both glial cells and glioma cells in each OptiCell™ treated with each drug were subjected to observation and analysis using the acoustic impedance profile. Data are reported as means ± standard deviation. All experimental procedures were approved by the committees for the use of animals in Toyohashi University of Technology and the Prime Minister's Office in Japan.

3. Results and discussion

Acoustic observation using high-frequency ultrasound is almost noninvasive because it does not change the cellular impedance even in continuous irradiation for 90 min. The mean values for the acoustic impedance of both cells were approximately $1.61\,\mathrm{N\,s\,m^{-3}}$. Treatment with 25 μg/ml CyB decreased the intracellular acoustic impedance of both glial cells and glioma cells for 120 min (Fig. 3). This suggests that long-lasting CyB treatment would cause damage to both types of cells. In contrast, 90 min of CyB treatment to glia–glioma coculture showed that the impedance of glioma cells was more decreased than that of glial cells (Fig. 4). Moreover, the impedance change of both cells was

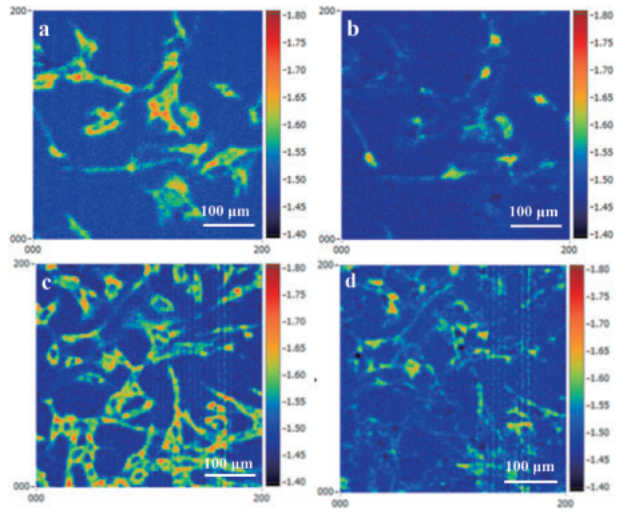

Fig. 3. (Color) Acoustic impedance changes with CyB treatment (25 mg/ml). (a) and (b), glial cells, and (c) and (d), glioma cells. (a) and (c) show untreated cells, and (b) and (d) show cells treated with CyB for 120 min.

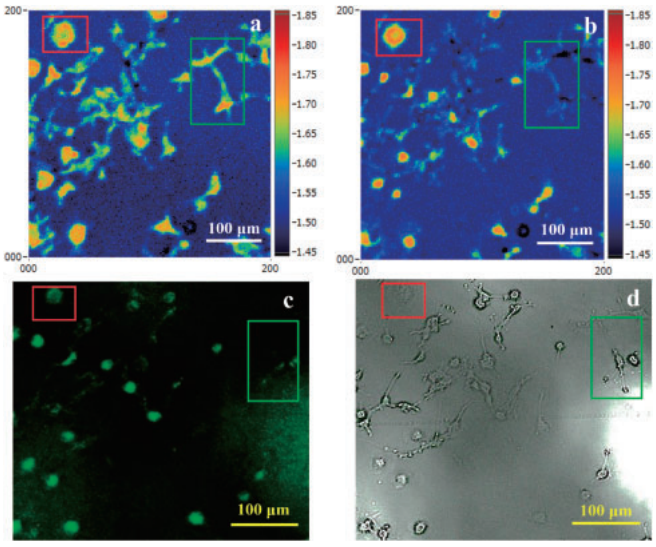

Fig. 4. (Color) Acoustic impedance changes with CyB treatment in glia–glioma coculture. The red square shows a typical glial cell, and the green square shows glioma cells. (a) Untreated coculture, and (b) coculture treated with CyB for 90 min. (c) Venus fluorescent image, and (d) phase contrast light microscopy image.

normalized and shown in Fig. 5. The impedance of glioma cells was decreased by about 1.5%, while normal glial cells showed little change. We also used confocal microscopy to confirm the position of glial cells inside the culture vessel as they were labeled by endogenous fluorescence. Green fluorescence proteins were observed when the specimen is excited by laser light. In addition, the glioma cells with decreased impedance did not disappear or die. Almost all the cells were present even after 90 min of CyB treatment. However, the cytoskeletal structures of the glioma cells were damaged. On the other hand, 2 mg/ml TMZ treatment for 90 min slightly decreased the acoustic impedance of both cells (Fig. 6). The impedance of glioma was decreased by about 1.0%, whereas that of normal glia was decreased by about 0.5%. TMZ is reported as the most sufficient antitumor drug and administrated clinically, while it is not harmless to

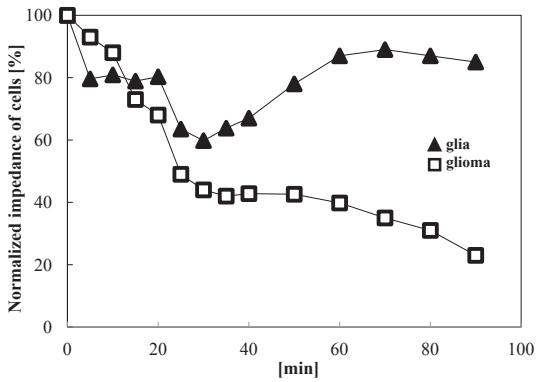

Fig. 5. Normalized impedance changes with CyB treatment in glia–glioma coculture.

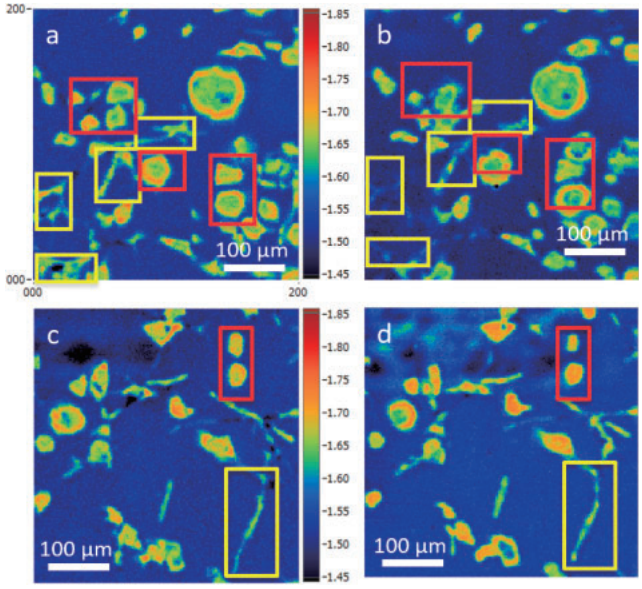

Fig. 6. (Color) Acoustic impedance changes with Zn treatment and TMZ treatment (2 mg/ml) in glia–glioma coculture. The red square shows a typical glial cell, and the yellow square shows glioma cells. (a) and (c), untreated coculture, and (b) and (d), coculture treated with TMZ for 90 min.

normal cells. Summarized data of the impedance changes following anticancer treatments are shown in Fig. 7.

Acoustic impedance microscopy (AIM) developed from our previous studies was employed in this study by interpreting the reflection intensity into 2D acoustic impedance. This system is suitable for the observation of biological soft tissue (rat cerebellar tissue) and cells (rat-derived glial cells, glioma cells, C2C12 cells) as the internal structure of cells, mainly the cytoskeleton, can be clearly observed and indicated considerably by high acoustic impedance. This enables us to elucidate the drug mechanism within the cells, which provides us with new insights for drug screening.[19–30] Thus, the effects of Zn and the anticancer drugs CyB and TMZ on the aforementioned brain tumor model were quantitatively analyzed to help us develop a new observation system for drug screening.

Long-lasting CyB treatment ($T = 120$ min) causes cytotoxicity to even normal cells. Glioma cells proliferate faster than glial cells, and hence are more affected by CyB treatment that promotes actin filament depolymerization by binding to F-actin. Recent studies showed that the cytoskeleton partic-

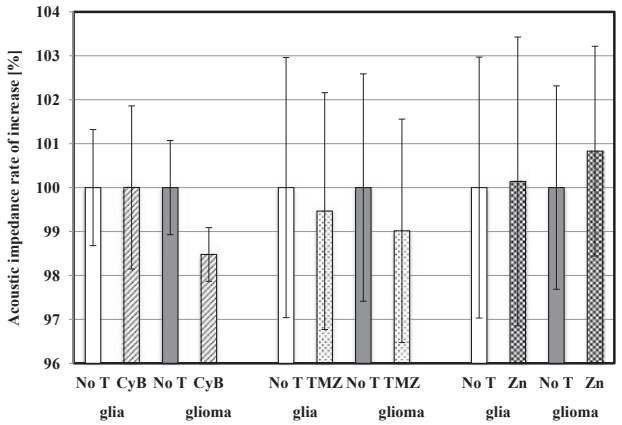

Fig. 7. Acoustic impedance changes with Zn treatment and anticancer drug treatment. No T, no treatment; Zn, Zn treatment; CyB, 90 min CyB treatment; TMZ, 90 min TMZ treatment. All data were normalized with the impedance of untreated samples.

ipates in various vital cellular activities, such as gene expression, cell movement, division and proliferation, and the transition to cancer. Therefore, rapidly dividing glioma cells undergo rapid F-actin polymerization. Once CyB binds to F-actin, it inhibits the superposition of G-actin, and hence depolymerization occurs, which decreases the integrity of the cytoskeleton.[7,34–40] However, when we treated glial cells with CyB long enough, the cytotoxicity of CyB towards glial cells was observed as the impedance of the glial cells decreased. This is because when normal cells treated with CyB proliferate, they are also affected by its inhibitory effect. The damaged cells can be observed in the 2D acoustic impedance image with lower impedance. When we shortened the treatment time to 90 min in the glia–glioma coculture, CyB showed little to no effect toward normal glial cells as the impedance did not change much after treatment. This suggests that AIM can be used as a monitoring system that can observe intracellular changes in living cells in real time.

In the glia–glioma coculture, both CyB and TMZ showed inhibitory effects on glioma cells because they decreased intracellular impedance. However, TMZ also affected normal glial cells, as it interferes with DNA replication by alkylation. It mainly targets cells with a high proliferation rate, such as cancer cells and normal cells that proliferate frequently, such as bone marrow and gastrointestinal tract cells.[9–11,41–43] In this case, glial cells were extracted from a model animal on P0–P2, which have a high proliferation rate, and hence were sensitive to TMZ treatment. We chose TMZ because we wanted to observe changes around nuclei, which house chromosomes, by AIM. Nevertheless, the acoustic impedance image only showed shrunken cells, suggesting that both cells were damaged. No significant changes around the nucleus were observed, as we anticipated.

On the other hand, Zn treatment showed a prominent result. Zn is an essential trace element, which is critical for nucleic acid replication and cell proliferation and is involved in cancer development.[12–14,44] Many research studies have shown that the concentration of Zn in tumors increased, indicating Zn accumulation in cancer cells.[15–17] We confirmed the accumulation of Zn in both cells as the impedance increased, especially around the cell nucleus. This suggests that the accumulation of Zn enhanced the reflection signal, which increased the acoustic impedance. Moreover, this suggests that AIM can be used for intracellular dynamics observation by carefully choosing the right indicator, such as Zn in this case instead of TMZ.

4. Conclusions

This study shows that acoustic impedance microscopy helps us to reveal the intracellular changes in living cells upon drug application without invasion. This is unprecedented in any other observation tools that are commonly used in potential anticancer drug development and cancer treatment, which require biopsy, cell staining, immunochemistry, and many other procedures. We are very optimistic that this study will provide us a simpler approach in potential anticancer drug screening before clinical trial. Potential anticancer drug candidates are usually tested on a huge number of animals before they are used in clinical trials. However, our result suggests that acoustic impedance microscopy would be more useful to decrease the necessity of conducting animal experiments. Furthermore, the visualization of the intracellular changes may aid us in elucidating both the mechanism of anticancer drugs and the physiological behavior of cancer cells. Consequently, acoustic impedance microscopy would help us to improve the current anticancer drug development.

Acknowledgment

This work was supported by JSPS KAKENHI Grant Numbers JP15H04017 and JP24360160.

1) S. M. Chang, I. F. Parney, W. Huang, F. A. Anderson, A. L. Asher, M. Bernstein, K. O. Lillehei, H. Brem, M. S. Berger, E. R. Laws, and Glioma Outcomes Project Investigators, JAMA **293**, 557 (2005).
2) D. N. Louis, A. Perry, G. Reifenberger, A. von Deimling, D. Figarella-Branger, W. K. Cavenee, H. Ohgaki, O. D. Wiestler, P. Kleihues, and D. W. Ellison, Acta Neuropathol. **131**, 803 (2016).
3) M. L. Goodenberger and R. B. Jenkins, Cancer Gen. **205**, 613 (2012).
4) E. R. Laws, I. F. Parney, W. Huang, F. Anderson, A. M. Morris, A. Asher, K. O. Lillehei, M. Bernstein, H. Brem, A. Sloan, and M. S. Berger, J. Neurosurg. **99**, 467 (2003).
5) K. R. Lamborn, S. M. Chang, and D. P. Michael, Neuro-Oncology **6**, 227 (2004).
6) D. C. Aldridge, J. J. Armstrong, R. N. Speake, and W. B. Turner, J. Chem. Soc. C, 1667 (1967).
7) S. F. Pedersen, E. K. Hoffmann, and J. W. Mills, Comput. Biochem. Physiol. A **130**, 385 (2001).
8) D. Cimini, D. Fioravanti, C. Tanzarella, and F. Degrassi, Chromosoma **107**, 479 (1998).
9) A. I. Omar and W. P. Mason, Core Evidence **4**, 93 (2009).
10) A. Carmo, H. Carvalheiro, I. Crespo, I. Nunes, and M. C. Lopes, Oncol. Lett. **2**, 1165 (2011).
11) W. J. Kil, D. Cerna, W. E. Burgan, K. Beam, D. Carter, P. S. Steeg, P. J. Tofilon, and K. Camphausen, Clin. Cancer Res. **14**, 931 (2008).
12) A. S. Prasad, Nutrition **11** [Suppl], 93 (1994).
13) A. S. Prasad, J. Trace Elem. Exp. Med. **11**, 63 (1998).
14) E. John, T. C. Laskow, W. J. Buchser, B. R. Pitt, P. H. Basse, L. H. Butterfield, P. Kalinski, and M. T. Lotze, J. Transl. Med. **8**, 118 (2010).
15) I. L. Mulay, R. Roy, B. E. Knox, N. H. Suhr, and W. E. Delaney, J. Natl. Cancer Inst. **47**, 1 (1971).
16) M. K. Schwartz, Cancer Res. **35**, 3481 (1975).
17) M. Murakami and H. Toshio, Cancer Sci. **99**, 1515 (2008).
18) X. Tang, T. B. Kuhlenschmidt, J. Zhou, P. Bell, F. Wang, M. S. Kuhlenschmidt, and T. A. Saif, Biophys. J. **99**, 2460 (2010).
19) K. Kobayashi, S. Yoshida, Y. Saijo, and N. Hozumi, Ultrasonics **54**, 1922 (2014).
20) A. I. Gunawan, N. Hozumi, S. Yoshida, Y. Saijo, K. Kobayashi, and S. Yamamoto, Ultrasonics **61**, 79 (2015).
21) A. I. Gunawan, N. Hozumi, K. Takahashi, S. Yoshida, Y. Saijo, K. Kobayashi, and S. Yamamoto, Ultrasonics **63**, 102 (2015).

22) N. Hozumi, K. Takanashi, M. Washiya, S. Yoshida, K. Kobayashi, and Y. Saijo, J. Acoust. Soc. Am. **140**, 3245 (2016).
23) S. Yoshida, R. H. Rahayu, K. Takanashi, K. Kishikawa, H. Kurita, K. Takashima, N. Hozumi, K. Kobayashi, and S. Yamamoto, J. Acoust. Soc. Am. **140**, 3139 (2016).
24) K. Takahashi, A. I. Gunawan, S. Yoshida, N. Hozumi, and K. Kobayashi, Proc. 4th Int. Symp. Engineering, Energy and Environments, 2015, p. 89.
25) S. Irie, K. Inoue, K. Yoshida, J. Mamou, K. Kobayashi, H. Maruyama, and T. Yamaguchi, J. Acoust. Soc. Am. **139**, 512 (2016).
26) D. Rohrbach, Q. V. Hoang, Q. Wen, S. A. McFadden, R. H. Silverman, and J. Mamou, IEEE Int. Ultrasonics Symp., 2015, p. 1.
27) Y. Saijo, E. Santos Filho, H. Sasaki, T. Yambe, M. Tanaka, N. Hozumi, K. Kobayashi, and N. Okada, IEEE Trans. Ultrason. Ferroelectr. Freq. Control **54**, 1571 (2007).
28) H. Kumagai, K. Yokoyama, K. Katsuyama, S. Hara, H. Yamamoto, T. Yamagata, N. Taniguchi, N. Hirota, and K. Itoh, Ultrasound Med. Biol. **40**, 2499 (2014).
29) S. Rajagopal, N. Sadhoo, and B. Zeqiri, Ultrasound Med. Biol. **41**, 317 (2015).
30) K. Miura, Y. Egawa, T. Moriki, H. Mineta, H. Harada, S. Baba, and S. Yamamoto, Pathol. Int. **65**, 355 (2015).
31) B. Grobben, P. De Deyn, and H. Slegers, Cell Tissue Res. **310**, 257 (2002).
32) M. Uematsu, Y. Hirai, F. Karube, S. Ebihara, M. Kato, K. Abe, K. Obata, S. Yoshida, M. Hirabayashi, Y. Yanagawa, and Y. Kawaguchi, Cereb. Cortex **18**, 315 (2008).
33) E. I. Fomchenko and E. C. Holland, Clin. Cancer Res. **12**, 5288 (2006).
34) X. L. Zeng, M. D. Jiao, X. G. Wang, and S. Hao, Acta Bot. Sin. **39**, 691 (1997).
35) J. A. Cooper, J. Cell Biol. **105**, 1473 (1987).
36) C. Stournaras, E. Stiakaki, S. B. Koukouritaki, P. A. Theodoropoulos, M. Kalmanti, Y. Fostinis, and A. Gravanis, Biochem. Pharmacol. **52**, 1339 (1996).
37) T. D. Pollard and J. A. Cooper, Science **326**, 1208 (2009).
38) K. M. K. Rao and H. J. Cohen, Mutat. Res./DNAging **256**, 139 (1991).
39) B. Buendia, M. H. Bré, G. Griffiths, and E. Karsenti, J. Cell Biol. **110**, 1123 (1990).
40) Y. Hirose, M. Katayama, O. K. Mirzoeva, M. S. Berger, and R. O. Pieper, Cancer Res. **65**, 4861 (2005).
41) M. C. Chamberlain, Expert Rev. Neurother. **10**, 1537 (2010).
42) T. Kanzawa, I. M. Germano, T. Komata, H. Ito, Y. Kondo, and S. Kondo, Cell Death Differ. **11**, 448 (2004).
43) B. Bergman, U. Friberg, S. Lohmander, and T. Öberg, Eur. J. Oral Sci. **80**, 486 (1972).
44) A. H. Shankar and A. S. Prasad, Am. J. Clin. Nutr. **68**, 447S (1998).

NeuroToxicology 65 (2018) 1–8

Contents lists available at ScienceDirect

NeuroToxicology

Full Length Article

Prenatal exposure to valproic acid alters the development of excitability in the postnatal rat hippocampus

Yukiko Fueta[a], Yuko Sekino[b,c], Sachiko Yoshida[d], Yasunari Kanda[b], Susumu Ueno[e,*]

[a] Department of Environmental Management and Control, School of Health Sciences, University of Occupational and Environmental Health, 1-1 Iseigaoka, Yahatanishi-ku, Kitakyushu, Fukuoka 807-8555, Japan
[b] Division of Pharmacology, National Institute of Health Sciences, 3-25-26 Tonomachi, Kawasaki-ku, Kawasaki, Kanagawa 210-9501, Japan
[c] Laboratory of Chemical Pharmacology, Graduate School of Pharmaceutical Sciences, The University of Tokyo, 7-3-1 Hongo, Bunkyo-ku, Tokyo 113-0033, Japan
[d] Department of Environment and Life Sciences, Toyohashi University of Technology, 1-1 Hibarigaoka, Tempaku-cho, Toyohashi, Aichi 441-8580, Japan
[e] Department of Occupational Toxicology, Institute of Industrial Ecological Sciences, University of Occupational and Environmental Health, 1-1 Iseigaoka, Yahatanishi-ku, Kitakyushu, Fukuoka 807-8555, Japan

ARTICLE INFO

Article history:
Received 5 December 2016
Received in revised form 3 December 2017
Accepted 4 January 2018
Available online 5 January 2018

Keywords:
Developmental neurotoxicity
Valproic acid
Prenatal exposure
Hippocampus
Slice preparation
Electrophysiology

ABSTRACT

Prenatal valproic acid (VPA) exposure is a well-known animal model of autism spectrum disorder (ASD) that produces alterations in embryonic and adult neurogenesis as well as adolescent/adulthood neurobehavioral phenotypes. However, the effects of prenatal VPA exposure on neural network excitability, especially during the synaptogenic period around eye opening, are not fully understood. In this study, we orally administered VPA (300 mg/kg) to pregnant Wistar rats on gestation day 15 and subsequently performed field potential recording in the CA1 area of hippocampal slices obtained from control (saline-exposed) and VPA-exposed rat pups between postnatal day (PND) 13 and PND18. In control slices, we observed an abrupt enhancement of stimulation-dependent responses including population spike (PS) amplitudes and field excitatory postsynaptic potential (fEPSP) slopes at PND16, which coincided with the average day of eye opening. In contrast, VPA-exposed pups exhibited delayed eye opening (PND17) and gradual rather than abrupt increases in PS amplitudes and fEPSP slopes over the duration of the synaptogenic period. We next investigated the involvement of ambient GABA (γ-aminobutyric acid) in PS generation using bicuculline methiodide (BMI), a GABA type A ($GABA_A$) receptor antagonist. In control slices, BMI enhanced PS amplitudes during PND14–15 (before eye opening) and had little effect thereafter during PND16–17; a subsequent regression model analysis of BMI ratios (the ratio of PS amplitudes in the presence and absence of BMI) indicated a possible developmental change between these periods. In contrast, almost identical regression models were obtained for BMI ratios during PND14–15 and PND16–17 in the VPA-exposed group, indicating the absence of a developmental change. Our results suggest that prenatal VPA exposure accelerates the development of hippocampal excitability before eye opening. Moreover, our experimental model can be used as a novel approach for the evaluation of developmental neurotoxicity.

1. Introduction

The impact of exogenous chemical substances on childhood neural development, also known as developmental neurotoxicity, is an important social issue (Andersen et al., 2000; Grandjean and Landrigan, 2006). Valproic acid (VPA) is an antiepileptic drug and mood stabilizer that has been reported to increase the risk of autism spectrum disorders (ASD) in children when women take VPA during early pregnancy (Chomiak et al., 2013). Similarly, rodent models of ASD have been established using prenatal exposure to VPA; in VPA exposure-based models, offspring exhibit autism-like behaviors including impaired social interactions and repetitive behaviors (Markram et al., 2008; Rodier et al., 1997; Roullet et al., 2013; Schneider and Przewlocki, 2005). In addition to neurobehavioral phenotypes, ASD model animals exhibit alterations in embryonic and adult neurogenesis (Juliandi et al., 2015). It has been reported that prenatal exposure to VPA suppresses early neurogenesis in fetal rat brain due to a prolongation of neural

* Corresponding author.
E-mail addresses: yukiko@med.uoeh-u.ac.jp (Y. Fueta), yukos@tkg.att.ne.jp (Y. Sekino), syoshida@ens.tut.ac.jp (S. Yoshida), kanda@nihs.go.jp (Y. Kanda), susumu@med.uoeh-u.ac.jp (S. Ueno).

https://doi.org/10.1016/j.neuro.2018.01.001
0161-813X/

progenitor cell proliferation (Go et al., 2012), and that early postnatal one-week (7–14 postnatal days) exposure to VPA also perturbs neuroblast production and postnatal neurogenesis (Foti et al., 2013). However, it is not well known whether prenatal exposure to VPA also affects neural network formation especially during the synaptogenic period.

Neural activity is a critical regulator of neural network development. It was recently demonstrated that spine density is remarkably increased in the hippocampal CA1 area of mice between postnatal day (PND) 11 and PND21, i.e. during the synaptogenic period (Johnson-Venkatesh et al., 2015). Interestingly, when intrinsic neural activity was suppressed by overexpression of Kir2.1, an inwardly rectifying K^+ channel, increases in spine density during the synaptogenic period were abolished. Thus, neural network activity in the hippocampal CA1 area is necessary for healthy neural development during the synaptogenic period including around eye opening.

Chloride conductance due to ambient concentrations of GABA (γ-aminobutyric acid) also plays a role in regulating neural network excitability during postnatal neural development (Cellot and Cherubini, 2013; Kilb et al., 2013). Ambient GABA originates from the spillover of neurotransmitter escaping the synaptic cleft and from astrocytes via a non-vesicular Ca^{2+}-independent process and mediates tonic inhibition via extrasynaptic GABA type A ($GABA_A$) receptors. However, there is little evidence demonstrating effects of prenatal exposure to toxicants including VPA on ambient GABA-mediated inhibition of neural network excitability.

In the present study, we used a model of prenatal VPA exposure and evaluated effects on neural network activity in the hippocampal CA1 area during the synaptogenic period using hippocampal slices from PND13–18 rat pups. We not only observed the ability of prenatal VPA exposure to abolish development-associated enhancements in stimulation-dependent neural responses, but also confirmed the ability of prenatal exposure to influence ambient GABA-mediated inhibition even prior to eye opening.

2. Material and methods

2.1. Animals

Adult Wistar/ST rats were purchased from Japan SLC *Inc.* (Japan). Rats were housed in plastic cages on paper chip bedding (ALPHA-dri, Shepherd Specialty Papers, USA) and maintained on a 12 h light/dark cycle (light period: 07:00–19:00) in a room with controlled temperature (23 ± 1 °C) and relative humidity (50 ± 15%). Animals were given free access to food (CE2, CLEA Japan Inc., Japan) and filtered water (TCW-PPS filter, Advantech Co., LTD., Japan) dispensed in glass water supply bottles.

The proestrus stage was verified with an impedance checker (MK-10B, Muromachi Kikai Co., Ltd., Japan). When the observed impedance was >3 kΩ female rats were provided with a male rat for mating. The presence of a vaginal plug or sperm in the vaginal smear the following morning confirmed coition, and it was regarded as gestation day (GD) "zero" (Fig. 1). Pregnant rats were randomly divided into two groups: a control group and a VPA exposure group.

VPA was purchased from Wako Pure Chemical Industries, Ltd. (Japan), dissolved in physiological saline (Otsuka Pharmaceutical Co., Ltd, Japan), and orally administered to dams (300 mg/kg) on GD15 under 5% isoflurane gas anesthesia (Pfizer Japan Inc., Japan).

All dams gave birth on GD21, and the date of birth was defined as PND0. If there were more than 10 pups in a litter, the litter size was adjusted to 10 pups on PND1. Litters of less than 10 pups were not adjusted. All pups were housed with their dams during the lactation period. Rat pup body weights were measured on PND1, PND7, PND14, and PND21. The day of eye opening was determined by checking the eyes of pups at 14:00 on each day from PND15–18.

For the electrophysiological study, the control group included pups from 16 control dams and the VPA-exposed group included pups from 17 VPA-exposed dams. All studies were approved by the Ethics Committee on Animal Care and Experimentation and performed in accordance with the guidelines of the University of Occupational and Environmental Health, Japan.

2.2. Slice preparation and recordings

Hippocampal slices (600 μm thickness) were prepared from male pups on each postnatal day between PND13–18 as previously described (Fueta et al., 2004; Fueta et al., 2002). Slices were perfused with artificial cerebrospinal fluid (ACSF) containing 124 mM NaCl, 2 mM KCl, 2 mM $MgSO_4$, 2 mM $CaCl_2$, 1.25 mM KH_2PO_4, 26 mM $NaHCO_3$, and 10 mM glucose; saturated with an O_2 95%/CO_2 5% gas mixture; and stored in a thermostatic bath (27.6 °C). The perfusion rate of ACSF was 1 ml/min for all experiments.

Population spikes (PSs) and field excitatory synaptic potentials (fEPSPs) were simultaneously recorded from the CA1 area of hippocampal slices using glass microelectrodes (Fig. 2A). For slices obtained during the period from PND13–15, PSs were recorded from the area between the pyramidal cell layer and the alveus. The recording positions for PSs and fEPSPs were similar between the control and VPA-exposed groups. Bipolar stimulation electrodes

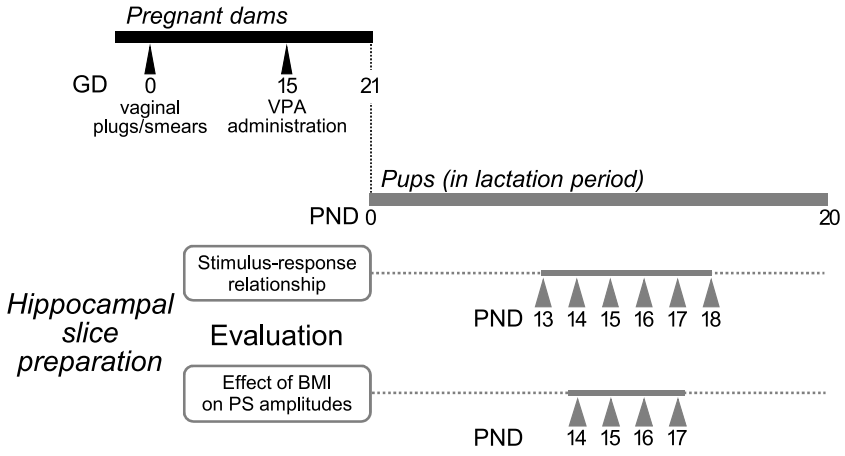

Fig. 1. Scheme of the experimental design.

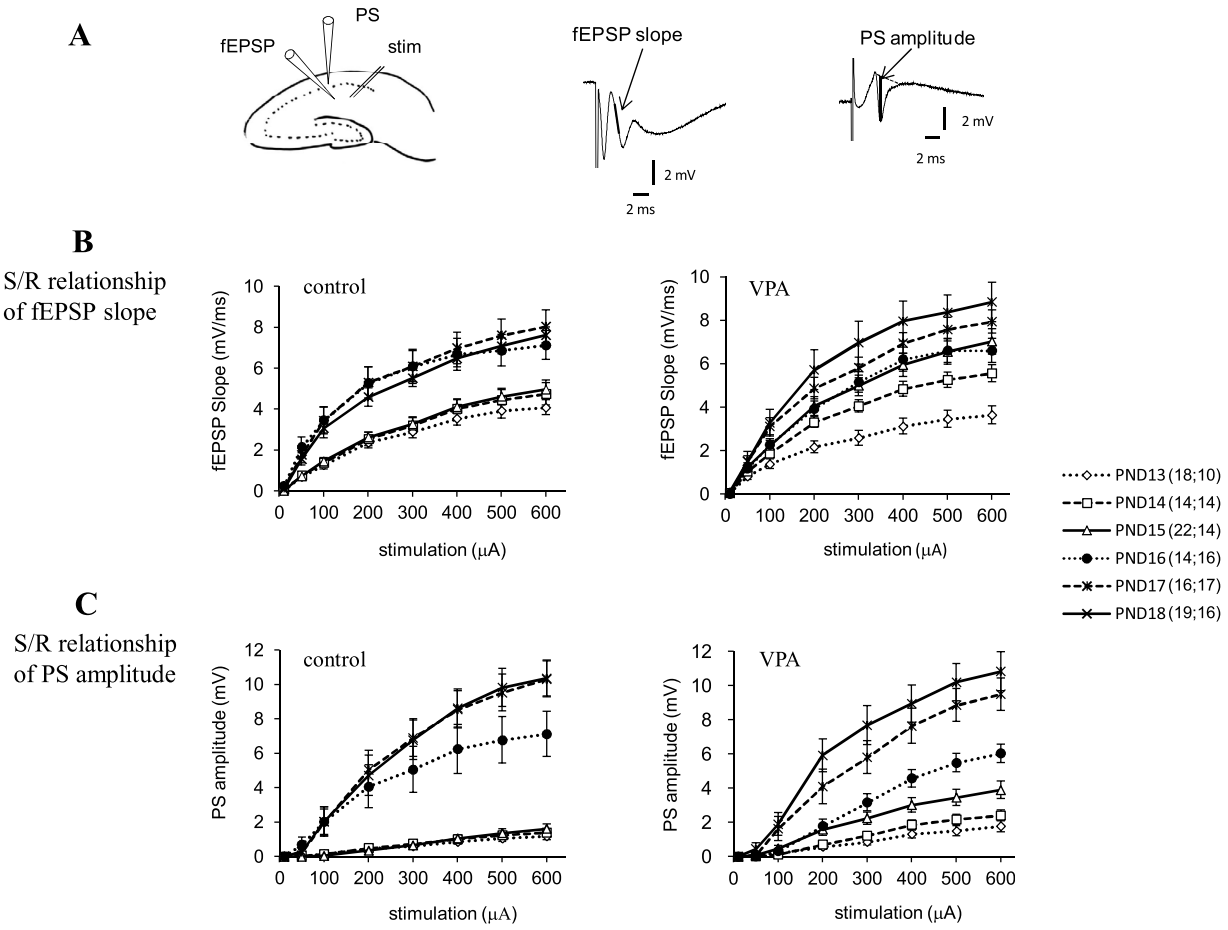

Fig. 2. Stimulation/response (S/R) relationships for population spike (PS) amplitudes and field excitatory postsynaptic potential (fEPSP) slopes recorded from the hippocampal CA1 area of rats that were prenatally exposed to valproic acid (VPA). (A) Illustration depicting the procedure of fEPSP and PS recordings from CA1. Responses were evoked with a stimulating electrode placed in the stratum radiatum. Thick lines on the left traces indicate how measurements of fEPSP slopes and PS amplitudes were taken. (B, C) In control rats (left graphs), the S/R relationships for both fEPSP slopes and PS amplitudes were enhanced between PND15–16. Data were collected from 14 to 22 slices obtained from pups of 4–5 different litters. In VPA-exposed rats (right graphs), these relationships were gradually enhanced between PND13–18. Data were gathered from 10 to 17 slices obtained from pups of 5–6 different litters. The x-axis is stimulation intensity and the y-axis is size of the fEPSP slope or PS amplitude. Data represent the mean ± standard error of the mean. The numbers in parentheses shown with data plot legends are the ones of slices tested for the control and VPA-exposed groups, respectively.

made of stainless wires (50 μm in diameter) were placed on Shaffer collateral/commissural fibers at a distance of about 250 μm from the fEPSP recording electrodes. Stimulation-response relationships were observed with stimulation intensities from 10 to 600 μA. The stimulation interval was 2 min in order to avoid the measurement of overlapping stimulation effects. Between PND14–17, experiments evaluated the effects of bicuculline methiodide (BMI, Tocris Bioscience, U.K.), a $GABA_A$ receptor antagonist, on the generation of PSs. Average PS amplitudes in response to 600 μA stimulation were recorded in triplicate (with 2 min intervals) in the absence and presence of BMI; after PS measurements in the absence of BMI, slices were perfused with ACSF containing BMI (1 μM) for 10 min and subsequently tested. Pups were obtained from at least two different dams, and a total of 3–4 slices per rat pup were tested. Accordingly, we examined 14–22 slices obtained from pups of 4–5 different litters for the control group, and 10–17 slices obtained from pups of 5–6 different litters for the VPA-exposed groups.

2.3. Distribution analysis

Histogram distribution and nonlinear regression analyses of BMI ratios (PS amplitude in the presence of BMI divided by that in the absence of BMI) were conducted using GraphPad Prism software (GraphPad Software, Inc., USA).

2.4. Statistical analysis

Litter sizes and sex ratios as well as pup body weights and the day of eye opening are expressed as the mean ± standard deviation (SD). Electrophysiological results are expressed as the mean ± standard error of mean (SEM), where n refers to the number of hippocampal slices tested. Statistical differences between the control and VPA-exposed groups were determined using two-sided Student's *t*-tests or Mann-Whitney *U* tests at a significance level of $P < 0.05$.

3. Results

For the purpose of our study, the time of eye opening in our rat models was needed to confirm. In consequence, the average day of eye opening was significantly delayed in the VPA-exposed group compared to the control group ($P < 0.01$, Table 1). We also examined general toxicity induced by one-time prenatal VPA exposure at GD15, and found that there were no significant differences between the control and VPA-exposed groups in terms of litter size, litter sex ratio, or changes in pup body weight. Moreover, the number of pups that died before experimentation or weaning was not significantly different between groups (control group, 2 of 206 pups; VPA-exposed group, 4 of 195 pups).

Table 1
Litter sizes and sex ratios as well as pup weight gain and the day of eye opening for the control and VPA-exposed groups.

	Control		VPA-exposed	
Litter size of dams	12.0 ± 2.0	(21)	13.0 ± 3.0	(20)
Sex ratio of pups (percent of males)	48.5 ± 0.1	(21)	49.5 ± 0.1	(20)
Male pup weight (g)				
PND1	6.0 ± 0.6	(55)	5.7 ± 0.4	(53)
PND7	14.9 ± 1.6	(54)	14.1 ± 1.3	(47)
PND14	30.1 ± 1.9	(47)	28.6 ± 2.2	(45)
PND21	50.2 ± 4.3	(20)	46.9 ± 3.7	(23)
Day of eye opening	16.5 ± 0.6	(67)	17.3 ± 0.7**	(77)

Data represent the mean ± standard deviation. Numbers in parentheses are total numbers of dams/pups examined.
** $P < 0.01$, compared to the control. Abbreviations: PND, postnatal day; VPA, valproic acid.

Next, to investigate neural network excitability during the synaptogenic period, we studied stimulation-response (S/R) relationships for fEPSP slopes and PS amplitudes using hippocampal slice preparations, in which the cytoarchitecture and synaptic circuits of the hippocampus are largely retained. S/R relationships exhibited two different stages; similar degrees of stimulation-dependent responses were observed in control pups between PND13–15. However, responses (fEPSP slopes and PS amplitudes) were suddenly augmented on PND16, which seemed to correspond with eye opening. Responses were maintained at an enhanced level for fEPSP slopes and slightly enhanced for PS amplitudes between PND17–18 (Fig. 2B, C).

In contrast, a gradual enhancement of S/R relationships was observed between PND13–18 in the VPA-exposed group, and did appear to correspond with eye opening. Therefore, we reanalyzed fEPSP slopes and PS amplitudes in response to a stimulation intensity of 600 μA, which evoked the maximal responses. PS amplitudes obtained from the control group showed an abrupt increase between PND15–16, whereas those from the VPA-exposed group again demonstrated a gradual increase over the period examined, with significant differences at PND14 and PND15 compared to the control group. A similar but smaller developmental change was observed in the fEPSP slope, with a significant difference between the control and VPA-exposed groups on PND15 (Fig. 3).

Next we investigated the effect of BMI on PS generation in order to elucidate the role of ambient GABA in postnatal PS generation. Fig. 4 shows the effect of BMI on PS amplitudes in the control group before eye opening (PND14–15) and after eye opening (PND16–17). PS amplitudes were enhanced in the presence of BMI during PND14–15 (Fig. 4A, left), but this enhancement was attenuated during PND16–17 (Fig. 4B, left). The mean BMI ratios (ratio of the PS amplitude in the presence of BMI to that in the absence of BMI) were 1.80 ± 0.17 (n = 13) for PND14–15 and 1.14 ± 0.04 (n = 10) for PND16–17. Histograms of BMI ratios (Fig. 4A and B, right) and nonlinear regression analyses revealed a clear developmental change in the probability distribution of BMI ratios for PS amplitudes (Fig. 6, left).

In contrast, for the VPA-exposed group, PS amplitudes generated in the presence of BMI showed small or little increases during both the PND14–15 and PND16–17 periods (Fig. 5A and B, left). The mean BMI ratios were 1.34 ± 0.14 (n = 17) for PND14–15 and 1.14 ± 0.05 (n = 17) for PND16–17. Moreover, histograms of BMI ratios and nonlinear regression analyses (Fig. 5A and B, right) were almost identical between the PND14–15 and PND16–17 periods, suggesting attenuation of the developmental change observed in the control group (Fig. 6, right). We also investigated the responses to BMI for fEPSP slopes, but minimal (non-significant) BMI responses and alterations in developmental change were observed.

4. Discussion

In this study, we investigated the effect of prenatal VPA exposure on the development of neural network activity in the hippocampal CA1 area during the synaptogenic period, including during the period of eye opening. A single dose of VPA (300 mg/kg) was orally administered to dams on GD15 and was not noted to affect dam maternal behavior or fetal/neonatal mortality. In animal models of ASD, VPA is often administered repeatedly or earlier than GD11.5 prior to closure of the neural tube (Rodier et al., 1997). Therefore, the most effective period for observing the effects of prenatal VPA exposure as it relates to ASD may be earlier than GD15.

Brain slice preparation is a well-known laboratory technique for electrophysiology and pharmacology research. Since local neuronal circuits remain intact in brain slices, this neurophysiological preparation is useful for studying neurotoxicity (Fountain et al., 1992) as well as the specific effects of neurotoxic agents on synaptic transmission and plasticity (Varela et al., 2012; Wiegand and Altmann, 1994). The electrophysiological strategy used in the present work has been previously implemented to study the effects of prenatal/perinatal ethanol exposure (Puglia and Valenzuela, 2010), lead (Carpenter et al., 2002; Sui et al., 2000), polychlorinated biphenyl exposure (Altmann et al., 1998; Carpenter et al., 2002; Kim and Pessah, 2011), and toluene exposure (Chen et al., 2011). Thus, we deemed the present model to be useful for

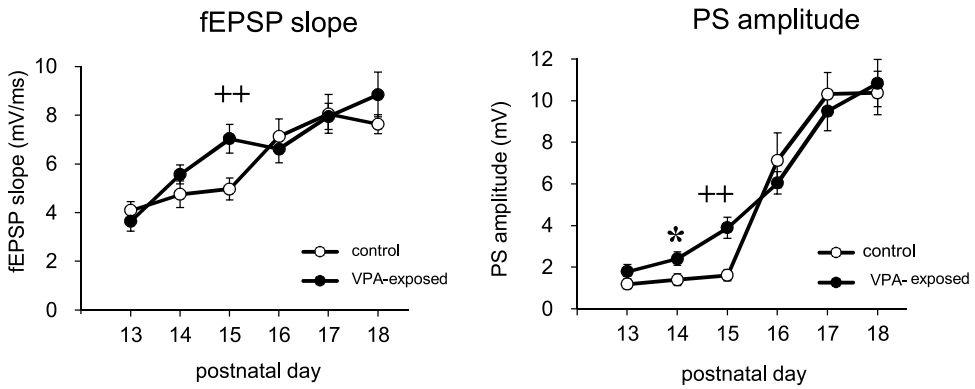

Fig. 3. Developmental changes in field excitatory postsynaptic potentials (fEPSPs) slopes and population spike (PS) amplitudes in the control and valproic acid (VPA)-exposed groups. One-time prenatal exposure to VPA (300 mg/kg) led to postnatal increases in fEPSP slope and PS amplitude at PND15 and during PND14–15, respectively. There were no between-group differences in excitability between PND16–18. The stimulation intensity was 600 μA. * indicates $P < 0.05$ using a Student's *t*-test. ++ indicates $P < 0.01$ using a Mann-Whitney *U* test.

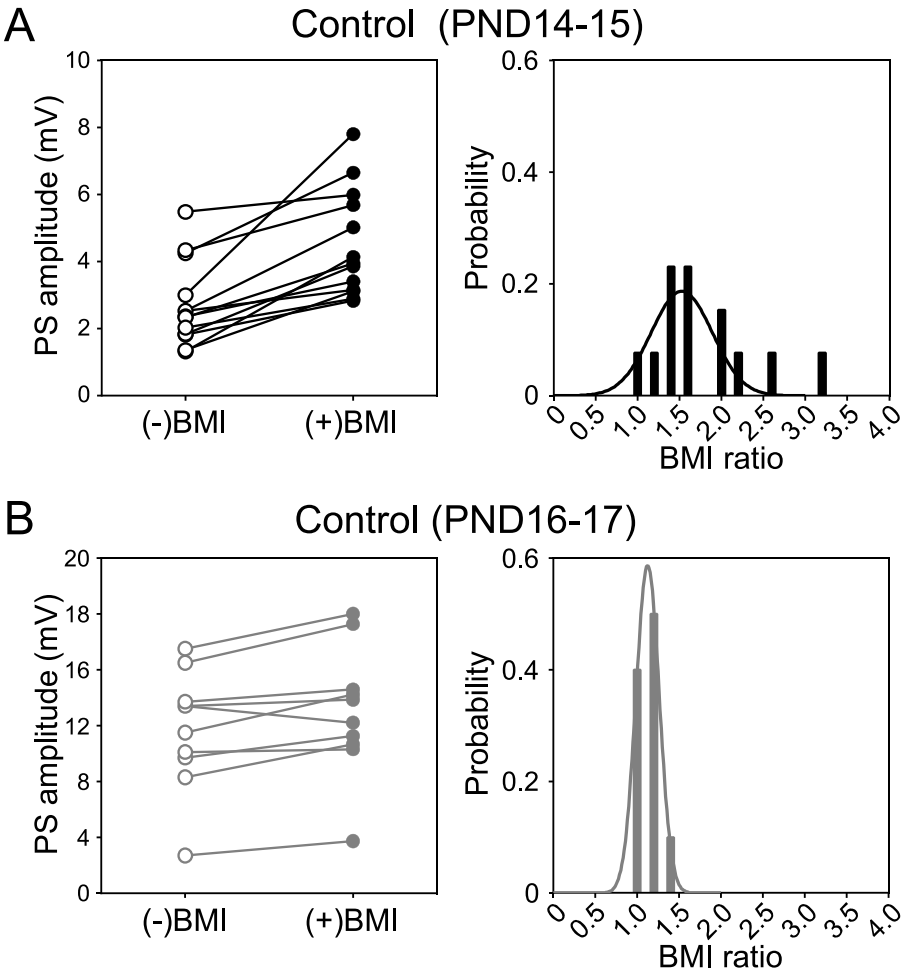

Fig. 4. Development-associated changes in population spike (PS) amplitude responses to BMI in the control group. (A) At PND14–15, application of the $GABA_A$ receptor antagonist BMI to hippocampal slices during recording remarkably increased PS amplitudes; the mean BMI ratio was 1.80 (n = 13, 95% confidence interval = 1.44–2.16). (B) Increased PS amplitudes in response to BMI application were not observed at PND16–17; the mean ratio was 1.14 (n = 13, 95% confidence interval = 1.04–1.24).

evaluating excitatory/inhibitory function and developmental neurotoxicity after VPA exposure.

Our first main finding was that stimulation-dependent responses for fEPSPs and PSs in the hippocampal CA1 area showed two different periods of development in normal pups; one from PND13–15 before eye opening on PND16, and another after eye opening from PND16–18. S/R relationships for neural excitability in the CA1 area exhibited drastic enhancements after eye opening. Alternatively, we did not observe clear discrimination between stimulation-dependent responses before and after eye opening in the VPA-exposed group; enhancements in stimulation-dependent CA1 excitability were observed on PND14 and/or PND15 in the VPA-exposed group compared to the control group, and gradual changes were observed in the subsequent postnatal days. In other words, prenatal VPA exposure appeared to accelerate developmental changes in neural excitability that otherwise appeared in association with eye opening in healthy pups.

Ambient GABA is a critical factor that regulates neural network excitability. Therefore, we also investigated the involvement of ambient GABA in PS generation using BMI, a $GABA_A$ receptor antagonist. On PND14 and PND15 before eye opening, PS amplitudes evoked in the presence of BMI were greater than those in the control condition, suggesting a possible role for PS inhibition by ambient GABA. On PND16 and PND17 on or after eye opening, BMI had little effect on PS amplitudes. These results indicated that ambient GABA was involved in suppressing neural excitability in the CA1 area during neural development prior to eye opening. The centering of this developmental change around the event of eye opening is consistent with a previous report that demonstrated notable increases in spine density on PND15 (Johnson-Venkatesh et al., 2015).

In contrast, BMI had little effect on PS generation before or after eye opening in the VPA-exposed group. Indeed, nonlinear regression models of distribution histograms obtained during PND14–15 and PND16–17 were virtually identical. These results suggest that prenatal exposure to VPA may eliminate ambient GABA suppression of neural excitability prior to eye opening, and are consistent with the observation of enhanced stimulation-dependent responses at PND14 and PND15 in the VPA-exposed group. Accordingly, prenatal exposure to VPA may accelerate neural development in CA1 area during the synaptogenic period.

Ambient GABA-mediated tonic inhibition in hippocampal neurons is synergistically modulated by two GABA transporters (GATs): GAT-1 located on presynaptic membranes and GAT-3 on astrocytes (Egawa and Fukuda, 2013; Kersante et al., 2013). GAT-1 is predominantly responsible for GABA reuptake under resting conditions; alternatively, GAT-3 plays an important role in controlling hippocampal cell excitability during neural activation (Kersante et al., 2013). Therefore, our findings raise the question of whether developmental changes in evoked PS responses to BMI were related to alterations in the expression and/or function of GATs in the CA1 area during development. Further investigations are in progress to address this issue.

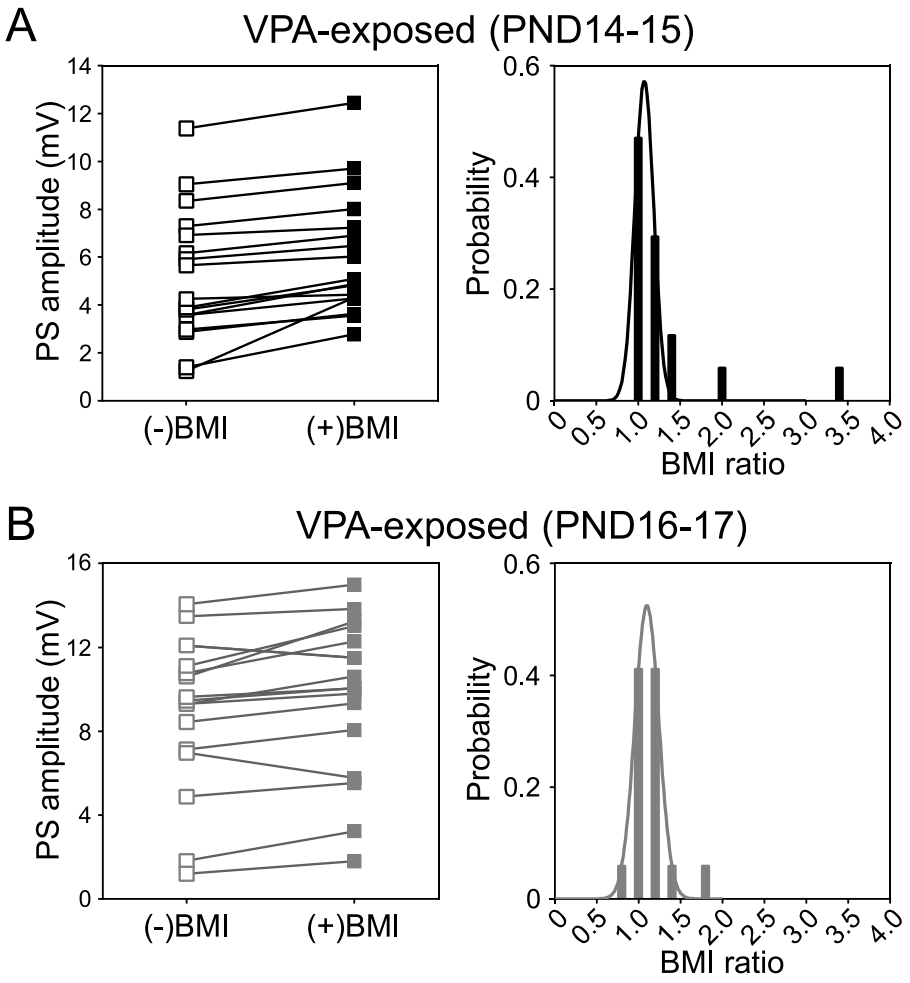

Fig. 5. Development-associated changes in population spike (PS) amplitude responses to BMI in the valproic acid (VPA)-exposed group. Hippocampal slices from the VPA-exposed group were virtually insensitive to BMI during both the PND14–15 (A) and PND16–17 (B) periods; the mean BMI ratios were 1.34 (n = 17, 95% confidence interval = 1.04–1.64) and 1.14 (n = 17, 95% confidence interval = 1.04–1.25), respectively.

Among several hypothetical mechanisms underlying ASD, the disruption of excitation/inhibition (E/I) balance in neuronal circuits has been proposed as a unifying explanation for the complexity and diversity of ASD presentations arising from genetic (Gkogkas et al., 2013; Gogolla et al., 2009; Rubenstein, 2010; Rubenstein and Merzenich, 2003) and environmental factors (Rubenstein and Merzenich, 2003). Although the precise mechanisms of altered E/I balance after prenatal exposure to VPA have not been fully elucidated, this effect has been replicated in several rodent studies. Rinaldi et al. showed that prenatal injection of VPA (500 mg/kg, intraperitoneally) increased N-methyl-D-aspartate (NMDA) receptor subunit protein expression in the whole brains

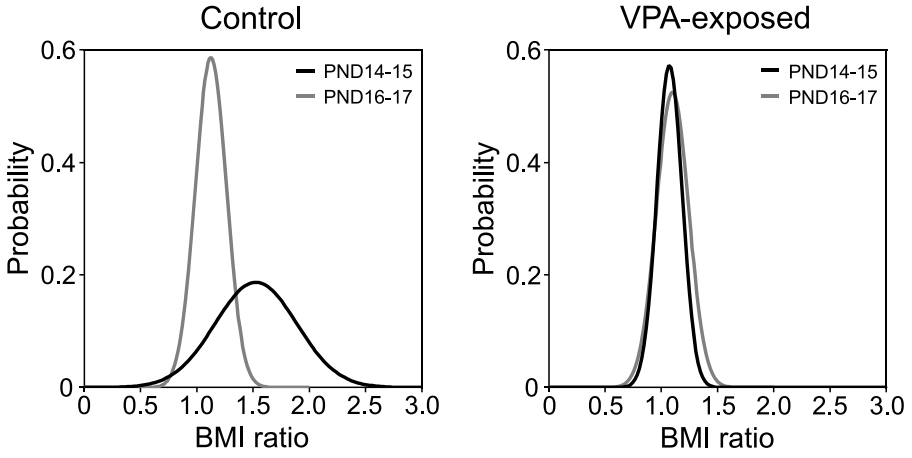

Fig. 6. Developmental alterations in nonlinear regression models of BMI ratios for population spike (PS) responses. Data from right figure panels of 4 and 5 were re-plotted and summarized for the control (left panel) and VPA-exposed groups (right panel).

of pups and enhanced NMDA receptor-mediated synaptic currents in neocortical slices obtained from pups during PND12–16 (Rinaldi et al., 2007). These authors further reported that prenatal VPA exposure induced local circuits hyperconnectivity and enhancements in both excitatory and inhibitory systems in the sensory cortex (Rinaldi et al., 2008). Banerjee et al. reported that a single intraperitoneal injection of VPA (600 mg/kg) at GD11.5 impaired postnatal GABAergic synaptic transmission using slice preparations of the auditory cortex from PND23–45 offspring (Banerjee et al., 2013).

To the best of our knowledge, this is the first report to describe a possible role for GABA-mediated inhibition in the development of evoked PSs during the synaptogenic period around eye opening. Moreover, our data suggest that prenatal exposure to VPA and potentially other developmental neurotoxicants at specific points of the gestation period can accelerate this developmental change. Changes in PS amplitudes evoked from hippocampal slices during prenatal development, especially in the presence of BMI, may be useful as an index for the normal development of neural circuits; to this end, our assay may have utility for testing other candidate drugs/chemicals affecting neural network formation during synaptogenic period. Studies with other known toxicants including organometallic compounds and pesticides are in progress to determine whether similar developmental alterations can be observed using the current experimental approach.

5. Conclusions

In summary, we report that one-time prenatal exposure to VPA at GD15 produced enhancements in stimulation-dependent responses for fEPSP slopes and PS amplitudes in the CA1 area of offspring, and moreover altered offspring PS amplitude responses to BMI. Taken together, prenatal VPA exposure may transiently alter E/I balance, resulting in the acceleration of neural development before eye opening. This effect corresponds with the hypothetical mechanisms underlying ASD; that is, the disruption of E/I balance in developing brain circuits. Although further investigations are required, our results provide an approach for studying effects of chemicals on neural network formation, which is one of important endpoints for the evaluation of developmental neurotoxicity.

Funding

This study was supported by Health and Labor Sciences Research Grants of the Ministry of Health, Labour and Welfare in Japan.

Conflict of interest

The authors declare that there are no conflict of interest.

Acknowledgements

The authors would like to thank Kaoru Sato, Seiichi Ishida, and Daiju Yamazaki for helpful discussion.

References

Altmann, L., Lilienthal, H., Hany, J., Wiegand, H., 1998. Inhibition of long-term potentiation in developing rat visual cortex but not hippocampus by in utero exposure to polychlorinated biphenyls. Brain Res. Dev. Brain Res. 110, 257–260.
Andersen, H.R., Nielsen, J.B., Grandjean, P., 2000. Toxicologic evidence of developmental neurotoxicity of environmental chemicals. Toxicology 144, 121–127.
Banerjee, A., Garcia-Oscos, F., Roychowdhury, S., Galindo, L.C., Hall, S., Kilgard, M.P., Atzori, M., 2013. Impairment of cortical GABAergic synaptic transmission in an environmental rat model of autism. Int. J. Neuropsychopharmacol. 16, 1309–1318.
Carpenter, D.O., Hussain, R.J., Berger, D.F., Lombardo, J.P., Park, H.Y., 2002. Electrophysiologic and behavioral effects of perinatal and acute exposure of rats to lead and polychlorinated biphenyls. Environ. Health Perspect. 110 (Suppl. 3), 377–386.
Cellot, G., Cherubini, E., 2013. Functional role of ambient GABA in refining neuronal circuits early in postnatal development. Front. Neural Circuits 7, 136.
Chen, H.H., Lin, Y.R., Chan, M.H., 2011. Toluene exposure during brain growth spurt and adolescence produces differential effects on N-methyl-D-aspartate receptor-mediated currents in rat hippocampus. Toxicol. Lett. 205, 336–340.
Chomiak, T., Turner, N., Hu, B., 2013. What we have learned about autism spectrum disorder from valproic acid. Pathol. Res. Int. 2013, 712758.
Egawa, K., Fukuda, A., 2013. Pathophysiological power of improper tonic $GABA_A$ conductances in mature and immature models. Front. Neural Circuits 7, 170.
Foti, S.B., Chou, A., Moll, A.D., Roskams, A.J., 2013. HDAC inhibitors dysregulate neural stem cell activity in the postnatal mouse brain. Int. J. Dev. Neurosci. 31, 434–447.
Fountain, S.B., Ting, Y.L., Teyler, T.J., 1992. The in vitro hippocampal slice preparation as a screen for neurotoxicity. Toxicol. In Vitro 6, 77–87.
Fueta, Y., Ishidao, T., Arashidani, K., Endo, Y., Hori, H., 2002. Hyperexcitability of the hippocampal CA1 and the dentate gyrus in rats subchronically exposed to a substitute for chlorofluorocarbons, 1-bromopropane vapor. J. Occup. Health 44, 156–165.
Fueta, Y., Fukuda, T., Ishidao, T., Hori, H., 2004. Electrophysiology and immunohistochemistry in the hippocampal ca1 and the dentate gyrus of rats chronically exposed to 1-bromopropane, a substitute for specific chlorofluorocarbons. Neuroscience 124, 593–603.
Gkogkas, C.G., Khoutorsky, A., Ran, I., Rampakakis, E., Nevarko, T., Weatherill, D.B., Vasuta, C., Yee, S., Truitt, M., Dallaire, P., Major, F., Lasko, P., Ruggero, D., Nader, K., Lacaille, J.C., Sonenberg, N., 2013. Autism-related deficits via dysregulated eIF4E-dependent translational control. Nature 493, 371–377.
Go, H.S., Kim, K.C., Choi, C.S., Jeon, S.J., Kwon, K.J., Han, S.H., Lee, J., Cheong, J.H., Ryu, J. H., Kim, C.H., Ko, K.H., Shin, C.Y., 2012. Prenatal exposure to valproic acid increases the neural progenitor cell pool and induces macrocephaly in rat brain via a mechanism involving the GSK-3β/β-catenin pathway. Neuropharmacology 63, 1028–1041.
Gogolla, N., Leblanc, J.J., Quast, K.B., Sudhof, T.C., Fagiolini, M., Hensch, T.K., 2009. Common circuit defect of excitatory-inhibitory balance in mouse models of autism. J. Neurodev. Disord. 1, 172–181.
Grandjean, P., Landrigan, P.J., 2006. Developmental neurotoxicity of industrial chemicals. Lancet 368, 2167–2178.
Johnson-Venkatesh, E.M., Khan, M.N., Murphy, G.G., Sutton, M.A., Umemori, H., 2015. Excitability governs neural development in a hippocampal region-specific manner. Development 142, 3879–3891.
Juliandi, B., Tanemura, K., Igarashi, K., Tominaga, T., Furukawa, Y., Otsuka, M., Moriyama, N., Ikegami, D., Abematsu, M., Sanosaka, T., Tsujimura, K., Narita, M., Kanno, J., Nakashima, K., 2015. Reduced adult hippocampal neurogenesis and cognitive impairments following prenatal treatment of the antiepileptic drug valproic acid. Stem Cell Rep. 5, 996–1009.
Kersante, F., Rowley, S.C., Pavlov, I., Gutierrez-Mecinas, M., Semyanov, A., Reul, J.M., Walker, M.C., Linthorst, A.C., 2013. A functional role for both γ-aminobutyric acid (GABA) transporter-1 and GABA transporter-3 in the modulation of extracellular GABA and GABAergic tonic conductances in the rat hippocampus. J. Physiol. 591, 2429–2441.
Kilb, W., Kirischuk, S., Luhmann, H.J., 2013. Role of tonic GABAergic currents during pre- and early postnatal rodent development. Front. Neural Circuits 7, 139.
Kim, K.H., Pessah, I.N., 2011. Perinatal exposure to environmental polychlorinated biphenyls sensitizes hippocampus to excitotoxicity ex vivo. Neurotoxicology 32, 981–985.
Markram, K., Rinaldi, T., La Mendola, D., Sandi, C., Markram, H., 2008. Abnormal fear conditioning and amygdala processing in an animal model of autism. Neuropsychopharmacology 33, 901–912.
Puglia, M.P., Valenzuela, C.F., 2010. Repeated third trimester-equivalent ethanol exposure inhibits long-term potentiation in the hippocampal CA1 region of neonatal rats. Alcohol 44, 283–290.
Rinaldi, T., Kulangara, K., Antoniello, K., Markram, H., 2007. Elevated NMDA receptor levels and enhanced postsynaptic long-term potentiation induced by prenatal exposure to valproic acid. Proc. Natl. Acad. Sci. U. S. A. 104, 13501–13506.
Rinaldi, T., Perrodin, C., Markram, H., 2008. Hyper-connectivity and hyper-plasticity in the medial prefrontal cortex in the valproic acid animal model of autism. Front. Neural Circuits 2, 4.
Rodier, P.M., Ingram, J.L., Tisdale, B., Croog, V.J., 1997. Linking etiologies in humans and animal models: studies of autism. Reprod. Toxicol. 11, 417–422.
Roullet, F.I., Lai, J.K., Foster, J.A., 2013. In utero exposure to valproic acid and autism–a current review of clinical and animal studies. Neurotoxicol. Teratol. 36, 47–56.
Rubenstein, J.L., Merzenich, M.M., 2003. Model of autism: increased ratio of excitation/inhibition in key neural systems. Genes Brain. Behav. 2, 255–267.
Rubenstein, J.L., 2010. Three hypotheses for developmental defects that may underlie some forms of autism spectrum disorder. Curr. Opin. Neurol. 23, 118–123.
Schneider, T., Przewlocki, R., 2005. Behavioral alterations in rats prenatally exposed to valproic acid: animal model of autism. Neuropsychopharmacology 30, 80–89.
Sui, L., Ge, S.Y., Ruan, D.Y., Chen, J.T., Xu, Y.Z., Wang, M., 2000. Age-related impairment of long-term depression in area CA1 and dentate gyrus of rat

hippocampus following developmental lead exposure in vitro. Neurotoxicol. Teratol. 22, 381–387.
Varela, C., Llano, D.A., Theyel, B.B., 2012. An introduction to in vitro slice approaches for the study of neuronal circuitry. In: Fellin, T., Halassa, M. (Eds.), Neuronal Network Analysis: Concepts and Experimental Approaches. Humana Press, Totowa, pp. 103–125.
Wiegand, H., Altmann, L., 1994. Neurophysiological aspects of hippocampal neurotoxicity. Neurotoxicology 15, 451–458.